The petrogenesis of the Pliocene Araral stratovolcano in the Andean Central Volcanic Zone, northern Chile

A thesis for a master's degree in geology in the Department of Geological Science, University of Cape Town, South Africa

Mapaseka Mashego

Supervised by: Dr Petrus le Roux and Dr Osvaldo González-Maurel

Contents:

Plagiarism declaration:

I, Mapaseka Mashego (student number: MSHRAM013), declare that:

i. I understand the definition of plagiarism and am familiar with the plagiarism policies at the University of Cape Town
ii. this thesis is my own original work
iii. I have cited, referenced, and acknowledged the work of others

Signed by candidate

Signed on 30 April 2024

Acknowledgements:

This project is based on the research supported in part by the National Research Foundation of South Africa (Grant Number: 129318) and was partially funded by Project FONDECYT Iniciación 11200013. I would like to thank the Masters Research Scholarship for providing me with financial assistance during the course of this research. I extend my gratitude to my supervisors, Dr Petrus le Roux and Dr Osvaldo González-Maurel, for their guidance and feedback. I am thankful to Cristian Aguirre Tapia for his assistance in sample collection, as well as to Dr Benigno Godoy for his collaboration in this research and contributions to sample collection. My appreciation also extends to the technical staff in the Department of Geological Science for their assistance with sample preparation and analysis. I would like to thank my colleagues in the department for their help and support. Lastly, I extend my sincere thanks to my family and friends for their support and encouragement. To everyone who has helped me throughout this research, thank you so much, I am truly grateful.

List of tables:

List of figures:

Abstract

The Altiplano-Puna Volcanic Complex (APVC) is a silicic volcanic complex in the Central Andean Volcanic Zone (CVZ). The APVC is underlain by the thickest known crust in a continental arc setting and the largest known magma body – the Altiplano-Puna Magma Body (APMB). Lavas of the APVC and CVZ are compositionally heterogeneous with elevated Sr isotope ratios relative to mantle-derived lavas and the rest of the Andean Volcanic Arc. The lavas are produced by subduction-induced magmatism and magma differentiation processes, such as crustal assimilation as the magma ascends through the thick crust. The APMB is a large regional melt anomaly proposed to be the source of APVC ignimbrites and the lavas of the APVC have a decreased degree of interaction with the APMB towards its margins. Mafic volcanism in the APVC is rare and is concentrated along the western margin of the APMB. These mafic lavas are predominantly Quaternary in age with some Pliocene lavas. Mafic volcanism in the APVC, and more specifically mafic volcanism during the Pliocene, is understudied.

Araral is an extinct Pliocene stratovolcano situated within the western border of the present-day APMB. This study uses petrography, major and trace element abundances, and O-Sr-Nd-Pb isotope data from Araral to evaluate the magmatic processes active during its formation. The results are compared to previous research on other volcanoes along the western APMB boundary to assess temporal changes in the influence of the APMB on the magmatism in the area. The samples of Araral are high-K calc-alkaline andesites and dacites with plagioclase, pyroxene, biotite, hornblende, and olivine phenocrysts. The lavas are characterised by SiO_2 = 59.89 – 67.16 wt%; MgO = 1.57 – 3.46 wt%; Mg# = 42.15 – 52.90; $^{87}Sr/^{86}Sr$ = 0.706877 – 0.708521; $^{143}Nd/^{144}Nd$ = 0.512281 – 0.512368; $^{208}Pb/^{204}Pb$ = 38.8032 – 38.9191; $^{207}Pb/^{204}Pb$ = 15.6541 – 15.6660; $^{206}Pb/^{204}Pb$ = 18.8861 – 19.0002; $\delta^{18}O_{pyroxene}$ = 6.2 – 7.7; and $\delta^{18}O_{plagioclase}$ = 6.6 – 9.2. Additionally, the samples have enrichments in large ion lithophile elements (LILE), low ratios of heavy rare elements (HREE) to light rare earth elements (LREE), and negative europium (Eu) anomalies. The $^{87}Sr/^{86}Sr$ values are high and the $^{143}Nd/^{144}Nd$ values are low relative to the CVZ, and the Pb isotope ratios reflect the local underlying crust.

The petrography, geochemical, and isotopic data are largely consistent with those of Pliocene and Quaternary APVC lavas within the western margin of the APMB. This suggests that the lavas of Araral have a similar petrogenesis and are formed from magmatic processes like

magma mixing and coupled assimilation and fractional crystallisation (AFC) at shallow crustal levels. The proposed magmatic evolution for the lavas of Araral is that a sub-arc parent magma formed from the assimilation of crustal material into mantle-derived magma at deep crustal levels. The sub-arc parent magma then ascended to the shallow crust and assimilated material from the APMB. The magma then underwent closed-system fractional crystallisation. The overlap of data from Araral with Pliocene and Quaternary APVC lavas along the western margin of the APMB suggests that the APMB has been active and spatially fixed since the Pliocene. However, the comparison of $^{87}Sr/^{86}Sr$ and $^{143}Nd/^{144}Nd$ between Araral and Quaternary lavas on the same velocity contour within the present-day APMB shows that Araral has higher $^{87}Sr/^{86}Sr$ and lower baseline $^{143}Nd/^{144}Nd$ values. This suggests that the lavas of Araral had a higher degree of interaction with the APMB. The higher degree of APMB influence is an indication of a greater spatial extent than the present-day contours for the zones of higher partial melts during the Pliocene.

1. Introduction:

Mafic volcanism in the Central Andean Volcanic Zone (CVZ) and Altiplano-Puna Volcanic Complex (APVC) is rare (Godoy et al., 2019; González-Maurel et al., 2019b; Stern, 2004). Mafic volcanism in the APVC and the magmatic processes involved are understudied – especially mafic volcanism during the Pliocene (González-Maurel et al., 2019a; Lister 2019). The study of the lavas of Araral not only provides insight into an understudied volcano (Araral), but also into Pliocene APVC lavas, and mafic volcanism in the APVC in general. Araral is well-preserved and one of the few known Pliocene volcanoes situated along the western margin of the present-day Altiplano-Puna Magma body (APMB) – Quaternary volcanoes are most common. There is little research on Araral and constraining the lavas of Araral can lead to a better understanding of mafic volcanism and magmatism in the APVC as well as the APMB and its influence during the Pliocene and how they have changed since.

The Andean volcanic arc is proposed to be a product of subduction-induced magmatism (Pichowaik et al., 1990; Thorpe, 1984) and has four volcanic zones – including the CVZ (fig. 1.1a). The CVZ is underlain by continental crust that is ~70 km thick (Beck et al., 1996) and consists of extensive ignimbrites, stratovolcanoes, and mafic monogenetic volcanoes (Stern, 2004). The lavas of the CVZ are characterised by andesitic to rhyolitic compositions, geochemical variability, and enrichments in LILE (Davidson et al., 1991; Stern 2004). The CVZ has lower neodymium (Nd) and higher strontium (Sr) and oxygen (O) isotope ratios than the other Andean volcanic zones (Davidson et al., 1991; Harmon et al., 1981). The lead (Pb) isotope ratios are similar to those of the underlying basement (Mamani et al., 2008, 2010). The distinct geochemical characteristics of the CVZ are attributed to magma differentiation processes as the magma ascends through the thick crust (e.g. Davidson et al., 1990). The magma differentiation processes involved are fractional crystallisation, crustal assimilation, a combination of both (AFC processes), and magma mixing (Davidson et al., 1990; Godoy et al., 2014; González-Maurel et al., 2020; Mamani et al., 2010; Wörner et al., 2018).

The APVC is an ignimbrite province in the CVZ (de Silva, 1989) and is underlain by the APMB – a geophysical anomaly suggested to be a zone of partial melt in the upper to middle crust (fig. 1.1b; Ward et al., 2014; Zandt et al., 2003). The degree of partial melt increases from the margins to the centre of the APMB from 4 to 25% (Ward et al. 2014; Araya Vargas et al., 2019). Mafic volcanism in the APVC is associated with stratovolcanoes and monogenetic

centres (e.g. González-Maurel et al., 2019a). Mafic lavas of the APVC are defined as basaltic-andesites and andesites containing pyroxene and, potentially, olivine (González-Maurel et al., 2019a, and references therein). The mafic lavas are spatially associated with extensional fault systems (e.g. Godoy et al., 2014; Trumbull et al., 2006) and are commonly situated along the western margin of the APMB in northern Chile, 21°10′S – 22°50′S (González-Maurel et al., 2019a, and references therein). Mafic volcanism in the APVC has been attributed to superheated hydrous basaltic magma ascending rapidly through extensional crustal structures (de Silva, 1989; Mattioli et al., 2006). Alternatively, mafic volcanism has been proposed to be a result of minimal interaction with the APMB during magma ascent (Godoy et al., 2017; González-Maurel et al., 2019a). These magmas ascend through the zones with lower degrees of partial melt and thus are less contaminated than those at the centre of the APMB (Godoy et al., 2017). Additionally, the geochemistry of lavas in the APVC suggests magma evolution occurs at shallow crustal levels, while the geochemistry of other lavas in the CVZ indicates magma evolution at deep crustal levels (e.g. Godoy et al., 2017). The shallow crustal magma evolution of lavas of the APVC suggests that the APMB may have a role in the magma evolution of mafic APVC lavas (Godoy et al., 2017).

Araral is an extinct Pliocene stratovolcano in the CVZ and is situated along the border between northern Chile and Bolivia (21°35′29” S, 68°14′3” W; fig. 1.1b and c). It was constructed 2.75 million years ago near the western margin of the present-day surface projection of the APMB (González-Maurel et al., 2019a; Sellés and Gardeweg, 2017). The lavas of Araral are pyroxene- and, occasionally, olivine-bearing andesites and dacites (González-Maurel et al., 2019a; Sellés and Gardeweg, 2017).

This research uses petrography, major element, trace element, radiogenic isotope, and O isotope data to constrain the characteristics of the lavas of Araral. This information is used to evaluate the magmatic processes and sources that formed the lavas of Araral and assess the influence of the APMB on the lavas of Araral. Further, this research uses the comparison of the Araral data with data from mafic APVC lavas with known APMB influence to assess how the influence of the APMB on APVC lavas has changed since the Pliocene.

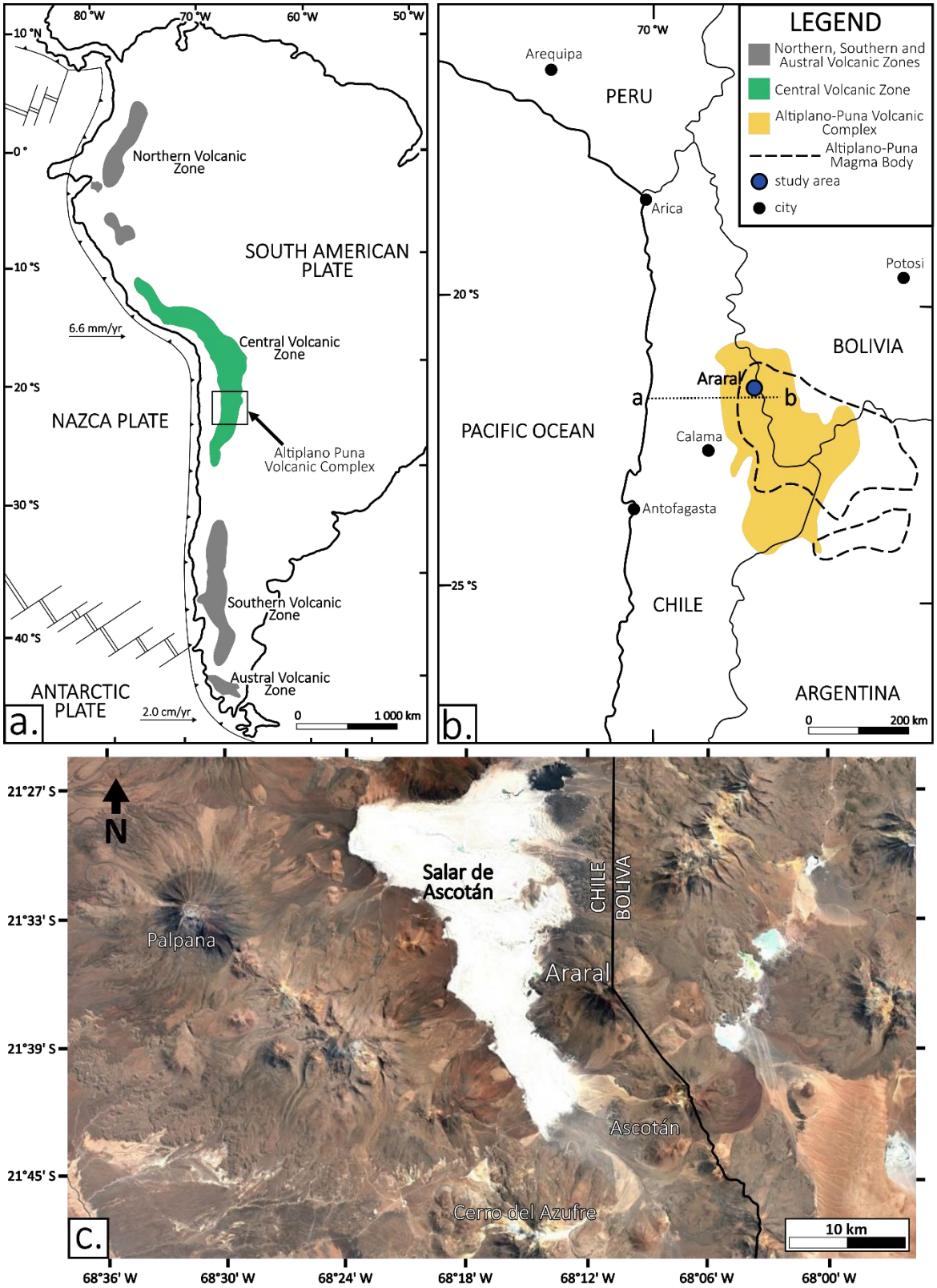

Figure 1.1. (a) Map of the Andean volcanic chain (adapted from de Silva, 1989 and Stern, 2004). (b) Map of the APVC, the surface projection of the present-day APMB, and the study area (adapted from de Silva, 1989; Zandt et al. 2003). (c) A satellite image showing Araral along with the nearby salar and volcanoes (Google Earth, 01 November 2024).

2. Geological background:

2.1. Andean Volcanic Arc:

The Andean Cordillera is morphologically continuous and spans a length of 9 000 km along the western edge of South America (fig. 1.1a). The Andean Cordillera coincides with the convergent plate boundary where the Nazca and the Antarctic Plates are subducting beneath the South American Plate along the western margin.

Andean magmatism and subduction are proposed to be genetically related (Thorpe, 1984). Andean magmatism was initiated in the early Jurassic and is a consequence of the subduction (Pichowaik et al., 1990). Dehydration and melting of the subducting lithosphere trigger flux melting as fluids from the subducting slab are introduced into the overlying mantle wedge (Thorpe, 1984). The initial stages of Andean magma generation are similar to those of ocean island arcs. This is reflected in the geochemical similarities in ocean island basalts and lavas of the Andes that undergo minimal crustal contamination during magma ascent (Hickey-Vargas et al., 1989).

There are four zones of Andean volcanism (fig. 1.1): Northern (NVZ, 5°N – 2°S), Central (CVZ, 14 – 28°S), Southern (SVZ, 33 – 46°S) and Austral Volcanic Zones (AVZ, 49 – 55°S). These zones are separated by the Peruvian flat-slab segment (5 – 15°S, between the NVZ and CVZ), the Pampean flat-slab segment (27 – 33°S, between the CVZ and the SVZ), and the Patagonian Volcanic Gap (46 – 49°S, between the SVZ and AVZ). For detailed descriptions of the Andean volcanic zones and flat-slab segments refer to Stern (2004).

2.2. Central Andean Volcanic Zone:

The CVZ is located in Southern Peru, northern Chile, southwestern Bolivia, and northwestern Argentina. The CVZ is north-south trending and is bound by the Nazca and Juan Fernandez Ridges (Stern, 2004). In the Central Andes, the Nazca plate has a subduction rate of 6.6 cm/yr, at subduction angles of 25°- 30° and an azimuth of 78° (Angermann et al., 1999). The CVZ is well preserved as a result of hyper-arid conditions associated with the Atacama Desert – the driest desert known (Stern, 2004). The Central Andes have an average elevation of 3 700 m, and the region has a width of 200 km and a length of 700 km. The main longitudinal

morphological units, from west to east are (fig. 2.1): (1) the Coastal Cordillera – Jurassic to early Cretaceous igneous rocks and some Cenozoic sedimentary rocks; (2) the Longitudinal Valley – relatively flat basin with Cenozoic sedimentary rocks and ignimbrites; (3) the Chilean Precordillera – Palaeozoic, Mesozoic and Cenozoic rocks; (4) pre-Andean basin – Calama and Salar de Atacama basins, Cenozoic sedimentary rocks (5) the Western Cordillera – predominantly Quaternary volcanic rocks; (6) the Altiplano-Puna region – mainly Neogene ignimbrites and some Cenozoic sedimentary and volcanic rocks; and (7) the Eastern Cordillera (Araya Vargas et al., 2019, and references therein).

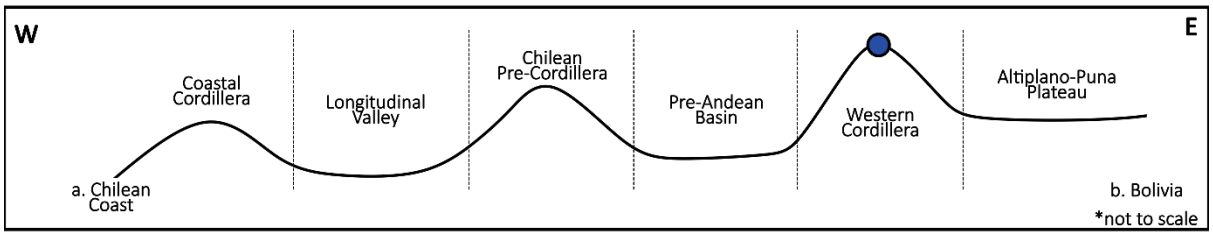

Figure 2.1. Cross-section of points a to b on the map from Figure 1.1b (Araya Vargas et al., 2019, and references therein). The blue dot represents the study area.

The central Andean volcanic front is located in the Western Cordillera, 240 – 300 km east of the trench, and 120 km above the subduction slab (Stern, 2004). The volcanic arc has been migrating eastward since the Jurassic (Pichowaik et al., 1990; Trumbull et al., 2006). The Andean Cycle describes the four main phases of the eastward migration of the volcanic arc: (1) Jurassic to Early Cretaceous arc – volcanic rocks predominantly erupted in the Chilean Coastal Range; (2) Mid-Cretaceous arc – Longitudinal Valley and Sierra de Moreno in Chile; (3) Late Cretaceous to Palaeogene arc – followed flat-slab subduction; (4) Miocene to Holocene active volcanic arc – volcanic rocks predominantly in the Western Cordillera associated with the increase in the subduction angle of the Nazca Plate (Trumbull et al., 2006). The Andean cycle is attributed to (1) subduction angle changes of the Nazca plate since 200 Ma (Scheuber and Reutter, 1992); and (2) subduction erosion (Ranero et al., 2006). The eastward migration of the central Andean volcanic front led to systematic spatiotemporal changes in the composition of the lavas. Since the Jurassic, the isotopic signatures of the lavas have changed and they have become enriched in incompatible trace elements (Davidson et al., 1990).

The crust underlying the CVZ is ~ 70 km thick and is the thickest crust in a continental arc setting (Beck et al., 1996). Most of the crustal thickening in the Central Andes occurred during

the Miocene (Allmendinger et al., 1997) and is suggested to be caused by (1) crustal shortening (Allmendinger et al., 1997; Beck et al., 1996); (2) magmatic underplating (Schmitz et al., 1997); (3) a combination of both crustal shortening and magmatic underplating (Giese et al., 1999); or (4) lithospheric delamination (Kay et al. 1994).

The volcanic rocks of the CVZ are highly compositionally variable and are predominantly andesitic to rhyolitic, with rare occurrences of basaltic andesites and basalts (Stern, 2004). Mafic volcanism in the CVZ is associated with stratovolcanoes and monogenetic centres (Mattioli et al., 2006). Rhyolitic compositions (>68%) dominate ignimbrites and stratovolcanoes are predominantly metaluminous high-K calc-alkaline andesites and dacites with strong subduction signatures (Mamani et al., 2008, 2010; Stern, 2004; Trumbull et al., 2006; Wörner et al., 2018). Trace element patterns of CVZ lavas show LILE enrichment and relative niobium (Nb) and tantalum (Ta) depletion, common characteristics of lavas in subduction settings (Davidson et al., 1991).

The lavas have lower Nd, as well as higher Sr and O isotope ratios with respect to primitive lavas (Davidson et al., 1991; Harmon et al., 1981). Primitive lavas are characterised by $^{143}Nd/^{144}Nd > 0.5129$ and $^{87}Sr/^{86}Sr = 0.703$ and $\delta^{18}O = 5.7 \pm 0.3$ ‰ (Davidson et al., 1991; Eiler, 2001; Harmon et al., 1981; Wörner et al., 2018). Lavas of the CVZ are characterised by $^{87}Sr/^{86}Sr > 0.706$ (Harmon et al., 1981); $^{143}Nd/^{144}Nd < 0.5125$ (Davidson et al., 1991); $\delta^{18}O_{whole\ rock} = 6.7 – 14.0$ ‰; $\delta^{18}O_{olivine} = 5.0 – 8.3$ ‰; $\delta^{18}O_{clinopyroxene} = 5.5 – 8.7$ ‰; $\delta^{18}O_{amphibole} = 5.1 – 6.3$ ‰; $\delta^{18}O_{biotite} = 6.7$ ‰; $\delta^{18}O_{plagioclase} = 6.5 – 9.6$ ‰; and $\delta^{18}O_{quartz} = 7.8 – 14.6$ ‰ (González-Maurel et al., 2020, and references therein; Michelfelder et al., 2013). High $^{87}Sr/^{86}Sr$ are even characteristic of the most primitive volcanic rocks in the CVZ (Davidson et al., 1991; Kay et al., 1994; Godoy et al., 2019; González-Maurel et al., 2019a). The isotopic compositions suggest extensive fractional crystallisation and assimilation of continental crust and/or subcontinental mantle lithosphere during magma ascent through the thick Central Andean crust – AFC processes (Davidson et al., 1991; Mamani et al., 2010; Thorpe, 1984, Wörner et al. 2018).

For these magmas, differentiation is initiated when mafic components stagnate and crystallise at the mantle-crust boundary due to their high density (Wörner et al., 2018). Further differentiation occurs in a lower-crust MASH petrogenic zone – where **m**elting, **a**ssimilation, **s**torage, and **h**omogenisation occur (Hildreth and Moorbath, 1988). Through these processes the magmas acquire high Sr to yttrium (Y) ratios (>40) and high LREE/HREE ratios, indicating

fractionation in a high-pressure environment where garnet is a stable phase (Davidson et al., 1990; Wörner et al., 2018). Differentiation in MASH zones produces silica-rich magmas, which may ascend to mid-crustal levels to form reservoirs (Hildreth and Moorbath, 1988).

Geochemical compositions show that the extent of crustal contamination increases with time in the Central Andes since the Miocene as the crust thickened (Trumbull et al., 1999). The lavas of the CVZ exhibit increases in $^{87}Sr/^{86}Sr$ and decreases in $^{143}Nd/^{144}Nd$ values, along with thorium (Th), uranium (U), and rubidium (Rb) enrichments since the Miocene (Trumbull et al., 1999). Neogene to recent volcanism in the CVZ is characterised by andesitic and dacitic stratovolcanoes as well as extensive silicic volcanism associated with ignimbrites (Allmendinger et al., 1997; Davidson et al., 1991, de Silva et al., 2006).

2.3. Altiplano-Puna Volcanic Complex:

The APVC is a silicic tectono-volcanic province that was produced by an ignimbrite flare-up in the late Miocene. The APVC is located in Argentina, Bolivia, and Chile (21 – 24°S; fig. 1.1b), at the southward transition between the Altiplano and Puna plateaus. The Altiplano and Puna plateaus have average elevations of 3.8 and 4.5 km, respectively. The APVC has an average elevation of 4 km and has volcanoes with elevations of >6 km. It has an unusually high elevation for a plateau at a subduction zone setting – such elevations are more common in continent-continent convergent plate boundaries. It is one of the largest silicic volcanic provinces in the world (de Silva, 1989; Allmendinger et al., 1997) with an approximate area of 70 000 km^2 (de Silva, 1989; de Silva and Gosnold, 2007) and a width of 350 – 400 km.

In the area, there are N-S and NE-SW trending local fault and lineament systems and two of the four main NW-SE trending regional fault and lineament systems, the Lipez-Coranzuli and the Calama-Olacapato-El Toro (Salfity, 1985; Tibaldi et al., 2009). The regional fault systems formed in the Palaeozoic, however, the current tectonic regime was initiated in the Miocene (Salfity, 1985; Tibaldi et al., 2009). The region was initially dominated by thrust faulting, but there was a shift to extensional and strike-slip faulting 1 – 2 Ma (Allmendinger et al., 1997). This change is a result of principle stress changes in the late Miocene which also reactivated the pre-existing structures (Tibaldi et al., 2009; Trumbull et al., 2006; Zandt et al., 2003). There is an apparent spatial association between the fault zones and the volcanic centres and

complexes in the area (e.g. Godoy et al., 2014; Trumbull et al., 2006). It is proposed that these extensional fault systems serve as conduits for magma ascension in the area (e.g. de Silva et al., 2006; Trumbull et al., 2006).

Hydrothermal activity is also spatially associated with the fault and lineament systems (Maza et al., 2021 and references therein). There are occurrences of hydrothermal activity and alteration at some of the volcanoes located near Araral – e.g. Cerro del Azufre and Ascotán (fig. 1.1c; Godoy et al., 2023; Maza et al., 2021 and references therein). Hydrothermally altered APVC lavas are characterised by rocks that are yellow-white in colour and occasionally have hydrothermal chimneys in their vicinity (e.g. Maza et al. 2021). They typically contain phyllosilicates (namely, illite, chlorite, kaolinite, alunite, pyrophyllite, and cristobalite), sulphates (e.g. gypsum), and sometimes native sulphides and Fe-Al-Ti oxide-hydroxides (Maza et al., 2021). Hydrothermally altered lavas have high $^{87}Sr/^{86}Sr$ values, like other APVC lavas, while the $\delta^{18}O$ values are low relative to other APVC lavas (Godoy et al.,2023).

The area has experienced large-scale silicic volcanism since 10 Ma (de Silva, 1989). An estimated 15 000 km^3 of magma erupted between 10 and 1 Ma to form ignimbrites (de Silva, 1989, 2006). These ignimbrite flare-ups are largely attributed to the production of crustal melts as a consequence of crustal thickening below the CVZ (de Silva, 1989). The large amounts of volcanism likely correspond to large amounts of melt production (de Silva et al., 2006). Volcanism in the APVC is episodic, with steady-state phases (associated with ignimbrite flare-ups) and waning stages (associated with stratovolcanoes and lava flow complexes). These ignimbrite flare-ups have four major pulses (10, 8, 6 and 4 Ma), that indicate that during these intervals there was a high influx of mantle-derived melt (de Silva et al., 2006). Each major pulse was accompanied by an increase in the intensity of the flare-ups, the intensity then decreased following the pulse that occurred 4 Ma (Salisbury et al., 2011). Volcanism in the APVC is associated with changes in subduction slab angle and magma production rates (Allmendinger et al., 1997; de Silva and Gosnold, 2007). Ignimbrite flare-ups are a product of the accumulation of dacitic magmas at shallow to mid-crustal levels (de Silva et al., 2006).

The model proposed by de Silva and Gosnold (2007) is that APVC lavas are formed from the differentiation of mafic magma (45 – 52 wt% SiO_2) in a lower crustal MASH zone to produce an intermediate magma (~60 wt% SiO_2) that ascends to a shallower reservoir and is then

differentiated to form a silicic magma (~65 wt% SiO_2). Isotope and trace element data suggest that the formation of ignimbrites is a result of the mixture of crustal melts with a minimum of 30% mafic mantle-derived magma at depths of 15 to 30 km (de Silva, 1989; de Silva et al., 2006; de Silva and Kay, 2018). Magma evolution at shallow crust levels (garnet-free environment) results in APVC lavas having low LREE/HREE and Sr/Y ratios relative to other lavas in the CVZ (Godoy et al., 2014, 2017, and references therein). The interaction with the shallow crustal reservoir results in the lavas of the APVC having higher $^{87}Sr/^{86}Sr$ (0.707 – 0.717) and lower $^{143}Nd/^{144}Nd$ (0.5121 – 0.5124) than the rest of the CVZ (Godoy et al., 2014, 2017, and references therein). The Pb isotope ratios of APVC lavas are consistent with those of the local basement – $^{208}Pb/^{204}Pb > 38.655$, $^{207}Pb/^{204}Pb > 15.651$, and $^{206}Pb/^{204}Pb > 18.551$ (Godoy et al., 2014; Mamani et al., 2008, 2010).

Mafic volcanism within the APVC is rare and typically found in stratovolcanoes and monogenetic centres along the margins of the APMB (Godoy et al., 2019; González-Maurel et al., 2019b). These mafic eruptions are thought to be a result of (i) direct and rapid ascension of hydrous basaltic magma (Mattiol et al., 2006); or (ii) mafic magmas having minimal interaction with APMB to produce moderately contaminated lavas that are relatively mafic (Godoy et al., 2017; González-Maurel et al., 2019a). The lavas near the margins of the APMB are characterised by lower $^{87}Sr/^{86}Sr$ and higher $^{143}Nd/^{144}Nd$ values than those at the centre and ignimbrites (Godoy et al., 2017; González-Maurel et al., 2019a). Along the western margin (21°10′S – 22°50′S) of the APMB there is an abundance of mafic to intermediate lavas that are olivine- and pyroxene-rich (Godoy et al., 2019; González-Maurel et al., 2019a, 2019b; Sellés and Gardeweg, 2017).

2.4. Altiplano-Puna Magma Body:

The APMB is a geophysical anomaly underlying the APVC in the middle to upper crust (fig. 2.2; Araya Vargas et al., 2019; Chmielowski et al., 1999; Ward et al., 2014; Zandt et al., 2003. It is characterised by low electrical resistivity, high heat flow values and low seismic velocity (Araya Vargas et al., 2019; Chmielowski et al., 1999; Ward et al., 2014; Zandt et al., 2003). This geophysical anomaly is thought to be a large-scale magma reservoir (Chmielowski et al., 1999) and the source of the APVC ignimbrites (Zandt et al., 2003). The present-day APMB is

the largest known magma body and has an estimated volume of 500 000 km^3, a diameter of 200 km (Chmielowski et al., 1999; Ward et al., 2014), and a depth range of 4 to 30 km. This magma body is formed from partial melting of the upper crust caused by advective heat from stagnating mantle-derived magmas (Annen and Sparks, 2002). Geophysical evidence suggests that the degree of partial melt is variable (Chmielowski et al., 1999), ranges from 4 to 25% and decreases from the centre to the margins (Ward et al. 2014; Araya Vargas et al., 2019). These zones of partial melt are represented by s-wave velocity contours, that vary from 3.2 to 2.1 $km.s^{-1}$ towards the centre (fig. 2.2).

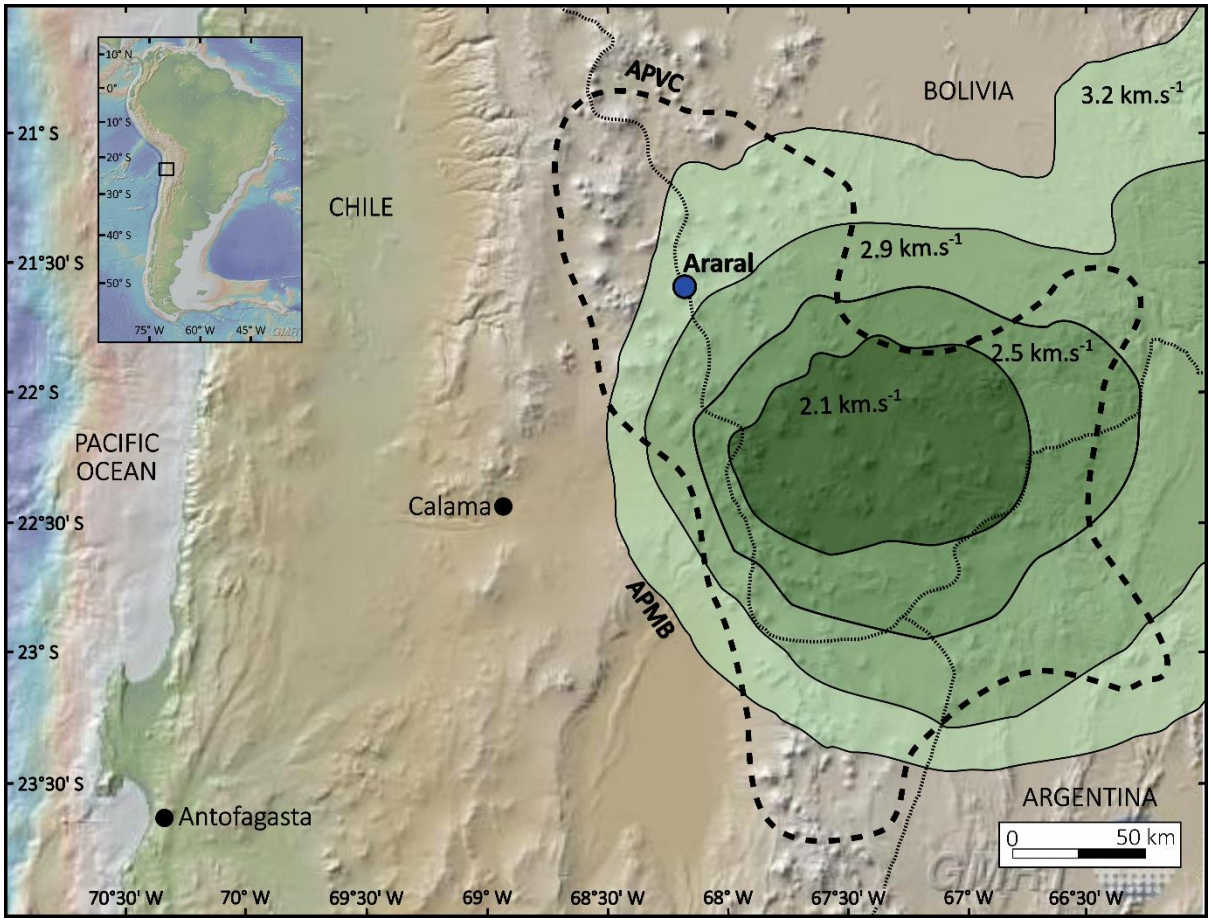

Figure 2.2. Global Multi-Resolution Topography (GMRT) image showing the surface projection of the present-day APMB, the APVC, and Araral. The green areas represent the extent of the APMB based on the joint ambient noise-receiver function inversion S-velocity model from Ward et al. (2014).

2.5. Araral volcano:

Araral is an extinct stratovolcano in the CVZ and is located on the border of Chile and Bolivia (21°35′29” S, 68°14′3” W), along the northwestern margin of the present-day APMB (fig. 2.2). Araral has a peak elevation of 5 698 m, and a diameter of 12 km (Sellés and Gargeweg, 2017). It was formed 2.75 ± 0.04 Ma and is made up of units of Pliocene lavas and Quaternary alluvial, colluvial, and glacial deposits (Sellés and Gargeweg, 2017). The lavas of Araral are high-K calc-alkaline andesites and dacites (González-Maurel et al., 2019b; Sellés and Gargeweg, 2017). The lavas have porphyritic and glomeroporphyritic textures with glassy groundmass and phenocrysts of plagioclase, olivine, pyroxene, amphibole, and biotite (González-Maurel et al., 2019b; Sellés and Gargeweg, 2017).

3. Sampling and methods:

3.1. Sample preparation:

A total of 20 samples were collected from lava flows in November 2021 and early April 2022 (fig. 3.1; fig. 3.2; table 3.1). The samples were intentionally collected from lavas with no visible indication of hydrothermal alteration. The samples were grouped according to the most abundant mafic phenocryst phases, as explained in the results section. There are three groups the olivine-rich (n = 2), pyroxene-rich (n = 14), and biotite-rich (n = 4) groups. The samples were collected from the potential flows for Araral mapped on Google Earth Pro – these flows were mapped using surface colour and texture differences. The samples were prepared in the crushing lab in the Department of Geological Sciences, University of Cape Town (UCT), and were split – including a piece to make thin sections. The remainder of the samples were put in the jaw crusher and then put through a 1400 µm sieve. The material < 1400 µm was put into the mill and turned into powder to obtain whole-rock major and trace element data and Sr-Nd-Pb isotope ratios. The material > 1400 µm was put in the jaw crusher again, then put through 1400 µm and 900 µm sieves, the >1400 µm and >900 µm material were put into separate vials for mineral picking for single mineral O isotope analysis. This study does not include electron microprobe (EMP) mineral chemical analysis due to the EMP facility in the Department of Geological Science, UCT, not being operational while this research was conducted. The elemental data from such analyses could have been used to model the magmatic evolution of the lavas of Araral – as done for Azufre by Lister, 2019.

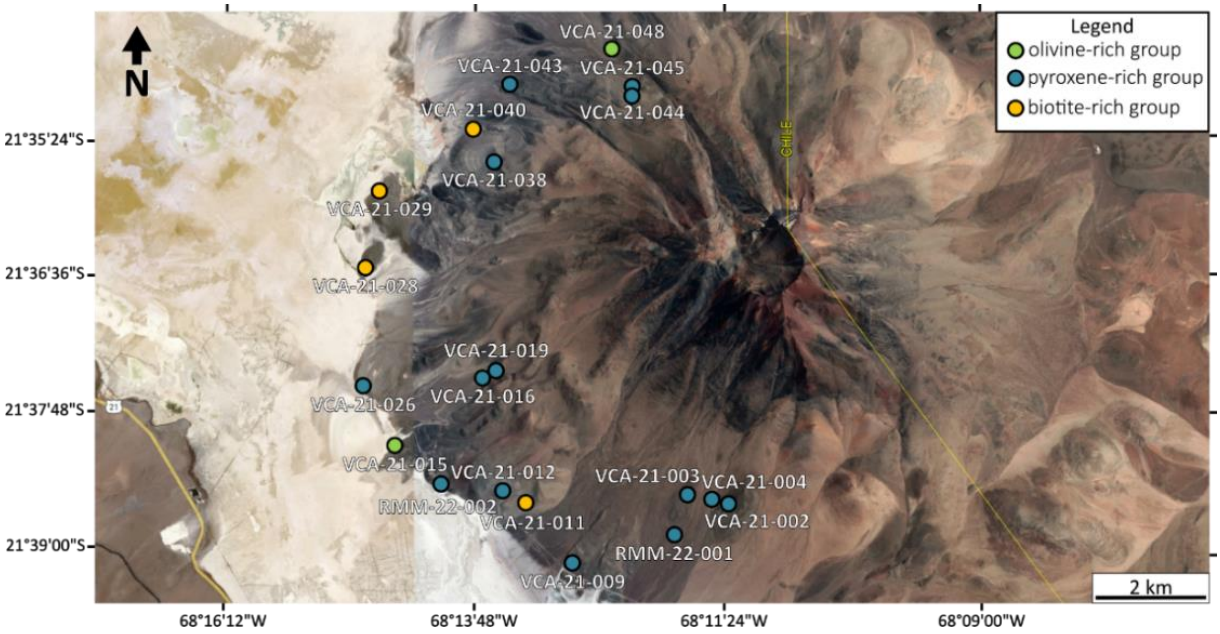

Figure 3.1. A satellite image showing the locations of samples collected from Araral (Google Earth, 22 March 2023).

Figure 3.2. (a) A picture of Araral taken from the southwest. (b) A picture of Salar de Ascotán taken from Araral. (c) A picture taken at the location of sample VCA-21-009. (d) A picture taken of the locations of samples VCA-21-016 and VCA-21-019 from the southwest. (e) A picture taken of the location of sample VCA-21-028 from the northwest. (f) A picture taken of the location of sample VCA-21-038 from the west.

Table 3.1. Sample location.

sample	longitude	latitude	elevation (m)
olivine-rich group			
VCA-21-015	68°14’38.33” W	21°38’10.53” S	3739
VCA-21-048	68°12’29.14” W	21°34’38.91” S	4112
pyroxene-rich group			
VCA-21-002	68°11’23.50” W	21°38’40.93” S	4074
VCA-21-003	68°11’32.10” W	21°38’39.35” S	4037
VCA-21-004	68°11’45.96” W	21°38’36.29” S	4050
VCA-21-009	68°12’53.67” W	21°39’13.92” S	3807
VCA-21-012	68°13’33.82” W	21°38’34.01” S	3774
VCA-21-016	68°13’45.27” W	21°37’33.40” S	3779
VCA-21-019	68°13’37.99” W	21°37’28.88” S	3944
VCA-21-026	68°14’56.77” W	21°37’37.66” S	3741
VCA-21-038	68°13’38.27” W	21°35’38.17” S	3978
VCA-21-043	68°13’30.28” W	21°34’56.05” S	3872
VCA-21-044	68°12’18.03” W	21°35’1.11” S	4113
VCA-21-045	68°12’18.01” W	21°35’4.88” S	4237
RMM-22-001	68°11’53.64” W	21°38’58.80” S	3915
RMM-22-002	68°14’10.32” W	21°38’33.42” S	3739
biotite-rich group			
VCA-21-011	68°13’20.90” W	21°38’41.85” S	3809
VCA-21-028	68°14’55.18” W	21°36’34.56” S	3770
VCA-21-029	68°14’47.15” W	21°35’52.21” S	3767
VCA-21-040	68°13’52.14” W	21°35’19.27” S	3792

3.2. Petrography:

20 thin sections (one from each sample) were analysed using an optical microscope (Leica DM EP microscope). All photomicrographs were taken using a Zeiss Axio Microscope in the Department of Geological Sciences, UCT.

3.3. X-Ray fluorescence (XRF) method (major elements):

Clean crucibles were weighed, 2.0 g of the rock powder was added, and the combined mass of the crucibles and the rock powder was recorded. The samples were dried in the oven at 110 °C for 4 hours, after which they were left to cool in a desiccator for 30 minutes and the mass was recorded again. The samples were then put in the furnace at 900 °C overnight.

After cooling in the desiccator for 30 minutes, the mass was recorded again. A 0.7 g measure of the sample and 6 g of lithium tetraborate/metaborate flux were put into small, labelled glass vials that were closed with both mylar film and a lid. These sample and flux mixtures were fused in a Claisse gas burner to make Claisse-Fluxy fusion discs for XRF analysis.

The fusion discs were analysed for major elements with a Panalytical Axios wavelength dispersive XRF spectrometer in the Department of Geological Sciences, UCT. The calibration curves used were obtained using the data from the analysis of well-characterised standards. These were standards with an identical preparation method as the samples – fusion discs of natural rock powders from MINTEK, the United States Geological Survey, and the Geological Society of Japan such as BE-N, JB-1, BHVO-1, JG-1, HUSG-1, and WITS-G. The concentration of the volatiles was calculated from the mass difference of the samples before and after they had dried in the oven. The loss of ignition was calculated from the mass difference of the samples before and after being put in the furnace overnight. The relative standard deviation (RSD) values for the analyses were ≤ 2%. The reported values obtained from the analysis of standard reference materials as unknowns are consistent with the accepted values.

3.4. Inductively coupled plasma-mass spectrometry (ICP-MS) method (trace elements):

Approximately 50 ± 1 mg of rock powder was added to a 7 ml Savillex PFA beaker, followed by 4 ml of 4:1 concentrated HF:HNO_3. The breakers were then closed and put on the hotplate to digest at 140 °C for 48 hours before being dried down. Once cooled, 2–3 ml 65% HNO_3 was added to the samples, and they were put back on the hot plate at 140 °C to dry down. The samples were then diluted with a solution of 5% HNO_3 containing 10 ppb of Rh, In, Re, and Bi used as internal standards. Then the samples were analysed for trace element concentrations using a Thermo-Fisher iCap RQ ICP-MS, in the Department of Geological Sciences, UCT. The quantitative data were obtained using calibration curves from artificial multi-element standard solutions. The RSD values for the analyses were ≤ 2.4%. The reported values obtained from the analysis of standard reference material JA-2 as an unknown are consistent with the accepted values.

3.5. Multi-collecter inductively coupled plasma-mass spectrometry (MC-ICP-MS) method (Sr-Nd-Pb isotopes):

Approximately 50 ± 1 mg of rock powder was added to a 7ml Savillex PFA beaker, followed by 4 ml of 4:1 concentrated HF:HNO_3. The breakers were then closed and put on the hotplate to digest at 140 °C for 48 hours. The samples were dried down at 140 °C. Once cooled, 2-3ml 65% HNO_3 was added to the samples, and they were again put on the hot plate at 140 °C to dry down. This step was repeated. After the samples had cooled down, 1.5 ml of 2M HNO_3 was added to the samples before they were left overnight. The samples were then put in a 1.5 ml centrifuge tube and centrifuged for 20 minutes at 4000 rpm.

The elemental separation of the samples followed sequential Sr, Pb, and Nd separation chemistry (after Pin et al., 2014). Initially, 1 ml of 2M HNO_3 was added to the Sr spec and TRU spec columns, simultaneously. This step was repeated once more. The columns were then stacked, with the Sr spec columns on top. Then 1 ml of 2M HNO_3 was added, followed by 0.75 ml and 0.7 ml of the sample solution, and then 0.5 ml of 2M HNO_3. The Sr spec and TRU spec columns were then disassembled and 0.5 ml of 2M HNO_3 was added to the Sr spec columns, followed by 0.5 ml of 7M HNO_3, 0.5 ml of 7M HNO_3 again, and then 0.5 ml of 2M HNO_3.

The waste beakers below the column were replaced with the clean 7 ml Savillex PFA beakers (labelled for Sr collection) and 0.5 ml of Milli-Q water was added to the Sr spec columns six times to collect the Sr fractions. The Sr collections beakers were then placed on the hot plate to dry down at 140 °C. After the beakers had dried and cooled, 1 ml of 0.2% HNO_3 was added to the beakers. The closed beakers were then put on the hotplate for 10 minutes at 100 °C.

Clean 7 ml Savillex PFA beakers (labelled for Pb collection) were placed beneath the Sr spec columns and then 0.5 ml of 6M HCl was added four times. The Pb collection beakers were then left to dry down on the hot plate at 140 °C. Then 1 ml of 65% HNO_3 was added and then dried down at 140 °C on the hotplate, this was repeated once. The beakers were then left to cool before 1 ml of 2% HNO_3 was added. The closed beakers were then put on the hot plate at 140 °C for 10 minutes.

A 0.5 ml aliquot of 2M HNO_3 was added to the TRU spec columns, this was repeated once, and followed by aliquots of 0.25 ml, 1 ml, and 1 ml of 0.05M HNO_3. The columns were then

stacked, with the Ln spec columns at the bottom. Then 0.5 ml of 0.05M HNO_3 was added six times to transfer the LREE from the TRU spec columns to the Ln spec columns. The columns were then separated and 0.5 ml of 0.05M HNO_3 was added to the Ln spec columns twice. This was followed by the addition of 1 ml, another 1 ml, 5 ml, and then 1 ml of 0.25M HCl. Clean 15 ml Savillex PFA beakers (labelled for Nd collection) were then placed beneath the Ln spec columns and Nd collected with the addition of 1 ml, another 1 ml, 5 ml, and then 1 ml of 0.25M HCl. The Nd collection beakers were then put on the hotplate to dry down at 140 °C. Then 1 ml of 65% HNO_3 was added and then dried down on the hotplate at 140 °C, this was repeated. The beakers were then left to cool before 2 ml of 2% HNO3 was added. The closed beakers were then put on the hot plate at 140 °C for 10 minutes.

The samples were analysed for Sr-Nd-Pb isotope compositions using Nu Instruments NuPlasma HR instrument in the MC-ICP-MS facility in the Department of Geological Sciences, UCT. The Sr isotopes were analysed as 200 ppb Sr solutions in 0.2% HNO_3 using NIST SRM987 as a reference standard and the values were normalised to an $^{87}Sr/^{86}Sr$ normalizing value of 0.710255 (Waight et al., 2002). For the Sr isotope data, the measured signal for ^{85}Rb and the natural $^{85}Rb/^{87}Rb$ ratio were used to correct for Rb interference. The exponential law and an $^{86}Sr/^{88}Sr$ value of 0.1194 were used to correct instrument mass fractionation, while Kr interference was subtracted using an on-peak background measurement. The two standard deviations (2σ) values for $^{87}Sr/^{86}Sr$ analyses were ≤0.000016. The Nd isotopes were analysed as 50 ppb Nd solutions in 2% HNO_3 also using a Nu Instruments DSN-100 desolvating nebuliser and with JNdi-1 as a reference standard. The Nd isotope ratios were normalised to a $^{143}Nd/^{144}Nd$ value of 0.512115 (Tanaka et al., 2000). For the Nd isotope data, the measured signal for ^{147}Sm and ^{140}Ce, and natural Sm and Ce isotope abundances were used to correct for Sm and Ce interference. The exponential law and a $^{146}Nd/^{144}Nd$ value of 0.7219 were used to correct instrumental mass fractionation. The 2σ values for $^{143}Nd/^{144}Nd$ analyses were ≤0.000018. The Pb isotopes were analysed as 50 ppb Pb solutions in 2% HNO_3 again using a Nu Instruments DSN-100 desolvating nebuliser and with NIST SRM981 as a reference standard. A NIST SRM997 Tl standard was added to the standards and samples to produce a 10:1 Pb:Tl ratio. The Pb isotope values were normalised using $^{208}Pb/^{204}Pb$, $^{207}Pb/^{204}Pb$, and $^{206}Pb/^{204}Pb$ values of 36.7219, 15.4963, and 16.9405, respectively (Galer and Abouchami, 1998). For Pb isotope data, Hg interference was corrected using an on-peak background

measurement, and the instrumental mass fractionation was corrected using the exponential law and a $^{205}Tl/^{203}Tl$ value of 2.3889 for NIST997. The 2σ values for $^{208}Pb/^{204}Pb$, $^{207}Pb/^{204}Pb$, and $^{206}Pb/^{204}Pb$ analyses were ≤ 0.0032, 0.0010, and 0.0011, respectively. The reported values for reference material JA-2 analysed as unknown with the project samples are $^{87}Sr/^{86}Sr$ = 0.706355 ± 0.000013, $^{143}Nd/^{144}Nd$ = 0.512532 ± 0.000024, $^{208}Pb/^{204}Pb$ = 38.6730 ± 0.0085, $^{207}Pb/^{204}Pb$ = 15.6060 ± 0.0028, and $^{206}Pb/^{204}Pb$ = 18.4011 ± 0.0020. The values are in good agreement with accepted values for JA-2 ($^{87}Sr/^{86}Sr$ = 0.706331 – 0.706372, $^{143}Nd/^{144}Nd$ = 0.512520 – 0.512576, $^{208}Pb/^{204}Pb$ = 38.6249 – 38.6680, $^{207}Pb/^{204}Pb$ = 15.5940 – 15.5980, and $^{206}Pb/^{204}Pb$ = 18.3906 – 18.3940). Total procedural blanks processed with these samples were typical for this facility, with values for Sr < 250 pg, Nd < 50 pg and Pb < 150 pg and therefore negligible.

3.6. Sample selection and laser fluorination (O isotopes):

For oxygen isotope analysis, the samples with the highest and lowest SiO_2 wt% were chosen from each group that contained clinopyroxene and/or olivine phenocrysts. From the olivine-rich group: samples VCA-21-015 and VCA-21-048; from the pyroxene-rich group: samples VCA-21-004 (third most mafic), VCA-21-012 (most felsic), and VCA-21-044 (most mafic); from the biotite-rich group: samples VCA-21-029 (most mafic) and VCA-21-040 (most felsic). Three samples, instead of two, were chosen from the pyroxene-rich group because it has the largest number of samples. However, the second most mafic sample was located relatively close to sample VCA-21-044 and thus the third most mafic sample (VCA-21-004) was chosen instead. The clinopyroxene and plagioclase crystals were picked under a binocular microscope.

The clinopyroxene and plagioclase crystals were analysed with Laser Fluorination in the Department of Geological Sciences, UCT. The methods follow those of Harris and Vogeli (2010). The laser system uses a 20 W New Wave CO_2 laser mounted on a moveable stage. The samples (1 – 3 mg) and two standards were put into a pure Ni sample holder, and MONGT (monastery garnet) was used as an internal standard. The sample holder was put in the oven at 110 °C for a minimum of an hour, before being moved to the reaction chamber. The reaction chamber then underwent a minimum of 2 hours of pumping. Then ~ 10 kPa of

BrF_5 was expanded into the reaction chamber for 30 seconds before being cryogenically removed. The chamber was then pumped again for 30 minutes. Then 10 kPa of BrF_5 was expanded into the reaction chamber and left overnight. After the reaction was complete, excess BrF_5 and Br (formed from dissociation) were frozen into a cold finger. The remaining gases were passed through the KCl trap maintained at ~ 200 °C to remove F_2. This was followed by the gases being expanded into a stainless-steel double-U trap that was immersed in liquid nitrogen and the collection of purified O_2 onto 5 Å molecular sieves within glass bottles. The O isotope data was measured using a Thermo Delta Mass Spectrometer in the Department of Archaeology, UCT.

The O isotope data are reported in δ-notation relative to V-SMOW (Standard Mean Ocean Water):

$$\delta = \left(\frac{\frac{^{18}O}{^{16}O}_{sample}}{\frac{^{18}O}{^{16}O}_{V-SMOW}} - 1 \right) * 1000$$

And the data was normalised using measured O isotope values of MONGT ($\delta^{18}O$ = 5.38‰).

4. Results:

4.1. Petrography:

The samples are hypocrystalline, porphyritic, and glomeroporphyritic with a glassy groundmass and microlites (fig. 4.1). The phenocrysts constitute 40 – 75% of the volume of rocks and the crystal size of the phenocrysts ranges from <0.25 mm to 3 mm. The phenocryst phases are, in order of decreasing abundance, plagioclase, clinopyroxene, orthopyroxene, opaque mineral(s), biotite, hornblende, and olivine. The crystal shapes are anhedral to euhedral for plagioclase crystals, anhedral to subhedral for clinopyroxene crystals, anhedral to subhedral for orthopyroxene crystals, subhedral to euhedral for biotite crystals, subhedral to euhedral for hornblende crystals, and anhedral to subhedral for olivine crystals. The plagioclase crystals exhibit oscillatory zoning, sieve textures as well as, Carlsbad, albite, and periclase twinning (fig. 4.1 a, c, d, e, h, and i). Plagioclase is the most abundant mineral among the phenocrysts, it constitutes about 37 – 63% of the phenocrysts. The largest phenocrysts in the samples are also typically plagioclase, with crystals up to 3 mm in size. Some clinopyroxene and orthopyroxene crystals exhibit simple twinning (fig. 4.1c). There are opacitic rims on some amphibole and biotite crystals (fig. 4.1 h and i).

Some samples that have pyroxene as the most abundant phenocryst assemblage, have two distinct types of groundmass: (1) a darker groundmass that rarely contains microlites, sometimes has a reddish colour in XPL and a red rim surrounding phenocrysts within it; and (2) a lighter groundmass, where microlites are common and less fine than those in the darker groundmass (fig. 4.1 d and e). These have various shapes in relation to one another: continuous, discontinuous, layered, elongated, and irregular. In some samples, the phenocrysts and microlites appear to be aligned in a preferred direction. Sample RMM-22-001 exhibits spherulites and devitrification (fig. 4.1 f and g).

Petrographic analyses of Araral samples are summarised in Table 4.1. More petrographic details are provided in the Supplementary Material 1 (Table S1). The samples were grouped according to their most abundant mafic phase(s), there are three groups: olivine-rich group (n = 2); pyroxene-rich group (n = 14); and biotite-rich group (n = 4) – in this group, the most abundant mafic phases are biotite and/or hornblende.

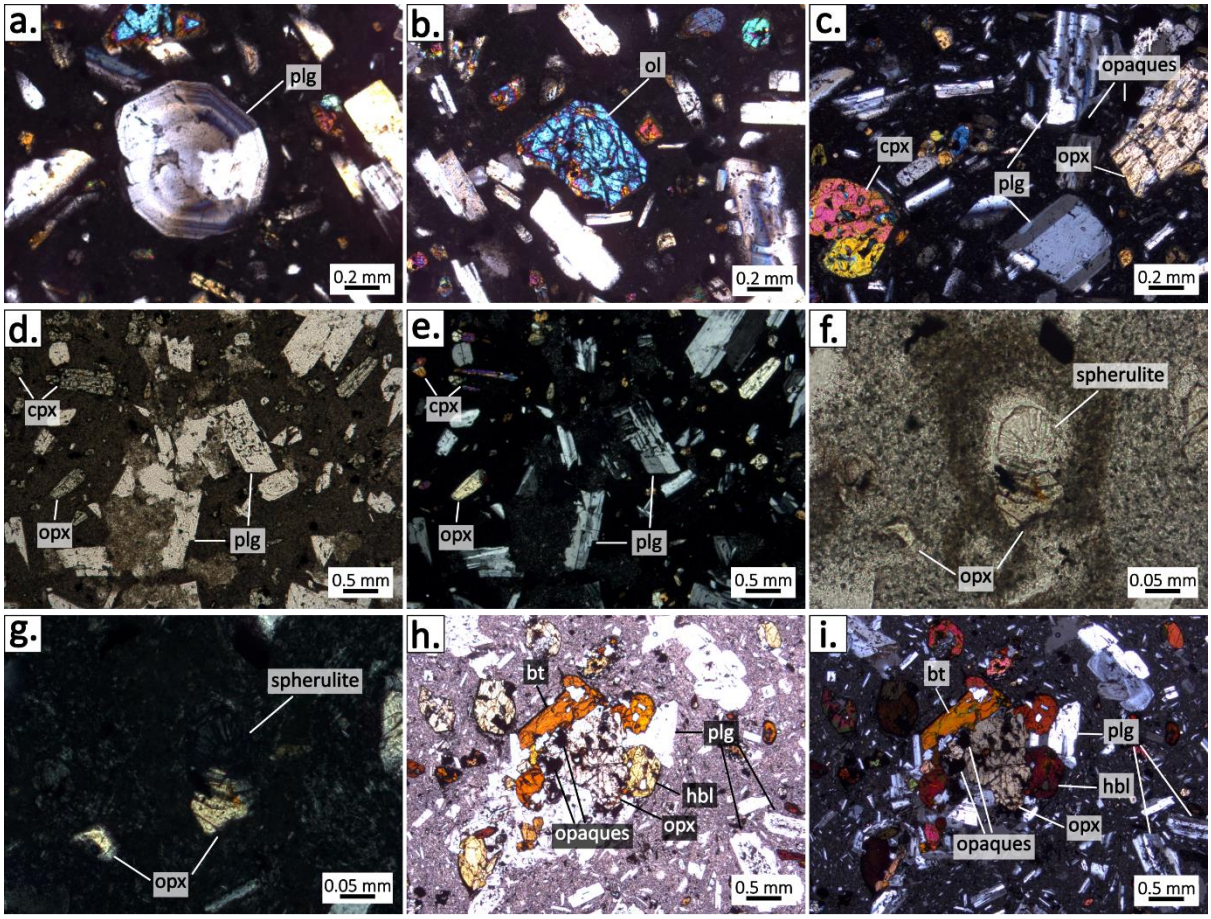

Figure 4.1. Photomicrographs of selected samples from the olivine-rich group (a – b), the pyroxene-rich group (c – g), and the biotite-rich group (h – i). (a) Oscillatory zoning in plagioclase in cross-polarised light (XPL) from sample VCA-21-048. (b) Olivine in XPL from sample VCA-21-048. (c) Porphyritic texture with phenocrysts of plagioclase, clinopyroxene, orthopyroxene, and opaque mineral(s) in XPL from sample VCA-21-004. (d) Porphyritic texture with light and dark groundmass, along with plagioclase, clinopyroxene, and orthopyroxene phenocrysts in plane polarised light (PPL) from sample VCA-21-002. (e) Porphyritic texture with light and dark groundmass, along with plagioclase, clinopyroxene, and orthopyroxene phenocrysts in XPL from sample VCA-21-002. (f) A spherulite in PPL from sample RMM-22-001. (g) A spherulite in XPL from sample RMM-22-001. (h) A glomerocryst with orthopyroxene, plagioclase, hornblende, biotite, and opaque mineral(s) in PPL from sample VCA-21-029. (i) A glomerocryst with orthopyroxene, plagioclase, hornblende, biotite, and opaque mineral(s) in XPL from sample VCA-21-029. bt – biotite, cpx – clinopyroxene, hbl – hornblende, plg – plagioclase, ol – olivine, opx – orthopyroxene.

Table 4.1. Rock classification and petrography summary.

sample	SiO_2 (wt%)	classification	rock description	phenocryst assemblage
olivine-rich group				
VCA-21-015	61.95	andesite	hypocrystalline, porphyritic, glomeroporphyritic, glassy groundmass with microlites	plg > ol > cpx = opaque mineral(s) > opx = hbl = bt
VCA-21-048	61.98	andesite	hypocrystalline, porphyritic, glomeroporphyritic, glassy groundmass with microlites	plg > ol = cpx = opaque mineral(s)
pyroxene-rich group				
VCA-21-002	61.95	andesite	hypocrystalline, porphyritic, glomeroporphyritic, glassy groundmass with microlites	plg > opx = cpx > opaque mineral(s)
VCA-21-003	61.30	andesite	hypocrystalline, porphyritic, glomeroporphyritic, glassy groundmass with microlites	plg > opx = cpx > opaque mineral(s)
VCA-21-004	60.30	andesite	hypocrystalline, porphyritic, glomeroporphyritic, glassy groundmass with microlites	plg > opx = cpx > opaque mineral(s)
VCA-21-009	62.53	andesite	hypocrystalline, porphyritic, glomeroporphyritic, glassy groundmass	plg > opx > cpx > opaque mineral(s)
VCA-21-012	65.88	dacite	hypocrystalline, porphyritic, glomeroporphyritic, glassy groundmass with microlites	plg > opx = cpx > bt = opaque mineral(s)
VCA-21-016	64.16	dacite	hypocrystalline, porphyritic, glomeroporphyritic, glassy with microlites	plg > opx = cpx > opaque mineral(s) > bt
VCA-21-019	65.09	dacite	hypocrystalline, porphyritic, glomeroporphyritic, glassy groundmass with microlites	plg > cpx > opaque mineral(s) > hbl > bt = opx
VCA-21-026	65.42	dacite	hypocrystalline, porphyritic, glomeroporphyritic, glassy groundmass with microlites	plg > cpx > opague mineral(s)
VCA-21-038	63.29	dacite	hypocrystalline, porphyritic, glomeroporphyritic, glassy groundmass with microlites	plg > opx > cpx > opaque mineral(s) >> ol
VCA-21-043	59.92	andesite	hypocrystalline, porphyritic, glomeroporphyritic, glassy groundmass with microlites	plg > cpx > hbl > opx > bt
VCA-21-044	59.89	andesite	hypocrystalline, porphyritic, glomeroporphyritic, glassy groundmass with microlites	plg > opx = cpx > bt > opaque mineral(s) > hbl
VCA-21-045	63.39	dacite	hypocrystalline, porphyritic, glomeroporphyritic, glassy groundmass with microlites	plg > opx > cpx > opaque mineral(s)
RMM-22-001	61.41	andesite	hypocrystalline, porphyritic, glomeroporphyritic, glassy groundmass with microlites, spherulites, and devitrification	plg > opx > cpx > opaque mineral(s)
RMM-22-002	61.35	andesite	hypocrystalline, porphyritic, glomeroporphyritic, glassy groundmass with microlites	plg > opx > cpx = opaque mineral(s) > bt > hbl
biotite-rich group				
VCA-21-011	63.44	dacite	hypocrystalline, porphyritic, glomeroporphyritic, glassy groundmass	plg > bt = opaque mineral(s) > cpx
VCA-21-028	61.30	andesite	hypocrystalline, porphyritic, glomeroporphyritic, glassy groundmass with microlites	plg > opx = bt > hbl = opaque mineral(s)
VCA-21-029	61.88	andesite	hypocrystalline, porphyritic, glomeroporphyritic, glassy groundmass with microlites	plg > hbl > opx = bt > opaque mineral(s) > cpx
VCA-21-040	67.16	dacite	hypocrystalline, porphyritic, glomeroporphyritic, glassy groundmass with microlites	plg > bt = cpx > opaque mineral(s)

4.2. Geochemistry:

4.2.1. Major elements:

The lavas of Araral are subalkaline and high-K calc-alkaline, and only one sample (RMM-22-001) is medium-K calc-alkaline (fig. 4.2). The olivine-rich group is andesitic (fig. 4.2a) with SiO_2 of 61.95 and 61.98 wt% and MgO of 3.01 and 3.07 wt% (table 4.2). The samples of the pyroxene-rich group are andesites and dacites (fig. 4.2a) with SiO_2 and MgO contents ranging from 59.89 to 65.88 wt%, and 1.96 to 3.46 wt%, respectively (table 4.2). The biotite-rich group is andesitic and dacitic (fig. 4.2a). The SiO_2 and MgO values are 61.30 – 67.16 and 1.57 – 2.69 wt%, respectively (table 4.2). Classification of the Araral samples is summarised in Table 4.1.

For the pyroxene-rich group, SiO_2 shows a strong positive linear correlation with K_2O (fig. 4.2b); a weak negative linear correlation with NaO_2 (fig. 4.3f); a negative linear correlation with Al_2O_3 (fig. 4.3e); strong negative linear correlations with FeO*, MgO, CaO, and TiO_2 (fig. 4.3 a – d). For the biotite-rich group, SiO_2 has a strong positive linear correlation with K_2O (fig. 4.2b); no linear correlation with NaO_2 (fig. 4.3f); strong negative linear correlations with FeO*, MgO, CaO, TiO_2, and Al_2O_3 (fig. 4.3 a – e).

The Mg# are 50.30 and 52.84, 46.25 – 52.90, and 42.15 – 49.64, for the olivine-rich, pyroxene-rich, and biotite-rich groups, respectively (table 4.2). Where $Mg\# = \frac{100*M}{M+F}$, $M = \frac{MgO}{40.30}$, and $F = \frac{FeO*}{71.84}$. All the samples in the olivine-rich group have Mg# > 50. In the pyroxene-rich group, 5 samples have Mg# <50 and they are all dacites, and only one dacite (VCA-21-012) has Mg# >50. All the samples in the biotite-rich group have Mg# <50. The two andesites in the group have the highest Mg#, both have Mg# >49 and are the only two andesites in the entire sample set with Mg# <50.

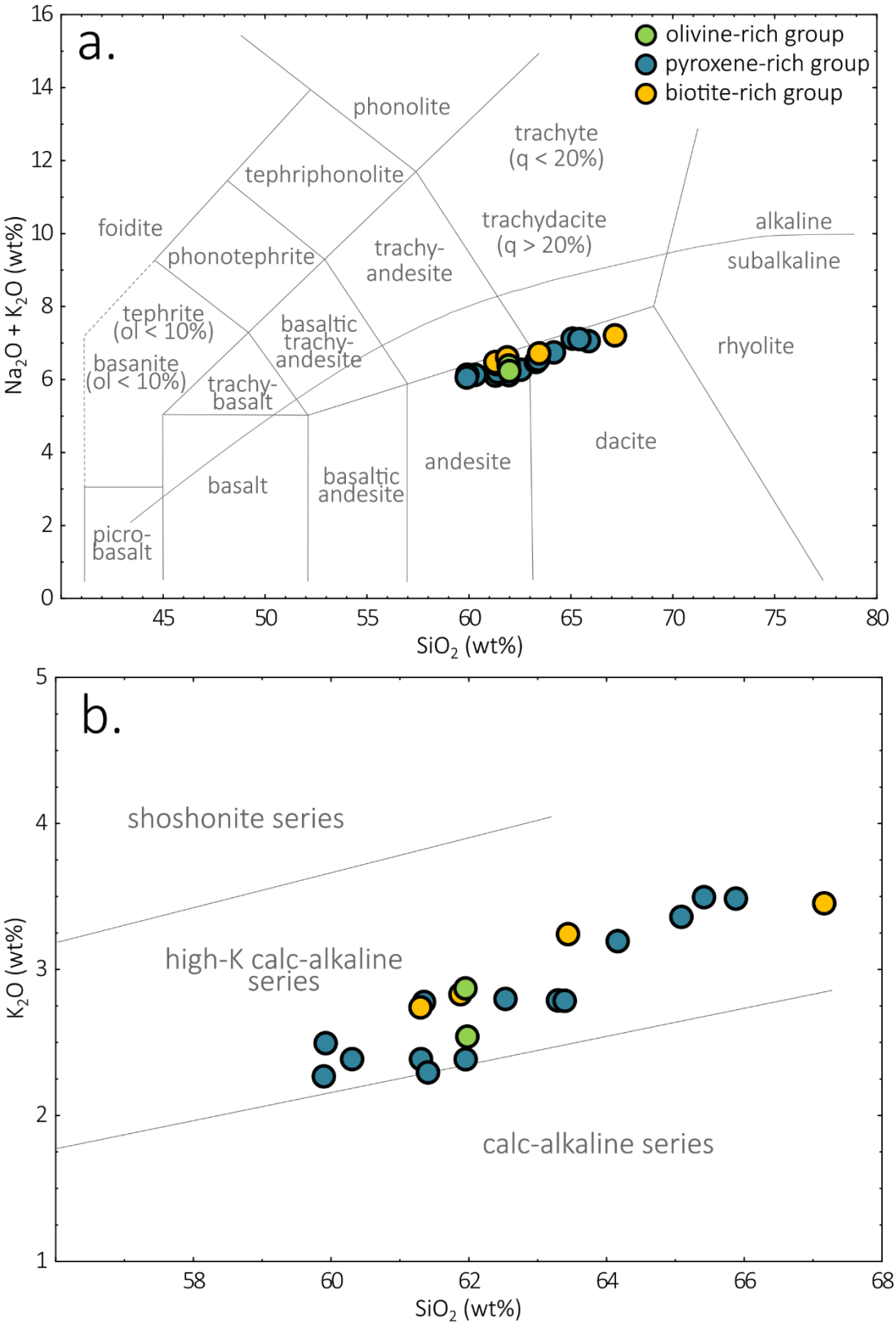

Figure 4.2. (a) Total alkali vs silica (TAS) diagram (Irvine and Bargar, 1971; Le Maitre et al., 1989). (b) K_2O vs SiO_2 classification diagram (Rickwood, 1989).

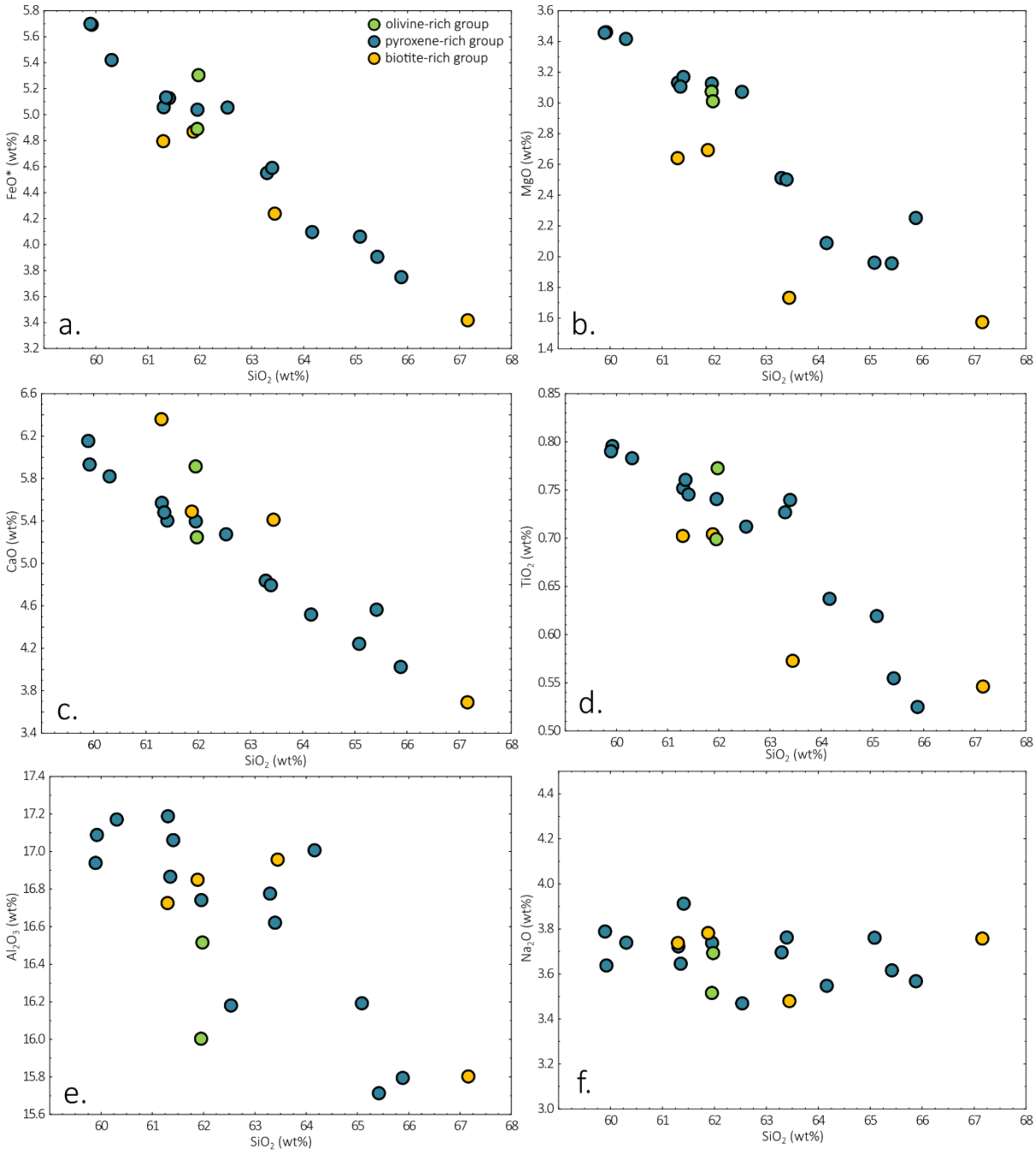

Figure 4.3. Major oxides vs SiO_2. (a) FeO* vs SiO_2. (b) MgO vs SiO_2. (c) CaO vs SiO_2. (d) TiO_2 vs SiO_2. (e) Al_2O_3 vs SiO_2. (f) Na_2O vs SiO_2.

Table 4.2. Major oxides in wt%.

	olivine-rich group		*pyroxene-rich group*							
sample	VCA-21-015	VCA-21-048	VCA-21-002	VCA-21-003	VCA-21-004	VCA-21-009	VCA-21-012	VCA-21-016	VCA-21-019	VCA-21-026
SiO_2	61.95	61.98	61.95	61.30	60.30	62.53	65.88	64.16	65.09	65.42
TiO_2	0.70	0.77	0.74	0.75	0.78	0.71	0.52	0.64	0.62	0.55
Al_2O_3	16.00	16.52	16.74	17.19	17.17	16.18	15.79	17.01	16.19	15.71
Fe_2O_3	5.44	5.90	5.60	5.62	6.03	5.62	4.17	4.55	4.51	4.34
MnO	0.09	0.09	0.09	0.08	0.09	0.09	0.07	0.07	0.07	0.08
MgO	3.07	3.01	3.13	3.13	3.42	3.07	2.25	2.09	1.96	1.96
CaO	5.91	5.25	5.40	5.57	5.82	5.27	4.02	4.52	4.24	4.56
Na_2O	3.52	3.69	3.74	3.72	3.74	3.47	3.57	3.55	3.76	3.62
K_2O	2.87	2.54	2.39	2.39	2.39	2.80	3.49	3.19	3.36	3.50
P_2O_5	0.19	0.22	0.22	0.22	0.22	0.20	0.17	0.22	0.19	0.17
SO_3	0.23	0.03		0.01		0.04	0.01			0.09
Cr_2O_3	0.01	0.01	0.01	0.01	0.01	0.01	0.01			
NiO	0.01				0.03		0.04			
Sum	100	100	100	100	100	100	100	100	100	100
H_2O-	2.05	0.70	0.97	0.95	0.24	0.32	1.11	6.98	0.30	0.34
LOI	2.07	1.25	1.13	1.47	0.80	1.53	1.38	1.67	0.27	1.64
FeO*	4.89	5.30	5.04	5.06	5.42	5.06	3.75	4.10	4.06	3.91
Mg#	52.84	50.30	52.52	52.46	52.90	51.99	51.70	47.60	46.25	47.17

Table 4.2. Major elements in wt% (continued).

	pyroxene-rich group						*biotite-rich group*			
sample	VCA-21-038	VCA-21-043	VCA-21-044	VCA-21-045	RMM-22-001	RMM-22-002	VCA-21-011	VCA-21-028	VCA-21-029	VCA-21-040
SiO_2	63.29	59.92	59.89	63.39	61.41	61.35	63.44	61.30	61.88	67.16
TiO_2	0.73	0.80	0.79	0.74	0.75	0.76	0.57	0.70	0.70	0.55
Al_2O_3	16.78	17.09	16.94	16.62	17.06	16.87	16.96	16.73	16.85	15.80
Fe_2O_3	5.06	6.33	6.33	5.10	5.70	5.71	4.71	5.33	5.41	3.80
MnO	0.07	0.10	0.10	0.09	0.08	0.08	0.08	0.10	0.09	0.06
MgO	2.51	3.46	3.46	2.50	3.17	3.11	1.73	2.64	2.69	1.57
CaO	4.84	5.93	6.15	4.80	5.40	5.48	5.41	6.36	5.49	3.69
Na_2O	3.70	3.64	3.79	3.76	3.91	3.65	3.48	3.74	3.78	3.76
K_2O	2.79	2.50	2.27	2.79	2.29	2.78	3.24	2.74	2.83	3.45
P_2O_5	0.22	0.22	0.22	0.21	0.21	0.22	0.24	0.22	0.23	0.15
SO_3			0.04			0.00	0.13	0.13	0.04	0.01
Cr_2O_3	0.02	0.01	0.01	0.01	0.01	0.01		0.01	0.01	0.00
NiO		0.01						0.01		
Sum	100	100	100	100	100	100	100	100	100	100
H_2O^-	1.11	0.10	0.21	0.17	0.24	0.40	0.91	0.62	0.19	0.24
LOI	0.75	0.75	0.80	0.84	0.70	1.78	2.58	1.89	1.43	1.40
FeO*	4.55	5.69	5.70	4.59	5.13	5.13	4.24	4.80	4.87	3.42
Mg#	49.59	52.01	51.95	49.28	52.42	51.89	42.15	49.54	49.64	45.08

*Major oxides are calculated to 100% anhydrous

$Mg\# = \frac{100*M}{M+F}$, $M = \frac{MgO}{40.30}$, and $F = \frac{FeO*}{71.84}$

4.2.2. Trace elements.

For Figure 4.4, the trace elements were normalised using values from Sun and McDonough (1989) for the primitive mantle and chondrite values, respectively. The incompatible trace element and REE patterns of all three groups have the same characteristics. Figure 4.4a shows that the samples are enriched in LILE with respect to high field strength elements (HFSE) and have negative Nb-Ta anomalies and Rb, Th, U, Pb, and Sr enrichments. The REE patterns show that the samples are LREE enriched with shallow slopes (low LREE/HREE ratios) and very weak negative Eu anomalies (fig. 4.4b). The Eu anomaly (Eu/Eu* = $\frac{Eu_N}{(Sm_N * Gd_N)^{0.5}}$) values are 0.85, 0.76 – 0.92, and 0.81 – 0.90, for the olivine-rich, pyroxene-rich, and biotite-rich groups, respectively (table 4.3). The Sr/Y ratios for the olivine-rich, pyroxene-rich, and biotite-rich groups are 20.98 and 23.84, 18.70 – 35.85, and 21.35 – 39.01, respectively (table 4.3). The ratios of lanthanum (La) to ytterbium (Yb) and dysprosium (Dy) to Yb both use chondrite normalised values. The La/Yb ratios are 12.64 and 14.94, 10.46 – 20.49, and 12.06 – 18.12 for the olivine-rich, pyroxene-rich, and biotite-rich groups respectively (table 4.3). The Dy/Yb ratios for the olivine-rich, pyroxene-rich, and biotite-rich groups are 1.28 and 1.48, 1.16 – 1.57, and 1.23 – 1.28, respectively (table 4.3).

For the pyroxene-rich group, SiO_2 has a strong positive linear correlation with Th (fig. 4.5d); a weak positive correlation with La/Yb (fig 4.6c); a weak negative linear correlation with Dy/Yb (fig 4.6d); negative linear correlations with Sr, Cr, Eu/Eu*, and Sr/Y (fig. 4.5 a and c; fig. 4.6 a and b); and a strong negative linear correlation with Ni (fig 4.5b). For the biotite-rich group, SiO_2 has strong positive linear correlations with Th and La/Yb (fig. 4.5d; fig. 4.6c); a weak positive correlation with Sr/Y and Dy/Yb (fig 4.6 b and d); negative linear correlations with Sr, Cr, Ni, and Eu/Eu* (fig. 4.5 a–c; fig. 4.6a).

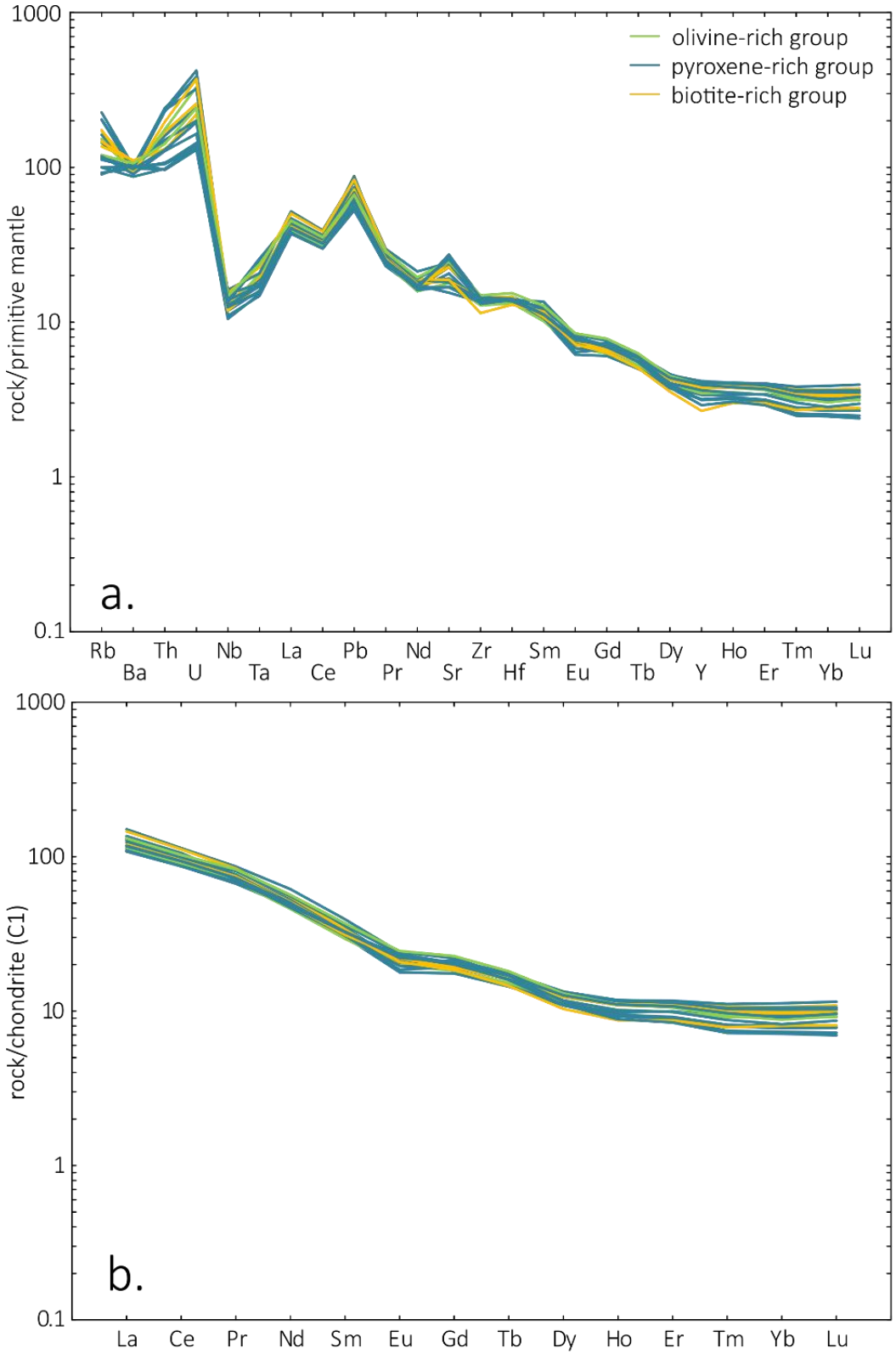

Figure 4.4. (a) Incompatible trace element diagram (trace element values normalised to primitive mantle values from Sun and McDonough, 1989). (b) Rare earth element diagram (REE values normalised to chondrite values from Sun and McDonough, 1989).

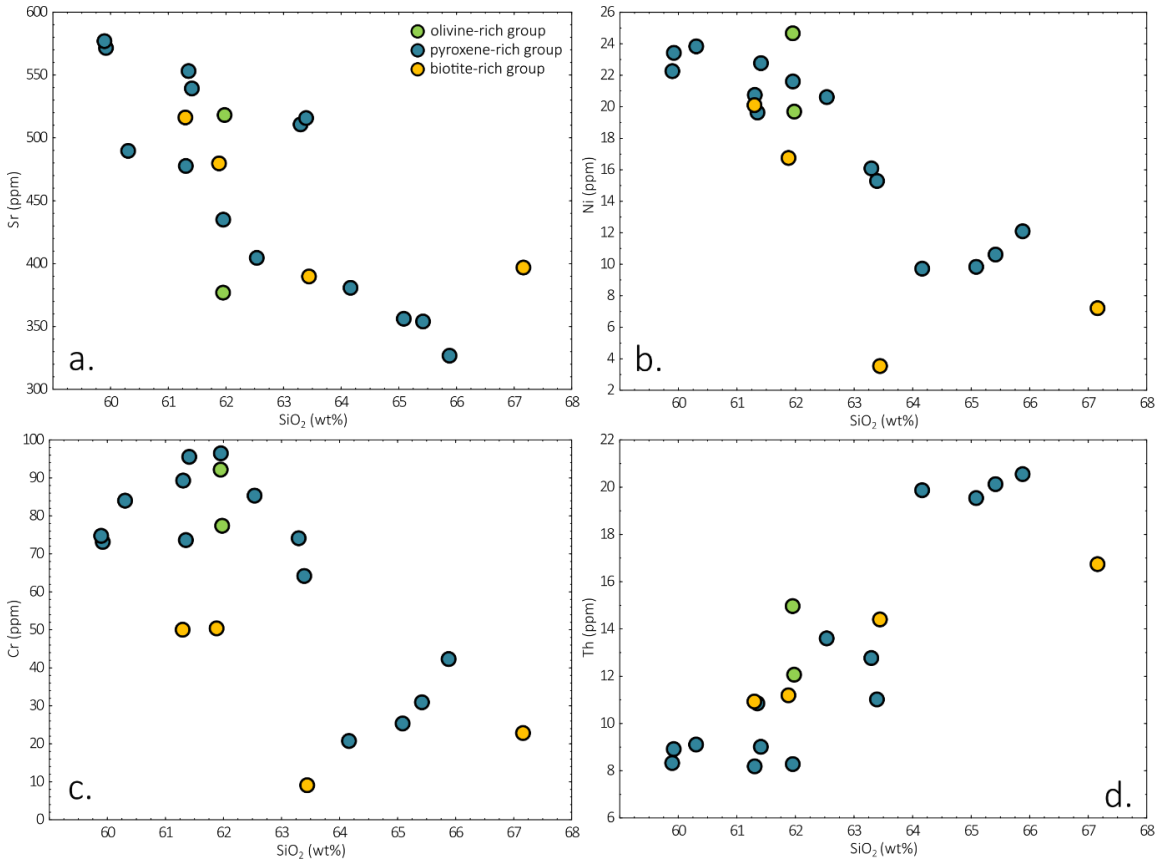

Figure 4.5. Trace elements vs SiO_2. (a) Sr vs SiO_2. (b) Ni vs SiO_2. (c) Cr vs SiO_2. (d) Th vs SiO_2.

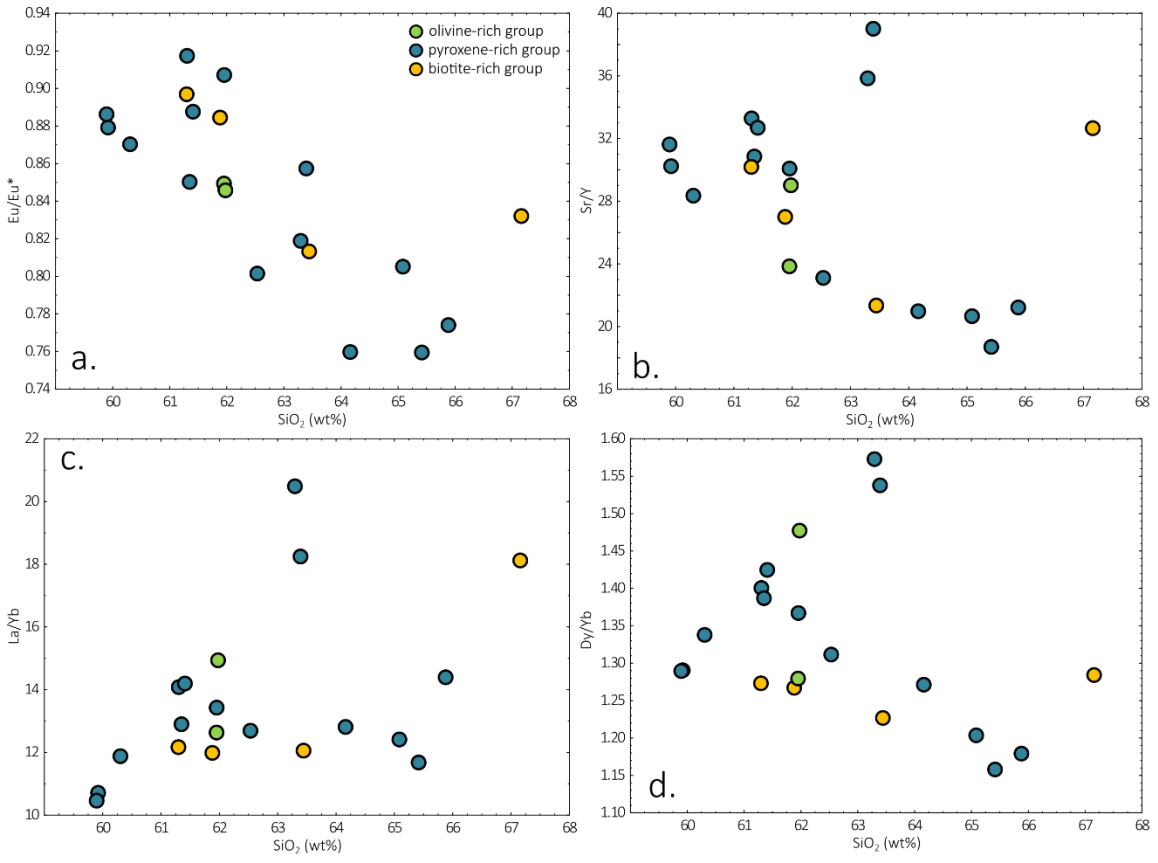

Figure 4.6. (a) Eu/Eu* vs SiO_2. (b) Sr/Y vs SiO_2. (c) La/Yb vs SiO_2. (d) Dy/Yb vs SiO_2.

Table 4.3. Trace element data in ppm.

	olivine-rich group		*pyroxene-rich group*				
sample	VCA-21-015	VCA-21-048	VCA-21-002	VCA-21-003	VCA-21-004	VCA-21-009	VCA-21-012
Li	22.83	33.13	20.86	23.59	19.96	21.54	26.60
Sc	11.25	12.86	12.29	12.19	14.77	12.24	9.67
V	134.64	132.85	138.61	141.92	153.20	134.94	85.33
Cr	92.18	77.41	96.48	89.30	84.04	85.35	42.29
Co	15.45	14.79	15.87	15.43	16.77	14.73	10.53
Ni	24.67	19.69	21.61	20.75	23.84	20.61	12.09
Cu	19.18	16.15	19.32	21.24	22.64	22.57	18.76
Zn	79.71	82.32	84.35	86.22	83.92	80.01	61.14
Rb	96.70	76.28	58.65	57.26	72.97	91.81	129.68
Sr	376.97	518.20	435.03	477.71	489.74	404.61	326.81
Y	15.81	17.86	14.46	14.35	17.27	17.51	15.40
Zr	143.57	166.98	148.64	155.19	154.58	154.98	151.04
Nb	8.66	10.54	7.50	7.83	8.45	8.54	9.59
Ba	645.77	742.72	686.70	749.05	692.13	691.13	698.01
La	27.10	31.14	25.60	25.90	26.72	29.27	32.19
Ce	54.96	62.76	53.04	54.64	55.22	59.79	64.59
Pr	6.57	7.86	6.35	6.63	6.85	7.27	7.15
Nd	21.43	26.45	22.12	22.56	23.42	24.27	23.48
Sm	4.50	5.67	4.72	4.75	4.99	5.08	4.64
Eu	1.14	1.42	1.25	1.26	1.29	1.21	1.04
Gd	3.75	4.66	3.75	3.74	4.11	4.16	3.60
Tb	0.57	0.68	0.55	0.54	0.62	0.62	0.54
Dy	2.94	3.30	2.79	2.76	3.22	3.24	2.83
Ho	0.58	0.62	0.54	0.52	0.62	0.63	0.56
Er	1.63	1.75	1.52	1.47	1.77	1.79	1.65
Tm	0.23	0.24	0.21	0.20	0.25	0.25	0.24
Yb	1.54	1.50	1.37	1.32	1.61	1.65	1.60
Lu	0.23	0.24	0.21	0.20	0.24	0.25	0.25
Hf	4.10	4.76	4.16	4.29	4.27	4.38	4.37
Ta	0.84	0.97	0.62	0.61	0.65	0.78	0.99
Pb	12.55	12.33	9.84	10.21	10.84	11.60	15.65
Th	14.97	12.06	8.28	8.19	9.11	13.60	20.55
U	6.94	5.07	2.85	2.73	2.88	5.10	7.82
Eu/Eu*	0.85	0.85	0.91	0.92	0.87	0.80	0.77
Sr/Y	23.84	29.02	30.09	33.29	28.35	23.11	21.22
La/Yb	12.64	14.94	13.43	14.08	11.88	12.70	14.39
Dy/Yb	1.28	1.48	1.37	1.40	1.34	1.31	1.18

Table 4.3. Trace element data in ppm (continued).

	pyroxene-rich group						
sample	VCA-21-016	VCA-21-019	VCA-21-026	VCA-21-038	VCA-21-043	VCA-21-044	VCA-21-045
Li	32.31	20.82	31.47	33.53	20.81	20.19	19.74
Sc	8.82	9.43	10.17	9.35	15.52	15.33	9.01
V	96.98	113.02	89.57	120.80	172.14	163.56	133.96
Cr	20.78	25.37	30.95	74.13	73.19	74.77	64.19
Co	11.01	10.71	10.55	12.91	18.98	18.46	13.76
Ni	9.73	9.84	10.61	16.09	23.42	22.26	15.29
Cu	24.10	19.81	67.96	13.53	22.69	28.79	15.30
Zn	72.82	70.42	74.03	90.09	84.59	79.42	88.19
Rb	103.10	129.10	143.69	71.20	73.96	63.48	74.91
Sr	380.76	356.17	354.01	510.80	571.51	576.99	515.79
Y	18.15	17.24	18.93	14.25	18.90	18.25	13.22
Zr	158.80	156.48	149.35	146.98	163.77	156.43	162.08
Nb	9.88	10.03	10.07	11.52	9.20	9.00	10.83
Ba	665.38	664.40	713.25	699.46	700.13	608.82	681.74
La	31.98	30.11	31.11	35.68	25.97	25.63	30.85
Ce	60.72	60.72	62.44	69.54	53.23	53.09	62.29
Pr	7.67	6.78	7.27	8.20	6.54	6.52	7.69
Nd	25.39	21.86	22.76	28.78	22.46	22.55	25.92
Sm	5.32	4.75	4.72	6.02	4.97	4.97	5.51
Eu	1.20	1.14	1.08	1.40	1.31	1.33	1.35
Gd	4.37	3.92	3.97	4.52	4.17	4.22	4.22
Tb	0.66	0.60	0.62	0.63	0.64	0.64	0.60
Dy	3.40	3.13	3.31	2.94	3.35	3.39	2.79
Ho	0.66	0.62	0.67	0.53	0.66	0.67	0.50
Er	1.86	1.80	1.93	1.45	1.90	1.91	1.40
Tm	0.27	0.26	0.28	0.19	0.26	0.27	0.18
Yb	1.79	1.74	1.91	1.25	1.74	1.76	1.21
Lu	0.27	0.27	0.29	0.18	0.26	0.26	0.18
Hf	4.50	4.51	4.37	4.32	4.30	4.22	4.35
Ta	1.02	1.05	1.05	0.85	0.70	0.64	0.73
Pb	13.74	15.13	16.26	15.50	10.01	9.76	12.73
Th	19.87	19.54	20.13	12.77	8.92	8.33	11.02
U	6.77	8.10	8.88	4.21	2.83	2.85	4.10
Eu/Eu*	0.76	0.81	0.76	0.82	0.88	0.89	0.86
Sr/Y	20.98	20.66	18.70	35.85	30.24	31.62	39.01
La/Yb	12.81	12.41	11.68	20.49	10.71	10.46	18.24
Dy/Yb	1.27	1.20	1.16	1.57	1.29	1.29	1.54

Table 4.3. Trace element data in ppm (continued).

	pyroxene-rich group		*biotite-rich group*			
sample	RMM-22-001	RMM-22-002	VCA-21-011	VCA-21-028	VCA-21-029	VCA-21-040
Li	21.08	49.14	29.29	27.50	28.75	34.45
Sc	15.51	14.56	7.37	11.89	11.91	5.96
V	147.41	144.72	83.01	127.98	127.56	81.82
Cr	95.55	73.63	9.11	50.04	50.41	22.83
Co	16.45	15.05	8.19	14.86	13.91	8.14
Ni	22.77	19.64	3.54	20.11	16.75	7.21
Cu	22.92	19.23	10.48	23.94	22.80	11.67
Zn	99.53	85.02	69.65	157.41	85.09	72.52
Rb	63.53	74.77	109.61	86.63	92.99	110.64
Sr	539.28	553.10	389.75	516.25	479.74	396.88
Y	16.50	17.93	18.26	17.10	17.77	12.15
Zr	160.23	160.28	159.57	160.11	161.49	128.21
Nb	8.92	9.90	9.52	8.49	8.62	10.92
Ba	705.90	632.99	702.19	778.59	771.53	640.43
La	27.67	27.87	30.31	27.95	28.47	34.51
Ce	57.15	57.38	61.25	57.05	58.05	68.20
Pr	6.91	6.90	7.30	6.91	7.08	7.96
Nd	23.34	23.10	23.79	22.63	23.18	25.65
Sm	4.99	4.98	4.92	4.78	4.93	5.18
Eu	1.32	1.28	1.19	1.27	1.30	1.21
Gd	4.12	4.27	4.07	3.94	4.08	3.80
Tb	0.60	0.63	0.62	0.60	0.62	0.54
Dy	2.98	3.21	3.31	3.13	3.23	2.62
Ho	0.57	0.62	0.66	0.62	0.64	0.49
Er	1.63	1.78	1.91	1.75	1.80	1.44
Tm	0.22	0.25	0.27	0.25	0.26	0.20
Yb	1.40	1.55	1.80	1.65	1.70	1.37
Lu	0.22	0.24	0.28	0.25	0.26	0.21
Hf	4.24	4.39	4.48	4.45	4.50	4.01
Ta	0.65	0.70	0.80	0.72	0.73	0.93
Pb	11.13	11.09	13.32	13.31	11.07	15.43
Th	9.02	10.85	14.40	10.93	11.19	16.74
U	3.02	3.46	5.43	4.63	4.13	7.80
Eu/Eu*	0.89	0.85	0.81	0.90	0.88	0.83
Sr/Y	32.69	30.85	21.35	30.19	27.00	32.67
La/Yb	14.20	12.90	12.06	12.17	11.98	18.12
Dy/Yb	1.42	1.39	1.23	1.27	1.27	1.28

$Eu/Eu^* = \frac{Eu_N}{(Sm_N * Gd_N)^{0.5}}$

4.2.3. Radiogenic Isotopes:

For the olivine-rich group, $^{87}Sr/^{86}Sr$ = 0707106 and 0.707245, $^{143}Nd/^{144}Nd$ = 0.512309 and 0.512342, $^{208}Pb/^{204}Pb$ = 38.8379 and 38.8712, $^{207}Pb/^{204}Pb$ = 15.6554 and 15.6608, and $^{206}Pb/^{204}Pb$ = 18.9268 and 18.9639 (table 4.4). For the pyroxene-rich group, $^{87}Sr/^{86}Sr$ = 0.706877 – 0.707828, $^{143}Nd/^{144}Nd$ = 0.512281 – 0.512368, $^{208}Pb/^{204}Pb$ = 38.8032 – 38.9191, $^{207}Pb/^{204}Pb$ = 15.6541 – 15.6640, and $^{206}Pb/^{204}Pb$ = 18.8861 – 19.0002 (table 4.4). For the biotite-rich group, $^{87}Sr/^{86}Sr$ = 0.707049 – 0.708521, $^{143}Nd/^{144}Nd$ = 0.512282 – 0.512343, $^{208}Pb/^{204}Pb$ = 38.8431 – 38.8993, $^{207}Pb/^{204}Pb$ = 15.6607 – 15.6660, and $^{206}Pb/^{204}Pb$ = 18.9233 – 18.9622 (table 4.4).

For the pyroxene-rich group, $^{87}Sr/^{86}Sr$ shows a positive linear correlation with SiO_2 (fig. 4.7a) and a weak negative correlation with elemental Sr concentrations (fig. 4.8a). $^{143}Nd/^{144}Nd$ does not correlate with SiO_2 (fig. 4.7b) and has weak negative linear correlations with elemental Nd (fig. 4.8b) and $^{87}Sr/^{86}Sr$ (fig. 4.9a). All the Pb isotope ratios have positive linear correlations with SiO_2 (fig. 4.7 c – e), elemental Pb (fig. 4.8 c – e) and each other (fig. 4.9 d – f). $^{208}Pb/^{204}Pb$ has a positive linear correlation with $^{87}Sr/^{86}Sr$ (fig. 4.9b) and no linear correlation with $^{143}Nd/^{144}Nd$ (fig. 4.9c). $^{207}Pb/^{204}Pb$ shows a positive linear correlation with $^{87}Sr/^{86}Sr$ and no linear correlation with $^{143}Nd/^{144}Nd$ (not shown). $^{206}Pb/^{204}Pb$ has a positive linear correlation with $^{87}Sr/^{86}Sr$ and no linear correlation with $^{143}Nd/^{144}Nd$ (not shown).

For the biotite-rich group, $^{87}Sr/^{86}Sr$ shows a near-perfect positive linear correlation with SiO_2 (fig. 4.7a) and a negative correlation with elemental Sr concentrations (fig. 4.8a). $^{143}Nd/^{144}Nd$ has strong negative correlations with SiO_2, elemental Nd, and $^{87}Sr/^{86}Sr$ (fig. 4.7b, 4.8b and 4.9a). All the Pb isotope ratios have positive linear correlations with SiO_2 (fig. 4.7 c – e), elemental Pb (fig. 4.8 c – e), and each other (fig. 4.9 d – f). $^{208}Pb/^{204}Pb$ has a strong positive linear correlation with $^{87}Sr/^{86}Sr$ (fig. 4.9b) and a negative linear correlation with $^{143}Nd/^{144}Nd$ (fig. 4.9c). $^{207}Pb/^{204}Pb$ shows a strong positive linear correlation with $^{87}Sr/^{86}Sr$ and a strong negative linear correlation with $^{143}Nd/^{144}Nd$ (not shown). $^{206}Pb/^{204}Pb$ has a strong positive linear correlation with $^{87}Sr/^{86}Sr$ and a negative linear correlation with $^{143}Nd/^{144}Nd$ (not shown).

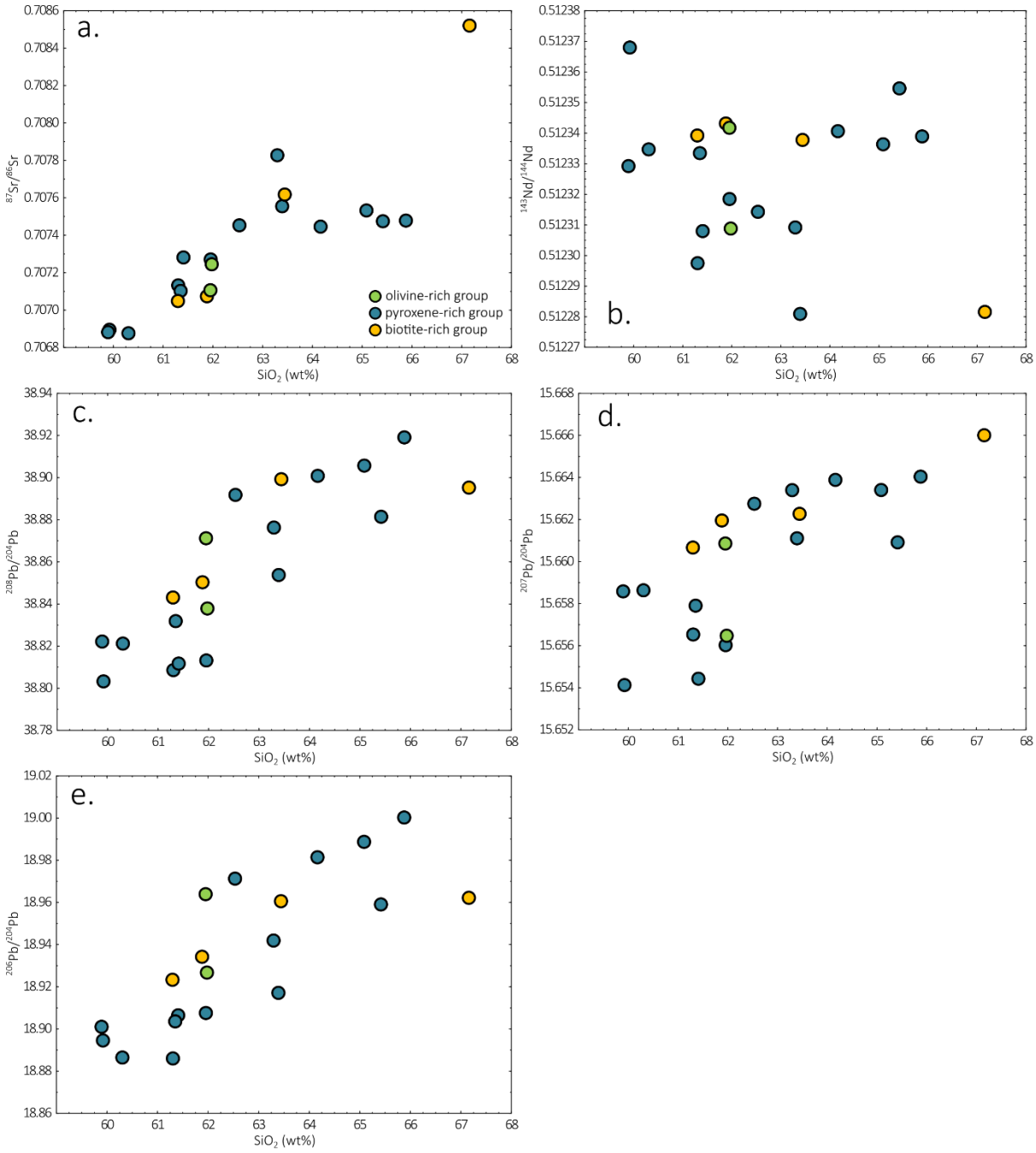

Figure 4.7. Radiogenic isotope ratios vs SiO_2. (a) $^{87}Sr/^{86}Sr$ vs SiO_2. (b) $^{143}Nd/^{144}Nd$ vs SiO_2. (c) $^{208}Pb/^{204}Pb$ vs SiO_2. (d) $^{207}Pb/^{204}Pb$ vs SiO_2. (e) $^{206}Pb/^{204}Pb$ vs SiO_2.

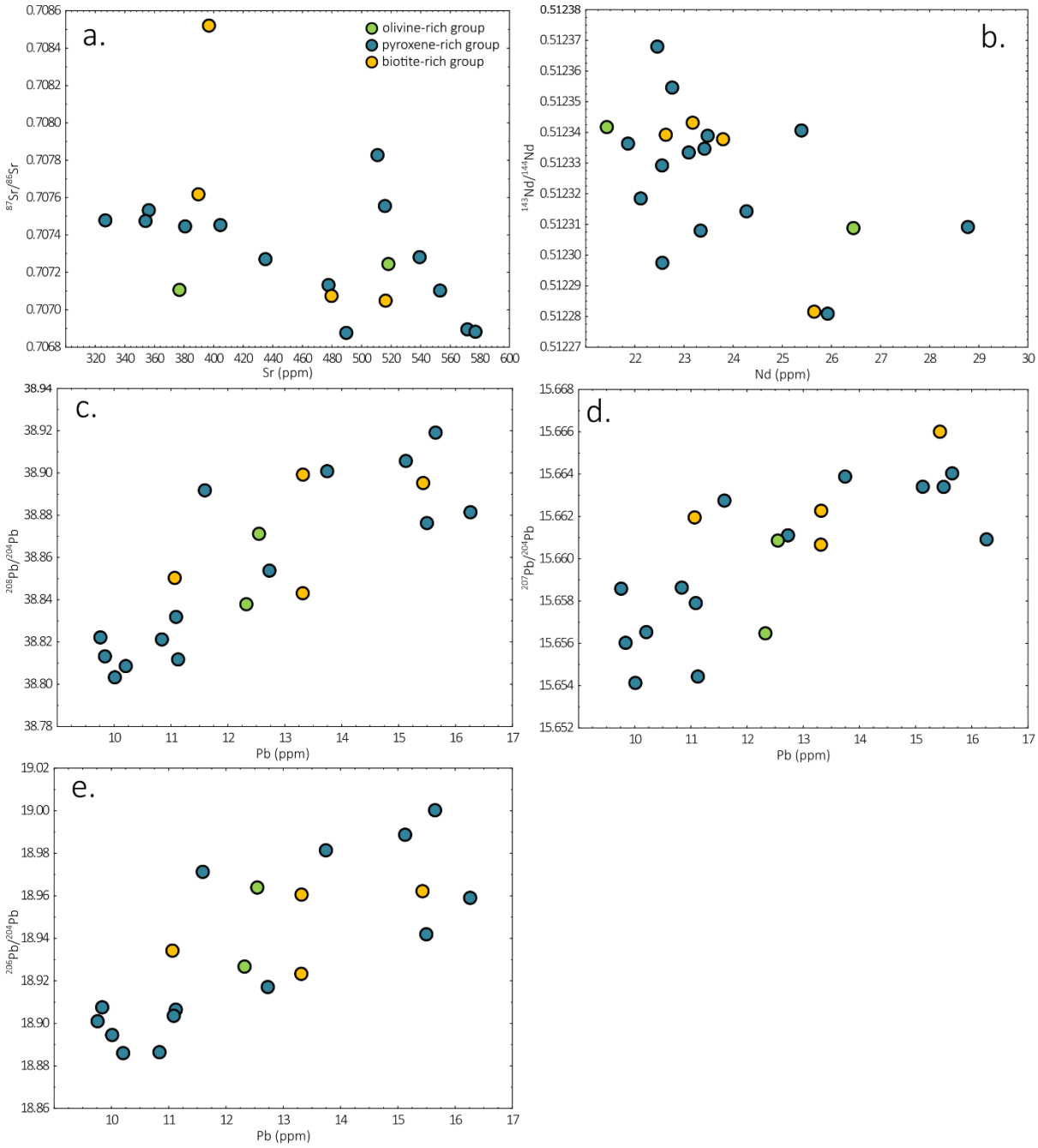

Figure 4.8. (a) $^{87}Sr/^{86}Sr$ vs Sr. (b) $^{143}Nd/^{144}Nd$ vs Nd. (c) $^{208}Pb/^{204}Pb$ vs Pb. (d) $^{207}Pb/^{204}Pb$ vs Pb. (e) $^{206}Pb/^{204}Pb$ vs Pb.

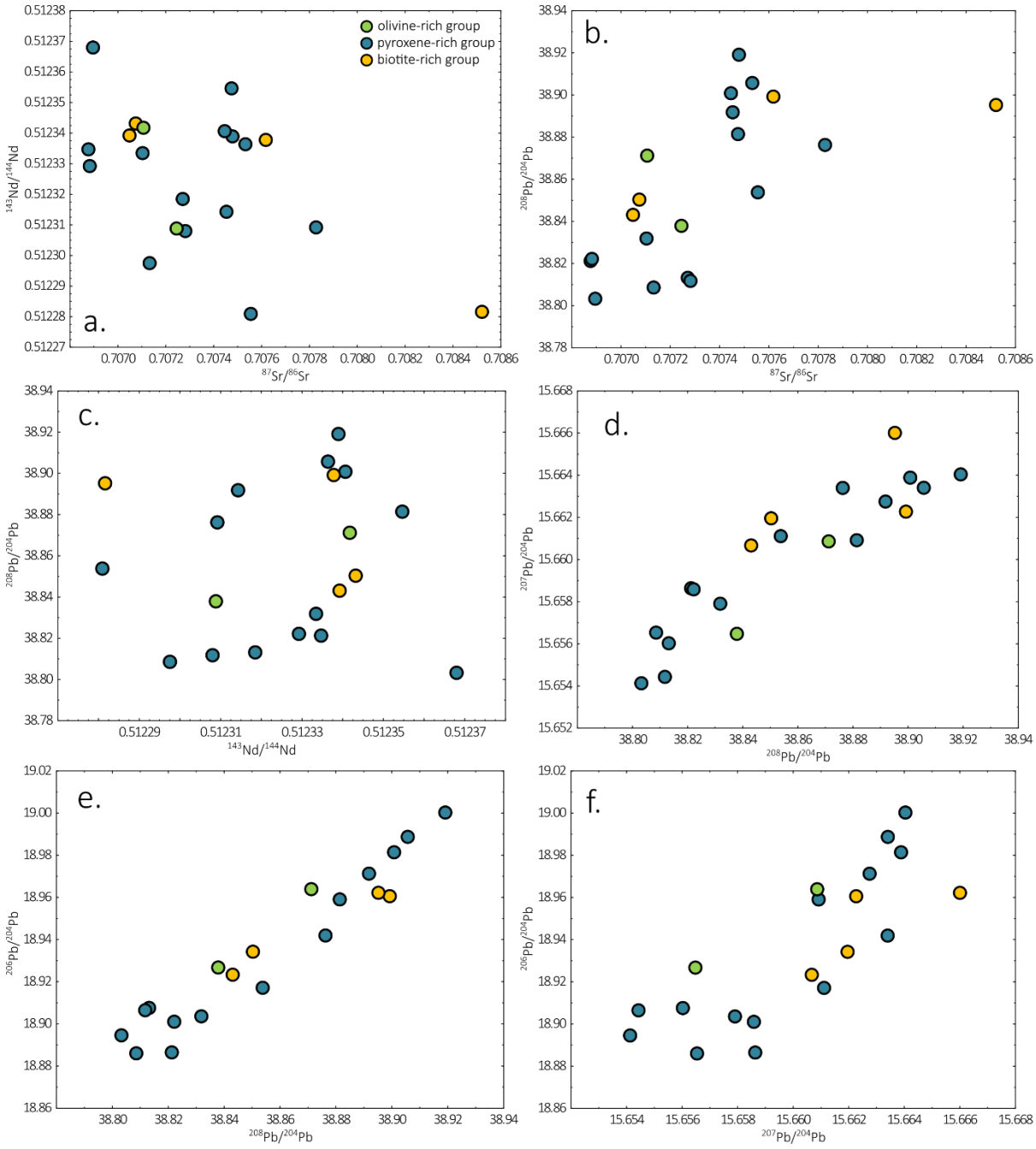

Figure 4.9. (a) $^{143}Nd/^{144}Nd$ vs $^{87}Sr/^{86}Sr$. (b) $^{208}Pb/^{204}Pb$ vs $^{87}Sr/^{86}Sr$. (c) $^{208}Pb/^{204}Pb$ vs $^{143}Nd/^{144}Nd$. (d) $^{207}Pb/^{204}Pb$ vs $^{208}Pb/^{204}Pb$. (e) $^{206}Pb/^{204}Pb$ vs $^{208}Pb/^{204}Pb$. (f) $^{206}Pb/^{204}Pb$ vs $^{207}Pb/^{204}Pb$.

Table 4.4. Radiogenic isotopes.

	olivine-rich group		*pyroxene-rich group*							
sample	VCA-21-015	VCA-21-048	VCA-21-002	VCA-21-003	VCA-21-004	VCA-21-009	VCA-21-012	VCA-21-016	VCA-21-019	VCA-21-026
$^{143}Nd/^{144}Nd$	0.512342	0.512309	0.512318	0.512298	0.512335	0.512314	0.512339	0.512341	0.512336	0.512355
$^{87}Sr/^{86}Sr$	0.707106	0.707245	0.707271	0.707133	0.706877	0.707453	0.707479	0.707446	0.707533	0.707475
$^{208}Pb/^{204}Pb$	38.8712	38.8379	38.8132	38.8086	38.8213	38.8918	38.9191	38.9008	38.9057	38.8814
$^{207}Pb/^{204}Pb$	15.6609	15.6565	15.6560	15.6565	15.6586	15.6627	15.6640	15.6639	15.6634	15.6609
$^{206}Pb/^{204}Pb$	18.9639	18.9268	18.9075	18.8861	18.8865	18.9713	19.0002	18.9814	18.9888	18.9591

Table 4.4. Radiogenic isotopes (continued).

	pyroxene-rich group						*biotite-rich group*			
sample	VCA-21-038	VCA-21-043	VCA-21-044	VCA-21-045	RMM-22-001	RMM-22-002	VCA-21-011	VCA-21-028	VCA-21-029	VCA-21-040
$^{143}Nd/^{144}Nd$	0.512309	0.512368	0.512329	0.512281	0.512308	0.512333	0.512338	0.512339	0.512343	0.512282
$^{87}Sr/^{86}Sr$	0.707828	0.706896	0.706882	0.707555	0.707282	0.707103	0.707618	0.707049	0.707074	0.708521
$^{208}Pb/^{204}Pb$	38.8763	38.8032	38.8222	38.8538	38.8117	38.8319	38.8993	38.8431	38.8503	38.8952
$^{207}Pb/^{204}Pb$	15.6634	15.6541	15.6586	15.6611	15.6544	15.6579	15.6623	15.6607	15.6620	15.6660
$^{206}Pb/^{204}Pb$	18.9419	18.8946	18.9010	18.9171	18.9065	18.9036	18.9606	18.9233	18.9342	18.9622

4.2.4. Oxygen isotopes:

For the olivine-rich group, the $\delta^{18}O_{pyroxene}$ values are 6.4 ‰ and 7.0 ‰ and the $\delta^{18}O_{plagioclase}$ values are 6.6 ‰ and 6.9 ‰ (table 4.5). For the pyroxene-rich group, the $\delta^{18}O_{pyroxene}$ values are 6.5 – 7.7 ‰ and the $\delta^{18}O_{plagioclase}$ value is 7.2 ‰ (table 4.5). $\delta^{18}O_{pyroxene}$ has a negative linear correlation with $^{143}Nd/^{144}Nd$ and weak negative linear correlations with SiO_2, $^{87}Sr/^{86}Sr$, $^{208}Pb/^{204}Pb$, $^{207}Pb/^{204}Pb$, and $^{206}Pb/^{204}Pb$ (fig. 4.10). For the biotite-rich group, the $\delta^{18}O_{pyroxene}$ values are 6.2 – 7.0 ‰ and the $\delta^{18}O_{plagioclase}$ values are 7.5 ‰ and 9.2 ‰ (table 4.5). $\delta^{18}O_{pyroxene}$ shows a strong negative linear correlation with $^{143}Nd/^{144}Nd$ and strong positive linear correlations with SiO_2, $^{87}Sr/^{86}Sr$, $^{208}Pb/^{204}Pb$, $^{207}Pb/^{204}Pb$, and $^{206}Pb/^{204}Pb$ (fig. 4.10).

Table 4.5. Oxygen isotope data.

sample	$\delta^{18}O_{pyroxene}$ (‰)	$\delta^{18}O_{plagioclase}$ (‰)
olivine-rich group		
VCA-21-015	6.4	6.6
VCA-21-048	7.0	6.9
pyroxene-rich group		
VCA-21-004	6.5	
VCA-21-012	6.7	7.2
VCA-21-044	7.7	
biotite-rich group		
VCA-21-029	6.2	7.5
VCA-21-040	6.6	9.2
	7.0	

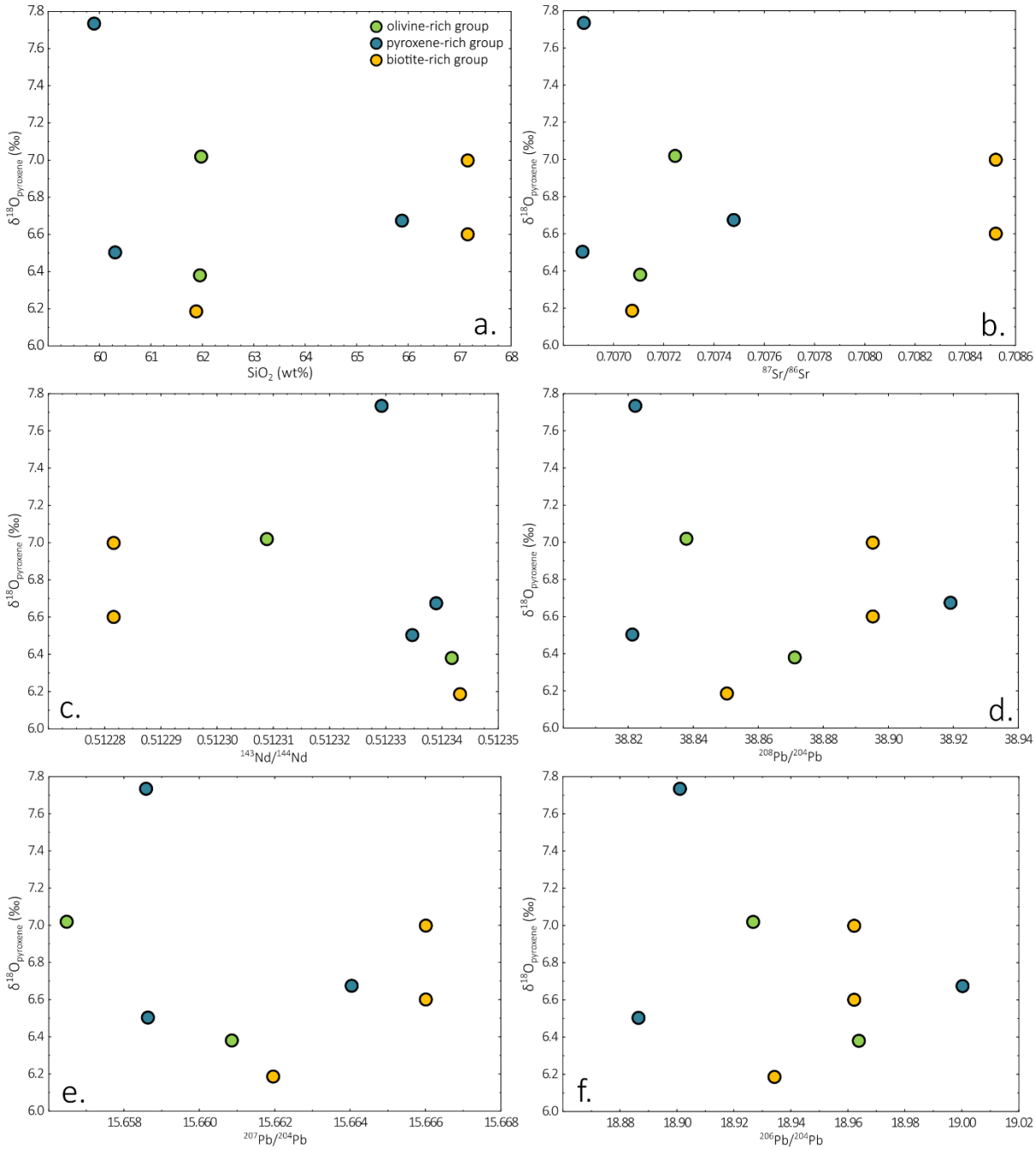

Figure 4.10. (a) $\delta^{18}O_{pyroxene}$ vs SiO_2. (b) $\delta^{18}O_{pyroxene}$ vs $^{87}Sr/^{86}Sr$. (c) $\delta^{18}O_{pyroxene}$ vs $^{143}Nd/^{144}Nd$. (d) $\delta^{18}O_{pyroxene}$ vs $^{208}Pb/^{204}Pb$. (e) $\delta^{18}O_{pyroxene}$ vs $^{207}Pb/^{204}Pb$. (f) $\delta^{18}O_{pyroxene}$ vs $^{206}Pb/^{204}Pb$.

5. Discussion:

5.1. General characteristics of Araral lavas:

The distinction between the olivine-, pyroxene-, and biotite-rich groups is based on petrography. There is little geochemical and isotopic distinction between the groups. The pyroxene-rich group significantly overlaps with the compositional ranges of both the olivine- and biotite-rich groups. The pyroxene-rich group has both the highest and lowest values for most of the geochemical components. However, the olivine-rich group has samples with the highest Ni and the lowest $\delta^{18}O_{plagioclase}$ values, and the biotite-rich group has samples with the highest SiO_2, CaO, $^{87}Sr/^{86}Sr$, $^{207}Pb/^{204}Pb$, and $\delta^{18}O_{plagioclase}$ values and lowest FeO*, MgO, CaO, Mg#, Ni, Cr, and $\delta^{18}O_{pyroxene}$ values. The compositional ranges for the olivine- and biotite-rich groups also overlap, except for SiO_2, MgO, FeO*, Mg#, Cr and $\delta^{18}O_{plagioclase}$. The samples of the olivine-rich group have lower values for SiO_2 and $\delta^{18}O_{plagioclase}$ and higher values for MgO, FeO, Mg#, and Cr. Additionally, both the samples of the olivine-rich group are andesites, while in the biotite-rich group, there are an equal number of andesites and dacites. With regards to SiO_2, MgO, FeO*, Mg#, Cr and $\delta^{18}O_{plagioclase}$, the olivine-rich samples are less evolved. Regardless, there are no clear boundaries between the olivine- and biotite-rich groups and there is significant overlap for all other geochemical components. The trends found in the pyroxene- and biotite-rich groups are generally in agreement with the trends of the collective sample set. Because of the geochemical and isotopic similarities between the olivine-, pyroxene-rich, and biotite-rich groups, they are not represented as separate groups in this section.

There are very subtle geochemical and isotope changes with relative eruptive age (fig 5.1). The relative eruptive age is inferred by elevation (table 3.1) – the younger rocks have higher elevations, and the older rocks have lower elevations.The relatively younger rocks show higher $\delta^{18}O_{pyroxene}$; whereas SiO_2, $^{143}Nd/^{144}Nd$, $^{208}Pb/^{204}Pb$, $^{207}Pb/^{204}Pb$, and $^{206}Pb/^{204}Pb$ are lower; and $^{87}Sr/^{86}Sr$ and $\delta^{18}O_{plagioclase}$ show no change with relative eruptive age. Additionally, samples containing biotite and hornblende are more prevalent in, but are not restricted to, the relatively older lavas. The most apparent correlation is the positive linear correlation between relative eruptive age and $\delta^{18}O_{pyroxene}$, this along with the negative linear correlations between relative eruptive age and $^{143}Nd/^{144}Nd$ suggests that relatively younger lavas are more evolved. However, the lack of change in $^{87}Sr/^{86}Sr$ and $\delta^{18}O_{plagioclase}$ with relative eruptive age

suggests that the relatively younger lavas are as evolved as the relatively older lavas. The weak negative linear correlation between relative eruptive age and SiO_2 suggests that the relatively younger lavas are less evolved. More mafic compositions for relatively younger rocks are consistent with the relationship between relative eruptive age and petrography. The relationships that relative eruptive age has with petrography and geochemistry in these samples provide a relatively unconstrained picture of the changes in Araral with time. The lack of absolute ages for the samples in this study makes it challenging to make a meaningful assessment of the geochemical changes of the lavas of Araral with time as done by Godoy et al. (2022) and Feeley and Davidson (1994) for Azufre and Ollagüe, respectively.

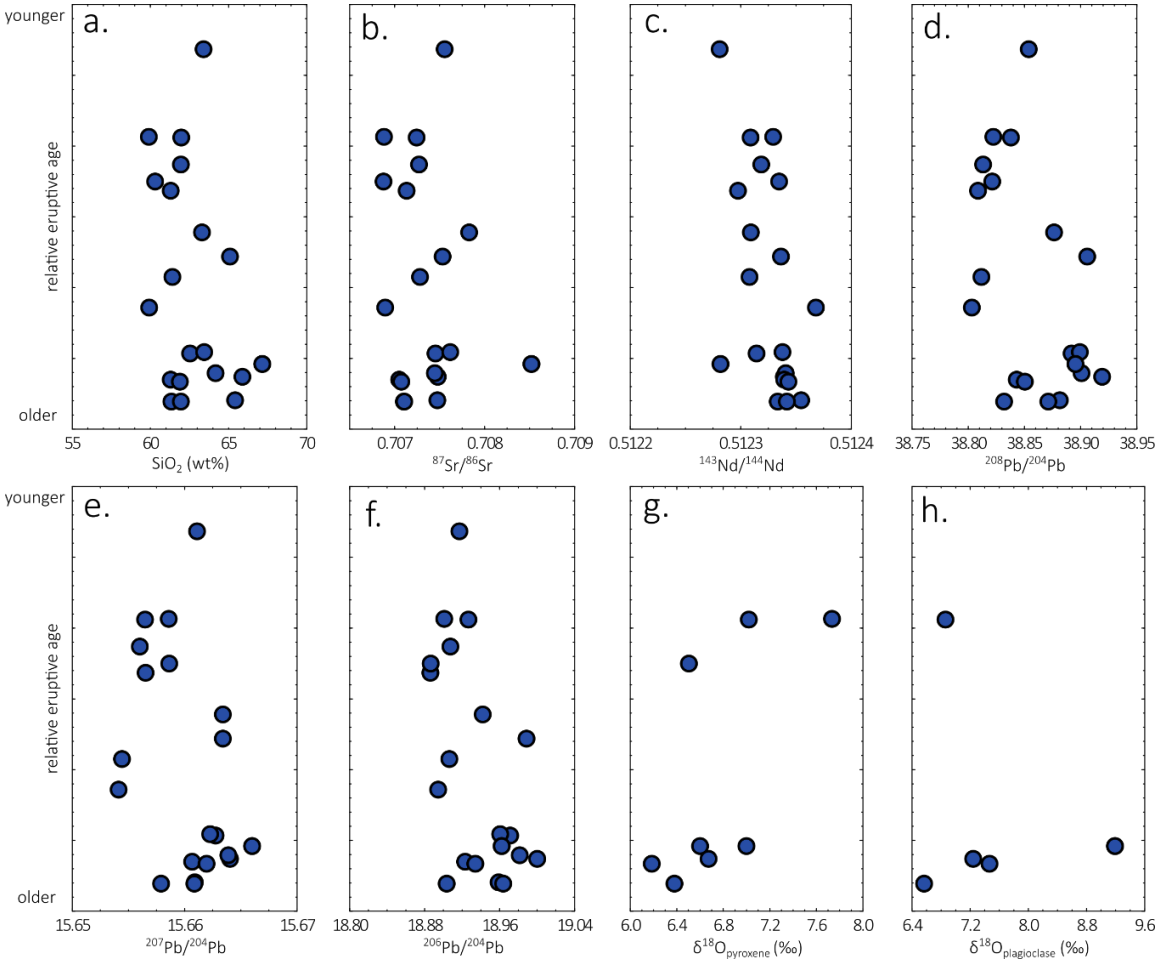

Figure 5.1. Relative eruptive age vs geochemical components. (a) Relative eruptive age vs SiO_2. (b) Relative eruptive age vs $^{87}Sr/^{86}Sr$. (c) Relative eruptive age vs $^{143}Nd/^{144}Nd$. (d) Relative eruptive age vs $^{208}Pb/^{204}Pb$. (e) Relative eruptive age vs $^{207}Pb/^{204}Pb$. (f) Relative eruptive age vs $^{206}Pb/^{204}Pb$. (g) Relative eruptive age vs $\delta^{18}O_{pyroxene}$. (h) Relative eruptive age vs $\delta^{18}O_{plagioclase}$.

The petrography and geochemical data of Araral from this study is generally in agreement with what is expected in the CVZ, Araral (based on data from previous studies), Pliocene and Quaternary lavas from the western margin of the APMB (fig. 5.2 – 11; e.g. González-Maurel et al., 2019a; Godoy et al., 2014, 2017; Lister, 2019; Mamani et al., 2010; Sellés and Gardeweg, 2017). The geochemical trends of Araral lavas are also similar to those of Pliocene and Quaternary lavas along the western margin of the APMB (e.g. González-Maurel et al., 2019a; Godoy et al., 2014, 2017; Lister, 2019). The samples also show little, but some, overlap with the data from Uturuncu (fig. 5.3a; fig. 5.4a – c and e; fig 5.5a; fig. 5.6a and d; fig. 5.7c; fig. 5.8c). Uturuncu is a Quaternary stratovolcano located at the centre of the present-day surface projection of the APMB, in southwest Bolivia (22°15'60" S, 67°10'60 "W; fig. 5.2). The lavas are high silica, predominantly dacitic with some andesites (Michelfelder et al. 2013). They are characterised by low $^{143}Nd/^{144}Nd$ (0.512148 – 0.512247), elevated $^{87}Sr/^{86}Sr$ (0.711002 – 0.714570) and $\delta^{18}O_{plagioclase}$ (7.3 – 9.6 ‰) relative to the lavas along the western margin (Godoy et al., 2014; Michelfelder et al., 2013). Information about the APVC lavas along the western margin of the APMB can be found in González-Maurel et al. (2019a) and Sellés and Gardeweg (2017).

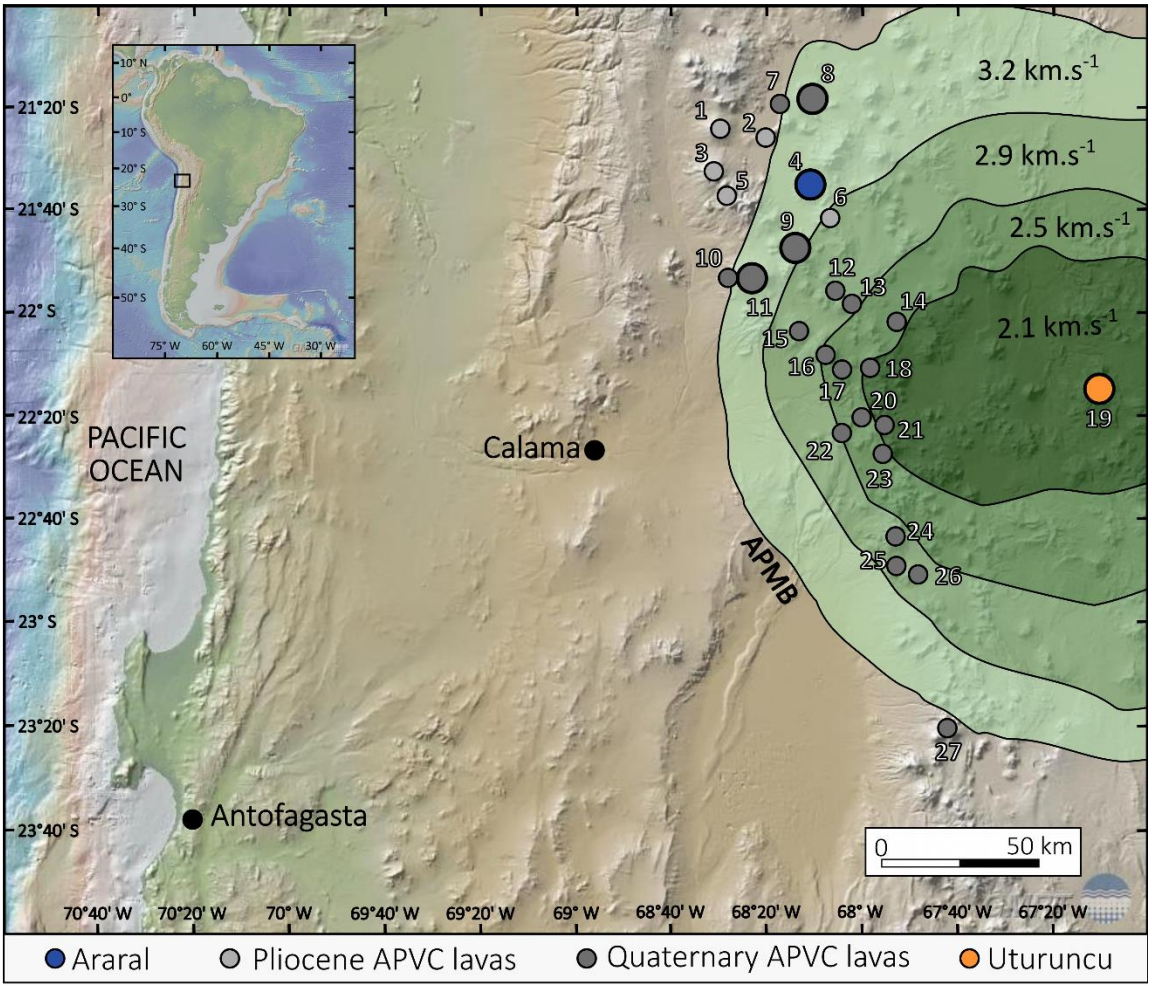

Figure 5.2. Global Multi-Resolution Topography (GMRT) image showing the surface projection of the present-day APMB and the locations of the Pliocene and Quaternary volcanoes in figures 5.3 – 5.11 and 5.15 (Bidart, 2014; de Astis et al., 2009; Feeley and Davidson, 1994; Feeley and Sharp, 1995; Figueroa and Figueroa, 2006; Figueroa et al., 2009; Godoy et al., 2014, 2017, 2018, 2019, 2022, 2023; González-Maurel et al., 2019a; Lister, 2019; Sellés and Gardeweg, 2017; Vezzoli et al., 2008; Watts et al., 1999). The green areas represent the extent of the APMB based on the joint ambient noise-receiver function inversion S-velocity model from Ward et al. (2014). The blue dot represents Araral. The grey dots represent Pliocene volcanoes. The dark grey dots represent Quaternary volcanoes. The orange dot represents Uturuncu. Pliocene volcanoes: 1 – Chela, 2 – Cerro Carcote, 3 – Palpana, **4 – Araral**, 5 – Cerro de las Cuevas, 6 – Ascotán. Quaternary volcanoes: 7 – La Poruñita, **8 – Ollagüe**, **9 – Cerro del Azufre**, 10 – La Poruña, **11 – San Pedro**, 12 – Apacheta, 13 – Cordón Inacaliri, 14 – Runtu Jarita, 15 – Paniri, 16 – Cerro de Leon, 17 – Toconce, 18 – Linzor, **19 – Uturuncu**, 20 – Volcán Tatio, 21 – Cerro La Quebrada, 22 – Cerro La Torta, 23 – Tocopuri, 24 – Sairecabur, 25 – Licancabur, 26 – Juriques, 27 – Lascar.

5.1.1. Petrography of Araral lavas:

The lavas of Araral from this study have glassy groundmass with microlites and hypocrystalline, porphyritic, and glomeroporphyritic textures (fig. 4.1). The phenocryst phases – in order of decreasing abundance and prevalence – are plagioclase, pyroxene, opaque mineral(s), biotite, amphibole, and olivine. Sieve textures in plagioclase and opacitic rims on pyroxene, hornblende, and biotite suggest chemical and thermal disequilibrium between the crystallising phases and the melt (fig. 4.1 c, d, e, h and i; Plechov et al. 2008; Nixon and Pearce, 1987). Sieve textures in plagioclase can form from the mixing of felsic and mafic magmas (Nixon and Pearce, 1987) and opacitic rims are formed from the addition of hotter magma into cooler magma (Plechov et al., 2008). Sample RMM-22-001 has spherulites (fig. 4.1 f and g), this is a texture common in rhyolites (Seaman et al., 2009, and references therein), but is not common to the lavas along the western margin of the APMB. Spherulites are radiating skeletal crystals formed from devitrification as a result of undercooling and are commonly made of felspar or intergrown feldspar and quartz (Seaman et al., 2009, and references therein). They suggest variable temperature conditions for the magma (Seaman et al., 2009, and references therein). The features of a lighter and a darker groundmass observed in some of the samples are reminiscent of flow banding (fig. 4.1 d and e) – the texture is common in felsic and intermediate lavas and often attributed to magma mixing (Seaman et al., 2009, and references therein). Observations that support the suggestion that this texture is flow banding are: (1) spherulites are commonly associated with flow banding (Seaman et al., 2009, and references therein); and (2) in some of the samples the crystals and microlites appear to be aligned with the “bands”. Microlites in groundmass are caused by undercooling and the “bands” with large amounts of microlites suggest a higher degree of undercooling (Seaman et al., 2009, and references therein). Undercooling can be induced by magma mixing (e.g. Nixon and Pearce, 1987). Additionally, some plagioclase crystals exhibit oscillatory zoning (fig 4.1a) which is associated with fluctuating conditions, such as plagioclase resorption in a convecting magma chamber containing both a primitive melt and an evolved melt, or the continuous replenishing and mixing of an evolved residual magma with a fresh primitive magma (Nixon and Pearce, 1987; Godoy et al., 2022, and references therein).

The petrography of the samples is consistent with that of previous studies of Araral and other volcanoes in the APVC (e.g., González-Maurel et al., 2019a; Lister, 2019; Michelfelder et al.,

2013; Sellés and Gardeweg, 2017). The samples have similar mineral assemblages – plagioclase and pyroxene with minor occurrences of olivine, biotite, amphibole, and opaque minerals. Like other lavas along the western margin of the APMB, the samples containing olivine and pyroxene generally have lower SiO_2 than most of the samples that just have pyroxene (González-Maurel et al., 2019a). Additionally, the samples in this study show similar disequilibrium textures – such as oscillatory zoning in plagioclase and opacitic rims on amphibole (e.g. Godoy et al., 2022). Oscillatory zoning has been attributed to the resorption of plagioclase caused by repeated magma replenishment of an evolved magma by more primitive magma (Godoy et al., 2022, and references therein). Flow banding is also common in mafic lavas in the APVC (Godoy et al., 2019, and references therein).

5.1.2. Whole-rock major and trace element compositions:

These Araral samples are high-K calc-alkaline andesites and dacites (fig. 5.3). SiO_2 shows a positive linear correlation with K_2O, no correlation with Na_2O and negative linear correlations with FeO*, MgO, CaO, TiO_2, and Al_2O_3 (fig. 5.3b and fig. 5.4). These linear relationships suggest that most of the major elements are affected by fractional crystallisation (e.g. Godoy et al., 2023). The major element data and geochemical trends are largely consistent with the Central Andean, Araral, Pliocene APVC, and Quaternary APVC arrays (fig. 5.3 and 5.4). Notably, RMM-22-001 from the pyroxene-rich group is the only medium-K calc-alkaline sample in the sample set, however, medium-K calc-alkaline samples can be found in the APVC (fig. 5.3b). The data overlaps with the APVC and Araral arrays for the plots of FeO*, and MgO, CaO, TiO_2, Al_2O_3, vs SiO_2 (fig. 5.4). For Na_2O vs SiO_2, the data overlaps with Quaternary APVC lavas and Araral samples from previous studies but not with Pliocene APVC lavas (fig. 5.4f). The Mg# values for the samples of Araral (42.15 – 52.90) are consistent with the Mg# values of Pliocene and Quaternary APVC lavas along the western margin of the APVC (43.93 – 63.70 and 25.35 – 66.77, respectively) and there is some overlap with the Mg# values for the lavas of Araral from previous studies (49.57 – 57.16) and the lavas of Uturuncu (39.10 – 44.72). Most of the APVC lavas along the western margin are high Mg# (50 – 60) and some classify as evolved (Mg# < 50) or primitive (Mg# > 60) (González-Maurel et al., 2019a, and references therein). Eleven of the Araral samples from this study are high Mg# and the rest (n = 9) are classified as evolved lavas (González-Maurel et al., 2019a, and references therein).

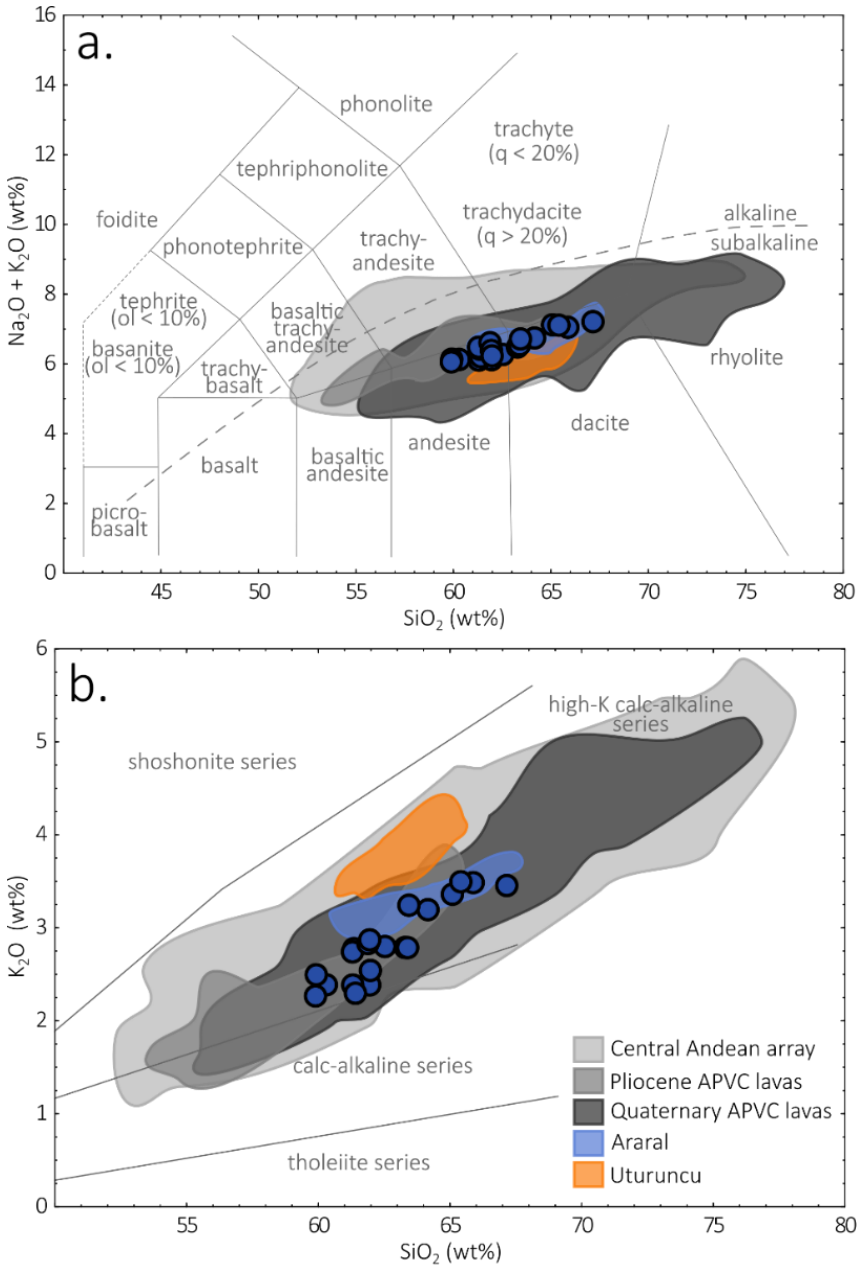

Figure 5.3. (a) Total alkali vs silica (TAS) diagram (Irvine and Bargar, 1971; Le Maitre et al., 1989). (b) K_2O vs SiO_2 classification diagram (Rickwood, 1989). The light grey area represents the Central Andean Array (Mamani et al., 2010). The grey area represents Pliocene APVC lavas along the western margin (González-Maurel et al., 2019a; Sellés and Gardeweg, 2017). The dark grey area represents Quaternary APVC lavas along the western margin (Bidart, 2014; de Astis et al., 2009; Feeley and Davidson, 1994; Figueroa and Figueroa, 2006; Figueroa et al., 2009; Godoy et al., 2014, 2017, 2018, 2019, 2022; González-Maurel et al., 2019a; Lister, 2019; Sellés and Gardeweg, 2017; Vezzoli et al., 2008; Watts et al., 1999). The blue area represents data for Araral from previous studies (González-Maurel et al., 2019a; Sellés and Gardeweg, 2017). The orange area represents Uturuncu (Michelfelder et al., 2013).

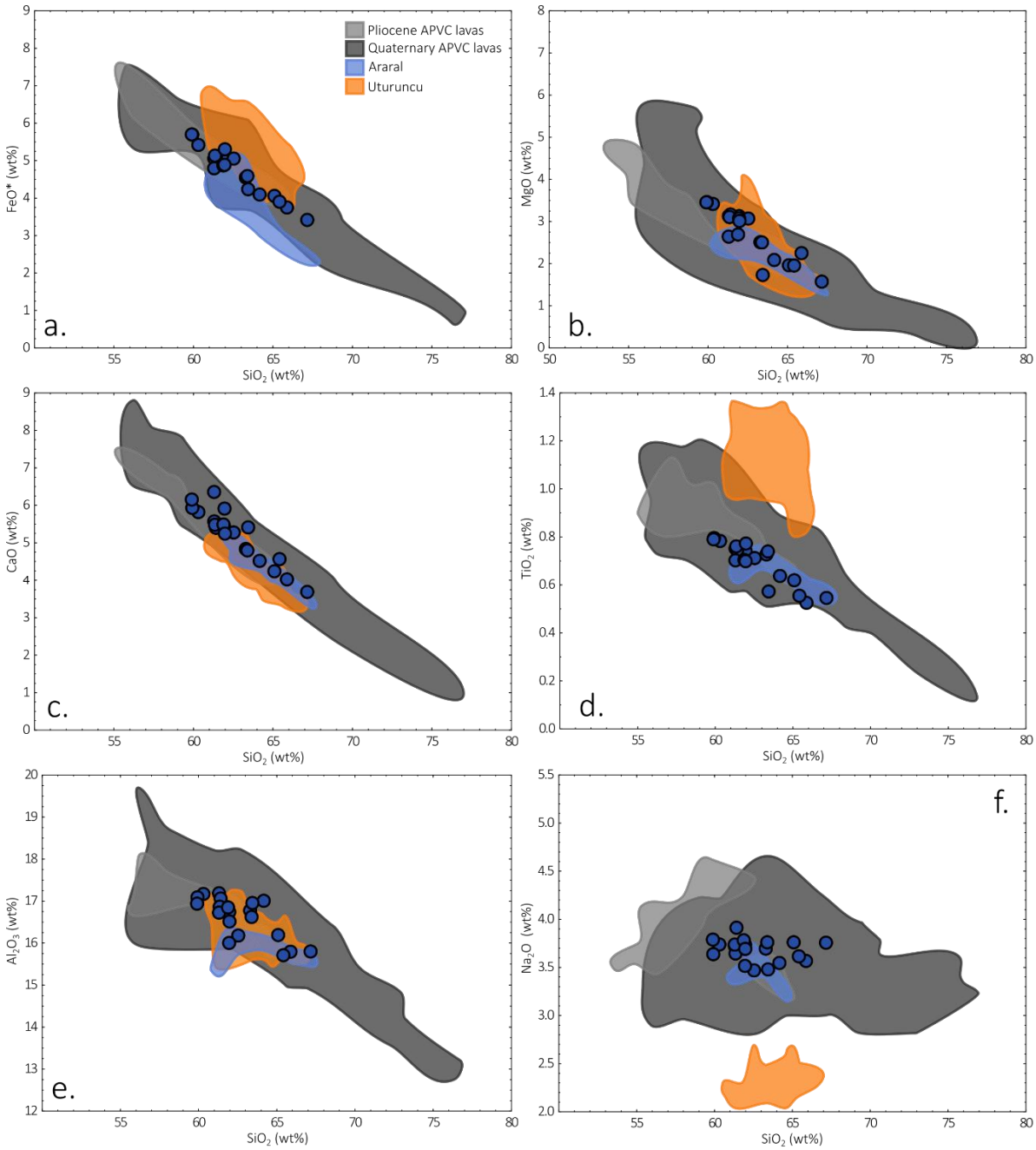

Figure 5.4. Major oxides vs SiO_2. (a) FeO* vs SiO_2. (b) MgO vs SiO_2. (c) CaO vs SiO_2. (d) TiO_2 vs SiO_2. (e) Al_2O_3 vs SiO_2. (f) Na_2O vs SiO_2. The grey area represents Pliocene APVC lavas along the western margin (González-Maurel et al., 2019a; Sellés and Gardeweg, 2017). The dark grey area represents Quaternary APVC lavas along the western margin (Bidart, 2014; de Astis et al., 2009; Figueroa and Figueroa, 2006; Figueroa et al., 2009; Feeley and Davidson, 1994; Godoy et al., 2014, 2017, 2018, 2019, 2022; González-Maurel et al., 2019a; Lister, 2019; Sellés and Gardeweg, 2017; Vezzoli et al., 2009; Watts et al., 1999). The blue area represents data for Araral from previous studies (González-Maurel et al., 2019a; Sellés and Gardeweg, 2017). The orange area represents Uturuncu (Michelfelder et al., 2013).

The trace elements patterns show that the samples are enriched in LILE, Rb, Th, U, Pb, and Sr with negative Na-Tb anomalies (fig. 5.5a). The REE patterns show an LREE enrichment with low LREE/HREE ratios and weak negative Eu anomalies (fig. 5.5b). The REE patterns are similar to the basaltic-andesite endmember which is proposed to be the parent magma for Central Andean lavas (Blum-Oeste and Wörner, 2016). Rare earth element patterns, Eu anomalies, and trace element ratios – namely Sr/Y, La/Yb, and Dy/Yb – can be used as indicators of the mineral present during magma evolution and consequently, the pressure conditions under which magmatic processes occurred (Mckay, 1989; Wörner et al., 2018). These geochemical components are affected by the presence of garnet, plagioclase, clinopyroxene, and amphibole (Wörner et al., 2018). The low LREE/HREE ratios (La/Yb = 10.46 – 20.49 and Dy/Yb = 1.16 – 1.57) suggest that magma differentiation occurred in an environment that is not compatible with garnet stability and fractionation (Burns et al., 2015; Davidson et al., 1990; Godoy et al., 2014; González-Maurel et al., 2019a; McKay, 1989; Taylor and McLennan, 1988). Garnet fractionates middle and heavy REE, resulting in steep REE patterns along with high La/Yb and Dy/Yb ratios (Mckay, 1989; Taylor and McLennan, 1988; Wörner et al., 2018). The depletion of HREE suggests an environment where garnet fractionation occurs and is unaffected by plagioclase fractionation (McKay, 1989; Taylor and McLennan, 1988). Garnet stability requires high pressures and consequently deep crustal levels – more than 12 kbar and 40 km depth (McKay, 1989; Taylor and McLennan, 1988). The absence of a garnet signature in the Araral lavas indicates that magma evolution predominantly occurred at shallow crustal levels. However, the lack of a garnet signature does not negate the possibility of magma ascension through and interaction with the thick crust (Godoy et al., 2014). Godoy et al. (2014) propose that low LREE/HREE ratios are caused by the rapid ascension of mantle-derived magmas that underwent minimal differentiation at deep crustal levels and most of the magma differentiation occurred at shallow crustal levels.

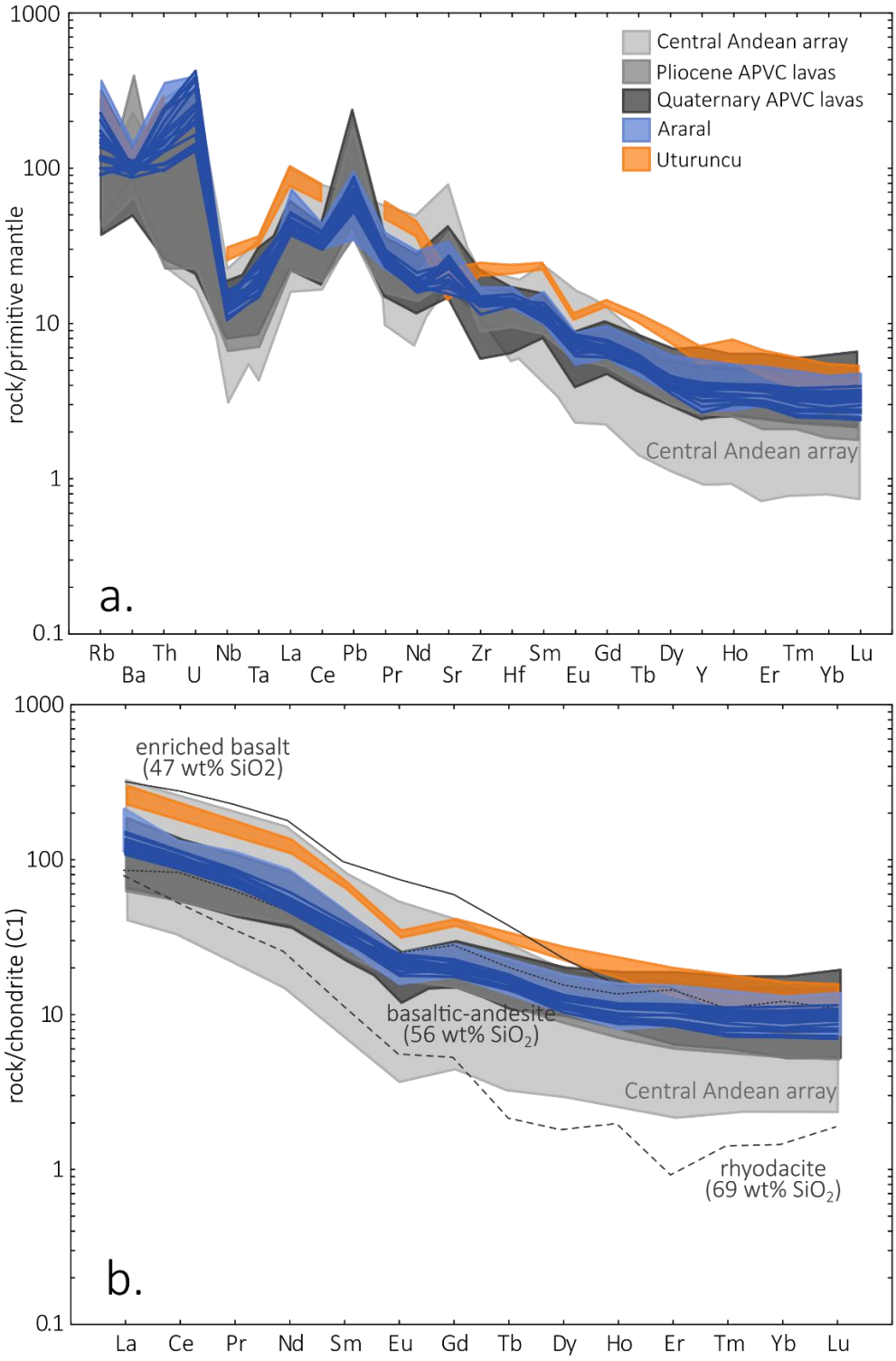

Figure 5.5. (a) Incompatible trace element diagram (trace element values normalised to primitive mantle values from Sun and McDonough, 1989). (b) Rare earth element diagram (REE values normalised to chondrite values from Sun and McDonough, 1989). The solid dark grey, dotted dark grey, and dashed dark grey lines represent the suggested enriched basalt, basaltic-andesite, and rhyodacite endmembers for Central Andean magmatism, respectively (Blum-Oeste and Wörner, 2016). The light grey area represents the Central Andean array

(Mamani et al., 2010). The grey area represents Pliocene APVC lavas along the western margin(González-Maurel et al., 2019a; Sellés and Gardeweg, 2017). The dark grey area represents Quaternary APVC lavas along the western margin (Figueroa and Figueroa, 2006; Figueroa et al., 2009; Godoy et al., 2014, 2017, 2018, 2019, 2022; González-Maurel et al., 2019a; Lister, 2019; Sellés and Gardeweg, 2017). The blue area represents data for Araral from previous studies (González-Maurel et al., 2019a; Sellés and Gardeweg, 2017). The orange area represents Uturuncu – the incompatible trace element pattern for Uturuncu is discontinuous because there is no data for U and Pb (Michelfelder et al., 2013).

The negative Eu/Eu* (0.76 – 0.92) and the negative linear correlation between Eu/Eu* and SiO_2 indicate plagioclase fractionation during magma differentiation (fig. 5.7a; McKay, 1989; Taylor and McLennan, 1988). Negative Eu anomalies are indicative of plagioclase-dominated environments because Eu preferably partitions into plagioclase (McKay, 1989; Taylor and McLennan, 1988). Plagioclase fractionation and stability occur at low-pressure conditions – less than 10 kbar or 40 km (Taylor and McLennan, 1988). This, in conjunction with the lack of garnet signature, alludes to magma differentiation taking place in the upper crust. The Sr/Y ratios (18.70 – 39.01) suggest magma differentiation at mid and shallow crustal levels, which are represented by Sr/Y > 30 and Sr/Y < 30, respectively (González-Maurel et al., 2019a). The low Sr/Y ratios are caused by plagioclase and clinopyroxene fractionation (Wörner et al., 2018). The samples have low La/Yb and Dy/Yb ratios with respect to the CVZ (fig. 5.7c – d; Mamani et al., 2010). Low La/Yb ratios support magma differentiation in an environment absent of garnet and amphibole (Davidson et al., 2013). The Dy/Yb ratios also suggest the absence of garnet but the presence of residual amphibole (González-Maurel et al., 2019a). This is consistent with amphibole as a minor phase observed in the samples of Araral and other lavas along the western margin of the APMB (Godoy et al., 2014; González-Maurel et al., 2019a). The shallow crustal signatures of the lavas in the APVC suggest that the APMB may have a role in the magmatic evolution in the lavas of Araral (Godoy et al., 2014).

For the Araral lavas, SiO_2 has negative linear correlations with Sr, Ni, Cr, Eu/Eu*, Sr/Y, and Dy/Yb; and positive linear correlations with Th and La/Yb (fig. 5.6 and 5.7). The negative linear correlations between SiO_2 and CaO, FeO, Cr, Ni and Eu/Eu* correspond with the fractional crystallisation of plagioclase and pyroxene with minor olivine, amphibole, and opaque

minerals (Godoy et al., 2022, González-Maurel et al., 2019a, McKay, 1989, Taylor and McLennan, 1988).

The trace element patterns of the Araral lavas are characteristic of those of subduction-related arc magmas and the CVZ (fig. 5.5a, Davidson et al., 1991) and are similar to those of the APVC. The REE patterns are consistent with those of APVC lavas and the CVZ but are not depleted in HREE like the rest of the CVZ (fig. 5.5b). The plots of Sr, Ni, and Cr vs SiO_2 show that the data for Araral overlaps with the APVC and Araral arrays (fig. 5.6). Some samples have higher Th values than expected, the samples are all dacites with higher SiO_2 contents and most of them contain biotite (fig. 5.6d). Those samples show overlap with the Uturuncu array and not the Pliocene and Quaternary APVC array. While the samples also have negative Eu anomalies, the anomalies are very weak, and the samples from this study have a higher Eu/Eu* for a given SiO_2 content in comparison to most lavas in the APVC (fig. 5.7a). The Araral samples have depleted Sr/Y ratios relative to the Central Andean array (fig. 5.7b). Most of the samples have consistent Sr/Y and SiO_2 values with the CVZ, previous Araral data and the APVC. The samples generally have lower La/Yb values than the Central Andean array and overlap with the data from the APVC and previous studies of Araral (fig. 5.7c). The Araral samples have lower Dy/Yb ratios than some Pliocene lavas but there is an overlap, there is more overlap with Quaternary lavas and Araral lavas from previous studies (fig. 5.7d).

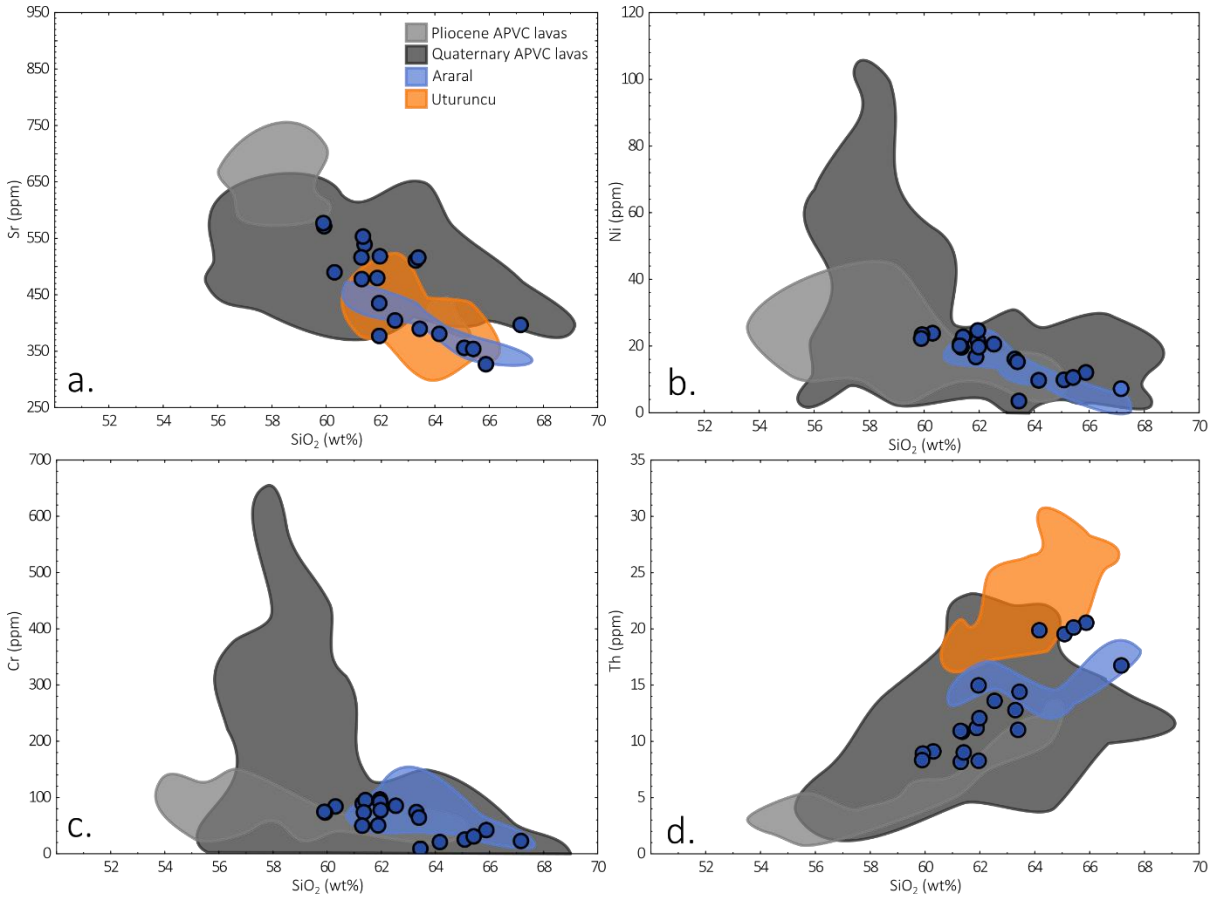

Figure 5.6. Trace elements vs SiO_2. (a) SiO_2 vs Sr. (b) SiO_2 vs Ni. (c) SiO_2 vs Cr. (d) SiO_2 vs Th. The grey area represents Pliocene APVC lavas along the western margin (González-Maurel et al., 2019a; Sellés and Gardeweg, 2017). The dark grey area represents Quaternary APVC lavas along the western margin (Bidart, 2014; de Astis et al., 2009; Figueroa and Figueroa, 2006; Figueroa et al., 2009; Feeley and Davidson, 1994; Godoy et al., 2014, 2017, 2018, 2019, 2022; González-Maurel et al., 2019a; Lister, 2019; Sellés and Gardeweg, 2017; Vezzoli et al., 2009; Watts et al., 1999). The blue area represents data for Araral from previous studies (González-Maurel et al., 2019a; Sellés and Gardeweg, 2017). The orange area represents Uturuncu (Michelfelder et al., 2013).

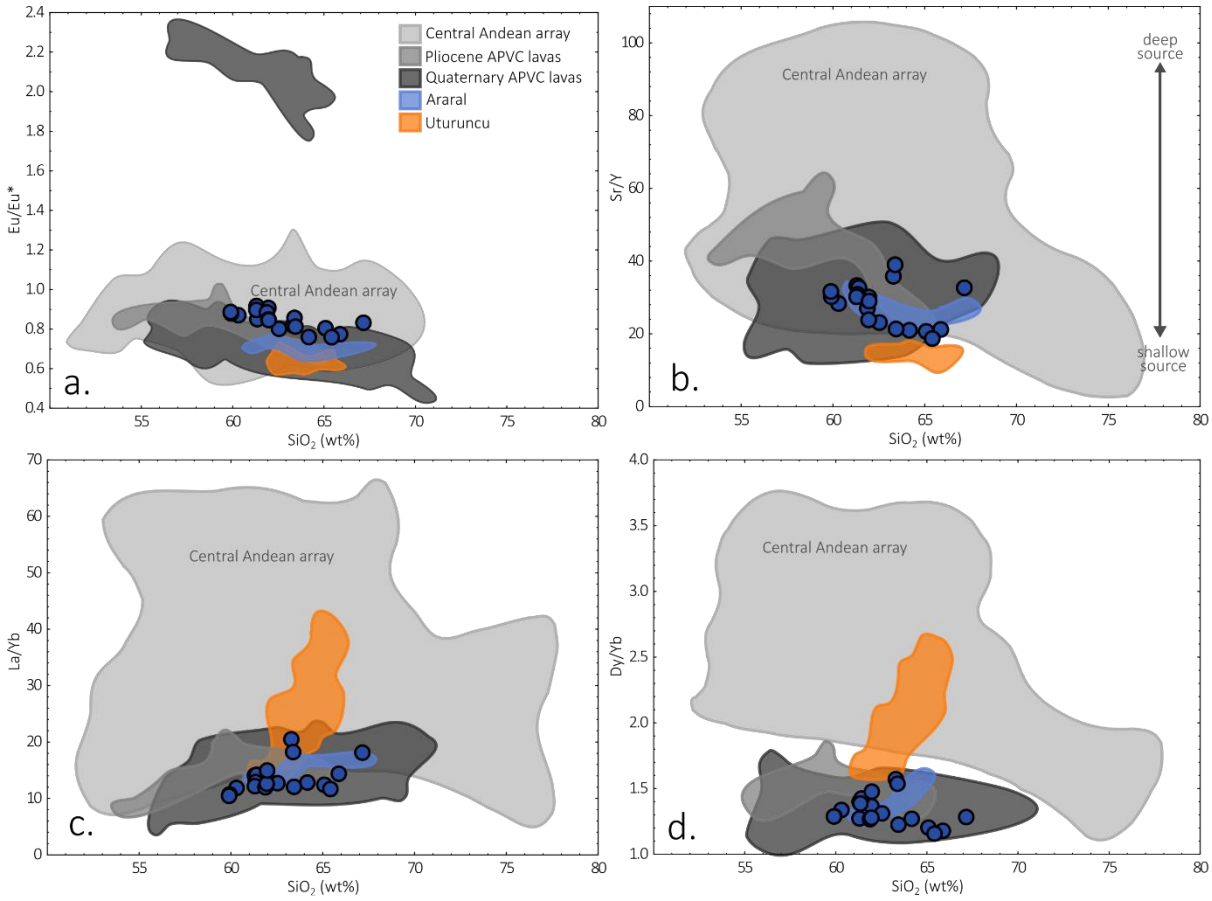

Figure 5.7. (a) SiO_2 vs Eu/Eu*. (b) SiO_2 vs Sr/Y. (c) SiO_2 vs La/Yb. (d) SiO_2 vs Dy/Yb. The light grey area represents the Central Andean Array (Mamani et al., 2010). The grey area represents Pliocene APVC lavas along the western margin (González-Maurel et al., 2019a; Sellés and Gardeweg, 2017). The dark grey area represents Quaternary APVC lavas along the western margin (Bidart, 2014; de Astis et al., 2009; Feeley and Davidson, 1994; Figueroa and Figueroa, 2006; Figueroa et al., 2009; Godoy et al., 2014, 2017, 2018, 2019; Vezzoli et al., 2009; González-Maurel et al., 2019a; Lister, 2019; Sellés and Gardeweg, 2017; Watts et al., 1999). The blue area represents data for Araral from previous studies (González-Maurel et al., 2019a; Sellés and Gardeweg, 2017). The orange area represents Uturuncu (Michelfelder et al., 2013).

5.1.3. Whole-rock radiogenic isotope compositions:

$^{87}Sr/^{86}Sr$ has negative linear correlations with Sr (fig. 5.9a) and $^{143}Nd/^{144}Nd$ (fig. 5.10a); and positive linear correlations with SiO_2 (fig. 5.8a), $^{208}Pb/^{204}Pb$ (fig. 5.10b), $^{207}Pb/^{204}Pb$ (not plotted), and $^{206}Pb/^{204}Pb$ (not plotted). $^{143}Nd/^{144}Nd$ shows a negative linear correlation with Nd (fig. 5.9b); and no linear correlation with SiO_2 (fig. 5.8b), $^{208}Pb/^{204}Pb$ (fig. 5.10c), $^{207}Pb/^{204}Pb$ (not plotted), and $^{206}Pb/^{204}Pb$ (not plotted). Lead isotope ratios have positive linear correlations with SiO_2, Pb and one another (fig. 5.8 c –e; fig. 5.9 c – e; fig. 5.10 d – f). Radiogenic isotopes can be used as indicators of magma contamination by crustal assimilation and APMB contribution (e.g. Godoy et al., 2017, 2023; Wörner et al., 2018). The radiogenic isotope ratios of the mantle-derived and crustal lavas are distinct (Wörner et al., 2018). The radiogenic isotope values for the mantle and mantle-derived lavas are relatively homogeneous with low $^{87}Sr/^{86}Sr$ (0.703) and high $^{143}Nd/^{144}Nd$ (> 0.5129) (Davidson et al., 1991; Eiler, 2001; Harmon et al., 1981; Wörner et al., 2018). While those of the crustal rocks are variable with relatively high $^{87}Sr/^{86}Sr$ and low $^{143}Nd/^{144}Nd$ (Wörner et al., 2018). Radiogenic isotopes are unaffected by melting and fractional crystallisation and can therefore be used as an indicator for the compositions and proportions of the magma sources (Wörner et al., 2018). Additionally, Pb isotope ratios will reflect those of the underlying crust even with minimal crustal contamination (Wörner et al., 2018).

The lavas of Araral have high $^{87}Sr/^{86}Sr$ (0.706877 – 0.708521) and low $^{143}Nd/^{144}Nd$ (0.512281 – 0.512368) ratios relative to the primitive mantle (Davidson et al., 1990), suggesting crustal contamination of these magmas during ascension (Davidson et al., 1991, Mamani et al. 2010). Araral like other lavas along the western margin of the APMB have higher $^{87}Sr/^{86}Sr$ and $^{143}Nd/^{144}Nd$ ratios than most Central Andean lavas, indicating a higher degree of crustal contamination. However, Araral has lower $^{87}Sr/^{86}Sr$ and higher $^{143}Nd/^{144}Nd$ than Uturuncu and APVC ignimbrites (fig. 5.10a; Godoy et al., 2017). Like other lavas along the western margin, even the samples from Araral with high SiO_2 have lower Sr isotope values than the lavas of Uturuncu (fig. 5.8a; Godoy et al., 2017). The lower $^{87}Sr/^{86}Sr$ and higher $^{143}Nd/^{144}Nd$ values relative to Uturuncu are interpreted to be caused by a lower degree of interaction with the APMB (Godoy et al., 2017; González-Maurel et al., 2019a).

Plots of radiogenic isotopes vs SiO_2 show that the data agree with the APVC and previous, limited Araral arrays for $^{87}Sr/^{86}Sr$ and $^{143}Nd/^{144}Nd$ (fig. 5.8a and b). There is little overlap in plots of Pb isotopes and SiO_2, for $^{208}Pb/^{204}Pb$ there is overlap with quaternary APVC lavas and Uturuncu, for $^{207}Pb/^{204}Pb$ there is overlap with quaternary APVC lavas, and for $^{206}Pb/^{204}Pb$ there is no overlap with either – the lavas of Araral have higher $^{206}Pb/^{204}Pb$ ratios (fig. 5.8c – e). For $^{87}Sr/^{86}Sr$ vs elemental Sr and $^{143}Nd/^{144}Nd$ vs elemental Nd, the new Araral data overlaps with APVC lavas and data from Araral from previous research (fig. 5.9). For the plot of $^{143}Nd/^{144}Nd$ vs $^{87}Sr/^{86}Sr$, the Araral data overlaps with the Central Andean, previous Araral, Pliocene and Quaternary APVC arrays (fig. 5.10a). Regarding the plots of $^{208}Pb/^{204}Pb$ vs $^{87}Sr/^{86}Sr$ (fig. 5.10b), $^{207}Pb/^{204}Pb$ vs $^{87}Sr/^{86}Sr$ (not plotted), $^{208}Pb/^{204}Pb$ vs $^{143}Nd/^{144}Nd$ (fig. 5.10c), $^{207}Pb/^{204}Pb$ vs $^{143}Nd/^{144}Nd$ (not plotted), and $^{207}Pb/^{204}Pb$ vs $^{208}Pb/^{204}Pb$ (fig. 5.10d) there is little overlap with Quaternary APVC lavas. There is no overlap with data from previous research in plots of $^{208}Pb/^{204}Pb$ vs Pb (fig. 5.9c), $^{207}Pb/^{204}Pb$ vs Pb (fig. 5.9d), $^{206}Pb/^{204}Pb$ vs Pb (fig. 5.9e), $^{206}Pb/^{204}Pb$ vs $^{87}Sr/^{86}Sr$ (not plotted), $^{206}Pb/^{204}Pb$ vs $^{143}Nd/^{144}Nd$ (not plotted), $^{206}Pb/^{204}Pb$ vs $^{208}Pb/^{204}Pb$ (fig. 5.10e), and $^{206}Pb/^{204}Pb$ vs $^{207}Pb/^{204}Pb$ (fig. 5.10f). For the plots of Pb isotopes vs elemental Pb, the Quaternary APVC array comprised only samples from Ollagüe (Feeley and Davidson, 1994) because only those samples had both Pb isotopes ratios and elemental Pb concentrations available. The lack of overlap with the plots of $^{208}Pb/^{204}Pb$ vs Pb and $^{207}Pb/^{204}Pb$ vs Pb is caused by $^{208}Pb/^{204}Pb$ and $^{207}Pb/^{204}Pb$ values of Araral lavas having no overlap with those of Ollagüe, even though the values overlap with those of other APVC lavas.

The linear correlations $^{87}Sr/^{86}Sr$ has with SiO_2, Sr, and $^{143}Nd/^{144}Nd$ are consistent with what is observed for other volcanoes (González-Maurel et al., 2019a). Little or no linear correlation between SiO_2 and $^{143}Nd/^{144}Nd$ can be observed at other volcanoes in the APVC (e.g. Lister, 2019). The linear correlations with Pb isotopes and other geochemical components are consistent with what is observed in some Quaternary APVC lavas (Godoy et al., 2014; Michelfelder et al., 2013).

The Pb isotope ratios of Araral lavas are on the higher end of the expected range for APVC lavas and there is no overlap with the values for $^{206}Pb/^{204}Pb$ (Godoy et al., 2014; Feeley and Davidson, 1994; Figueroa and Figueroa, 2006; Michelfelder et al., 2013). The elevated Pb isotope ratios of the Araral lavas could be a result of the age, Araral is Pliocene in age while

the other APVC lavas are quaternary (Komárek et al., 2007, and references therein). Alternatively, the difference could be caused by U, Th, and Pb concentrations – ^{208}Pb, ^{207}Pb, and ^{206}Pb are formed from the decay of ^{232}Th, ^{235}U, and ^{238}U (Komárek et al., 2007, and references therein). The U/Pb (0.27 – 0.55) and Th/Pb (0.80 – 1.45) ratios of Araral lavas are high relative to those of Ollagüe (U/Pb = 0.09 – 0.38 and Th/Pb = 0.30 – 0.76), the samples of Ollagüe are the only ones that had U, Th, and Pb concentrations available. The relative U and Th enrichment in the Araral lavas could be the cause of the elevated Pb isotope ratios. The concentration of these elements affects ^{206}Pb (and consequently ^{206}Pb /^{204}Pb) most because ^{238}U is relatively abundant (Komárek et al., 2007, and references therein). This could be the cause of the lack of overlap between the $^{206}Pb/^{204}Pb$ values of Araral lavas and other APVC lavas. Further, there is not much Pb isotope data for APVC lavas, which could also account for the discrepancy considering that the Pb isotope ratios of Araral lavas are consistent with those of the Antofalla domain (Mamani et al., 2008, 2010).

The consistency between the Pb ratios of Araral and the underlying basement suggests the incorporation of the underlying basement into the magma that formed the Araral lavas (Wörner et al., 2018). Because the Pb isotope ratios have no regional variations and the ratios are not significantly altered by differentiation, the changes in $^{87}Sr/^{86}Sr$ are considered to be caused by varying degrees of contamination and differentiation rather than changes in crustal compositions (Godoy et al., 2014). While the samples of Araral have values expected of this area, Pb isotopes increase linearly with both SiO_2 and $^{87}Sr/^{86}Sr$, indicating that these values are affected by magma differentiation processes to some extent.

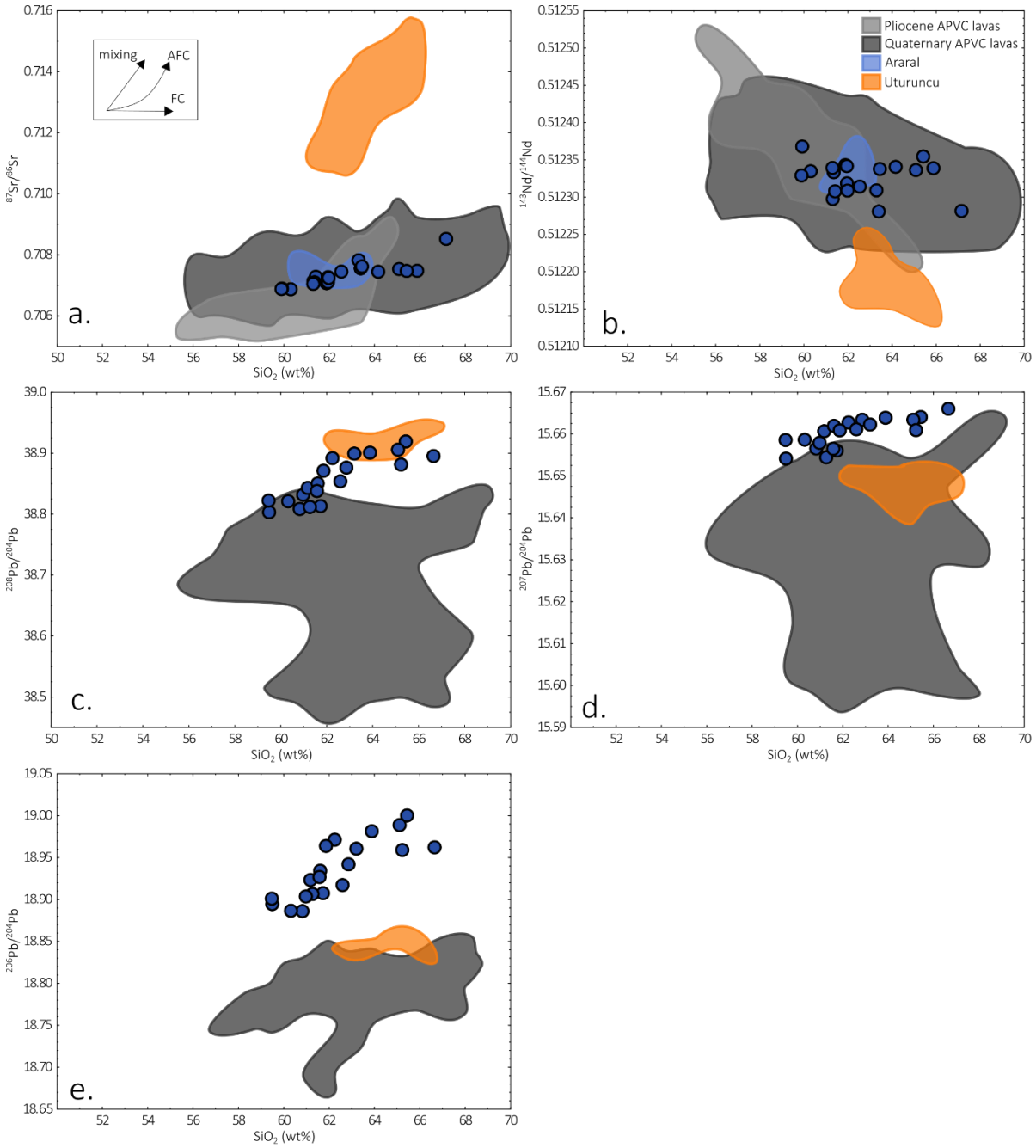

Figure 5.8. Radiogenic isotope ratios vs SiO_2. (a) $^{87}Sr/^{86}Sr$ vs SiO_2. The inset shows the typical trends for mixing, AFC, and fractional crystallisation (FC) processes. (b) $^{143}Nd/^{144}Nd$ vs SiO_2. (c) $^{208}Pb/^{204}Pb$ vs SiO_2. (d) $^{207}Pb/^{204}Pb$ vs SiO_2. (e) $^{206}Pb/^{204}Pb$ vs SiO_2. The grey area represents Pliocene APVC lavas along the western margin (González-Maurel et al., 2019a). The dark grey area represents Quaternary APVC lavas along the western margin (Feeley and Davidson, 1994; Figueroa and Figueroa, 2006; Figueroa et al., 2009; Godoy et al., 2014, 2017, 2018, 2019, 2023; González-Maurel et al., 2019a; Lister, 2019). The blue area represents data for Araral from previous studies (González-Maurel et al., 2019a). The orange area represents Uturuncu (Michelfelder et al., 2013).

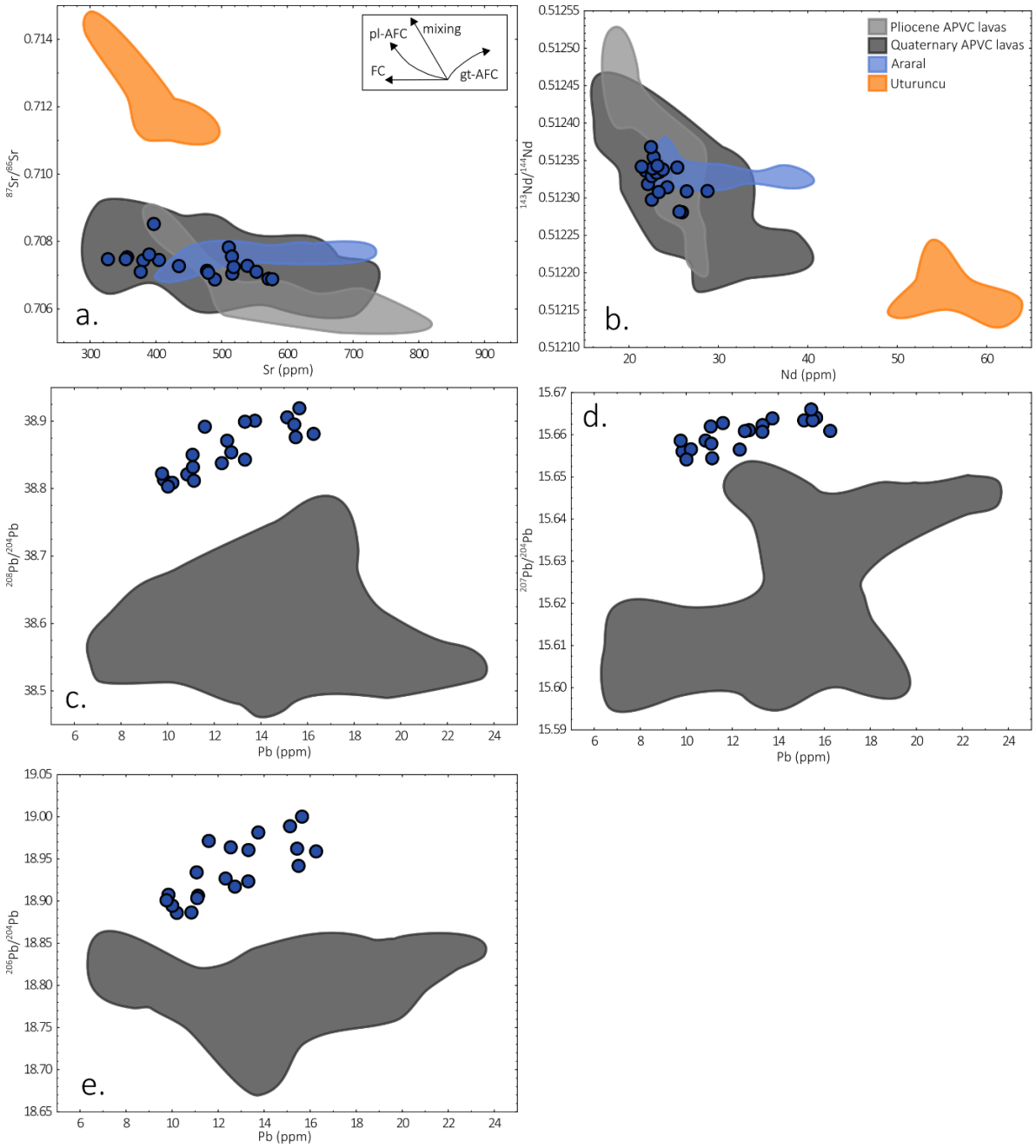

Figure 5.9. (a) $^{87}Sr/^{86}Sr$ vs Sr. The inset shows the typical trends for mixing, fractional crystallisation (FC), plagioclase- and garnet-dominated AFC (pl-AFC and gt-AFC, respectively) processes. (b) $^{143}Nd/^{144}Nd$ vs Nd. (c) $^{208}Pb/^{204}Pb$ vs Pb. (d) $^{207}Pb/^{204}Pb$ vs Pb. (e) $^{206}Pb/^{204}Pb$ vs Pb. The grey area represents Pliocene APVC lavas along the western margin (González-Maurel et al., 2019a). The dark grey area represents Quaternary APVC lavas along the western margin (Feeley and Davidson, 1994; Figueroa and Figueroa, 2006; Figueroa et al., 2009; Godoy et al., 2014, 2017, 2018, 2019, 2023; González-Maurel et al., 2019a; Lister, 2019). The blue area represents data for Araral from previous studies (González-Maurel et al., 2019a). The orange area represents Uturuncu (Michelfelder et al., 2013).

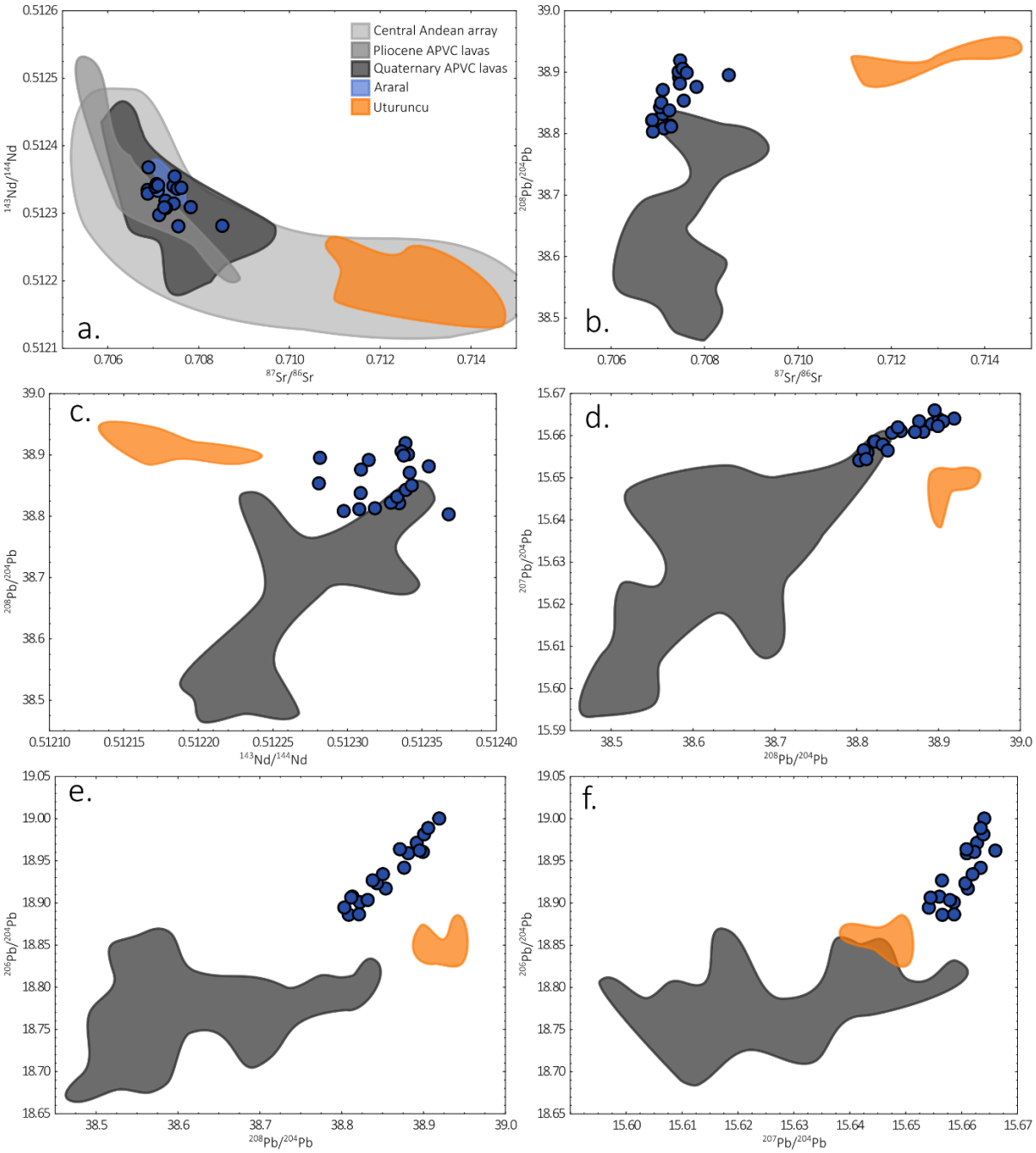

Figure 5.10. (a) $^{143}Nd/^{144}Nd$ vs $^{87}Sr/^{86}Sr$. (b) $^{208}Pb/^{204}Pb$ vs $^{87}Sr/^{86}Sr$. (c) $^{208}Pb/^{204}Pb$ vs $^{143}Nd/^{144}Nd$. (d) $^{207}Pb/^{204}Pb$ vs $^{208}Pb/^{204}Pb$. (e) $^{206}Pb/^{204}Pb$ vs $^{208}Pb/^{204}Pb$. (f) $^{206}Pb/^{204}Pb$ vs $^{207}Pb/^{204}Pb$. The light grey area represents the Central Andean array (Godoy et al., 2017). The grey area represents Pliocene APVC lavas along the western margin (González-Maurel et al., 2019a). The dark grey area represents Quaternary APVC lavas along the western margin (Feeley and Davidson, 1994; Figueroa and Figueroa, 2006; Figueroa et al., 2009; Godoy et al., 2014, 2017, 2018, 2019, 2023; González-Maurel et al., 2019a; Lister, 2019). The blue area represents data for Araral from previous studies (González-Maurel et al., 2019a). The orange area represents Uturuncu (Michelfelder et al., 2013).

5.1.4. Oxygen isotope compositions:

$\delta^{18}O_{pyroxene}$ has no linear correlations with SiO_2 (fig 5.11a) and $^{87}Sr/^{86}Sr$ (fig. 5.11b) and a weak negative linear correlation with $^{143}Nd/^{144}Nd$ (fig. 5.11c). $\delta^{18}O_{plagioclase}$ has no linear correlations with $^{87}Sr/^{86}Sr$ (fig 5.11e) and $\delta^{18}O_{pyroxene}$ (fig 5.11f), weak positive linear correlations with SiO_2 (fig 5.11d) and $^{143}Nd/^{144}Nd$ (not shown). The weak and lack of linear correlations between O isotopes and other geochemical components suggest that variations in O isotopes are not a result of fractional crystallisation (e.g. Godoy et al., 2023). Further, the elevated Sr and O isotope ratios suggest crustal assimilation because contamination of subducted material before melting by mantle source would have little effect on O isotope ratios (Wörner et al., 2018).

The plots of O isotope data show some overlap with previous data from CVZ. Except for $\delta^{18}O_{pyroxene}$ vs $^{143}Nd/^{144}Nd$. Like other individual volcanoes, the O isotope data for Araral shows no linear correlation or very weak linear correlation with other chemical components (Godoy et al., 2023). The $\delta^{18}O$ data from previous studies show positive linear correlations between $\delta^{18}O_{pyroxene}$ and $\delta^{18}O_{plagioclase}$, whereas the $\delta^{18}O$ data from this study shows no linear correlation between the two.

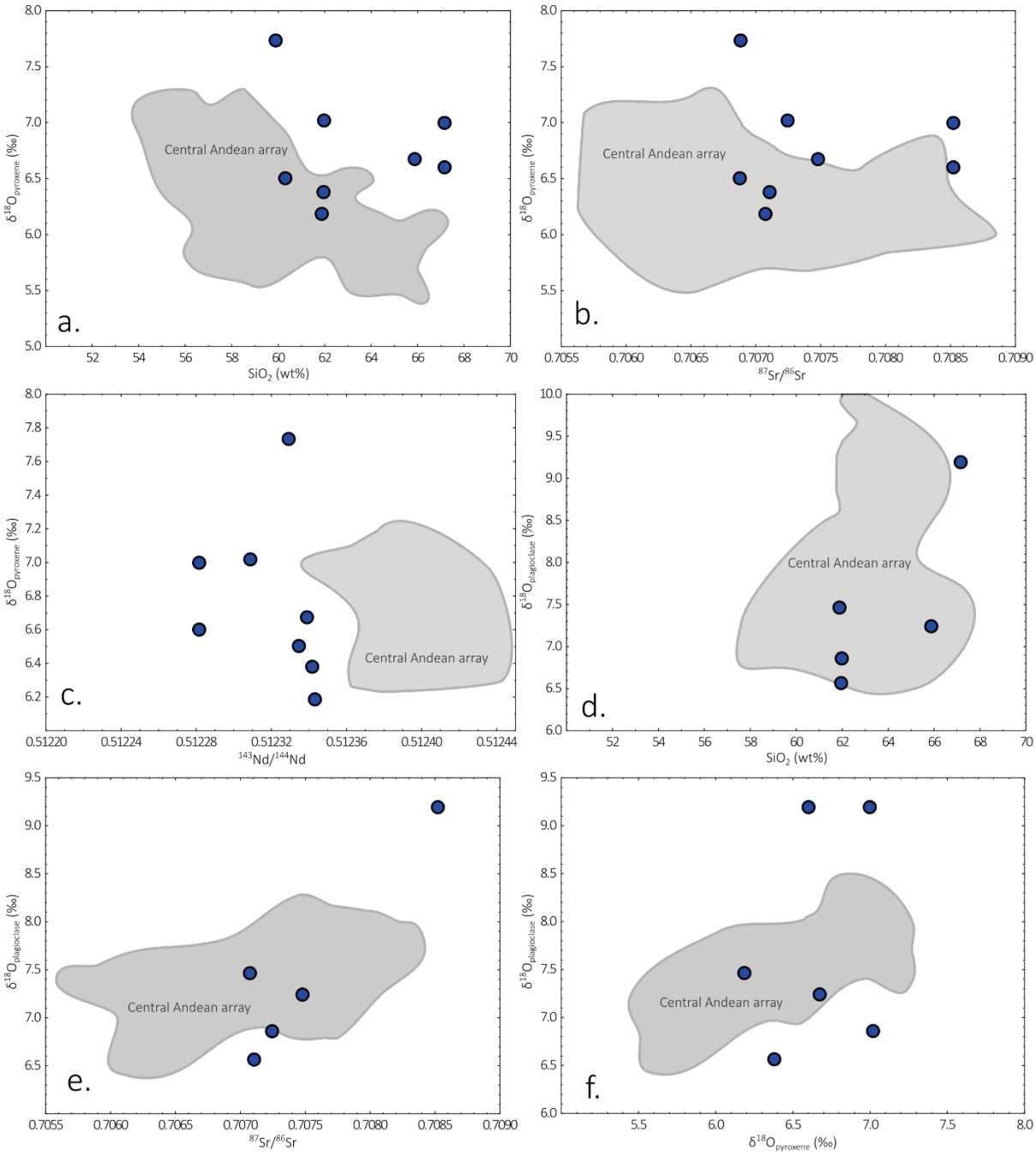

Figure 5.11. (a) $\delta^{18}O_{pyroxene}$ vs SiO_2. (b) $\delta^{18}O_{pyroxene}$ vs $^{87}Sr/^{86}Sr$. (c) $\delta^{18}O_{pyroxene}$ vs $^{143}Nd/^{144}Nd$. (d) $\delta^{18}O_{plagioclase}$ vs SiO_2. (e) $\delta^{18}O_{plagioclase}$ vs $^{87}Sr/^{86}Sr$. (f) $\delta^{18}O_{plagioclase}$ vs $\delta^{18}O_{pyroxene}$. The light grey area represents the Central Andean Array (Feeley and Sharp, 1995; Freymuth et al., 2015, and references therein; González-Maurel et al., 2020; Michelfelder et al., 2013).

5.2. Crustal assimilation at Araral:

The AFC model presented by Godoy et al. (2017) shown in Figure 5.12 uses a sample from Lascar as a primitive end-member and samples from Sierra de Moreno as as the crustal contaminant. The sample from Lascar is characterised by SiO_2 = 57.55 wt%; MgO = 3.78 wt%; Sr = 711 ppm; $^{87}Sr/^{86}Sr$ = 0.70577; and $^{143}Nd/^{144}Nd$ = 0.51247 (Godoy et al., 2017, and references therein). The samples from Sierra de Moreno are characterised by SiO_2 = 65.28 and 68.80 wt%; MgO = 1.94 and 2.14 wt%; Sr = 185 and 271 ppm; $^{87}Sr/^{86}Sr$ = 0.72184 and 0.72777; and $^{143}Nd/^{144}Nd$ = 0.51196 and 0.51209 (Godoy et al., 2017, and references therein). Applying the AFC model of Godoy et al. (2017) to the lavas of Araral suggests that the samples from this study underwent AFC processes in a plagioclase-dominated environment. The model also suggests that the lavas of Araral assimilated 10 – 20% crustal material, followed by closed-system fractional crystallisation. One data point suggests the assimilation of ~25% crustal material before closed-system fractional crystallisation.

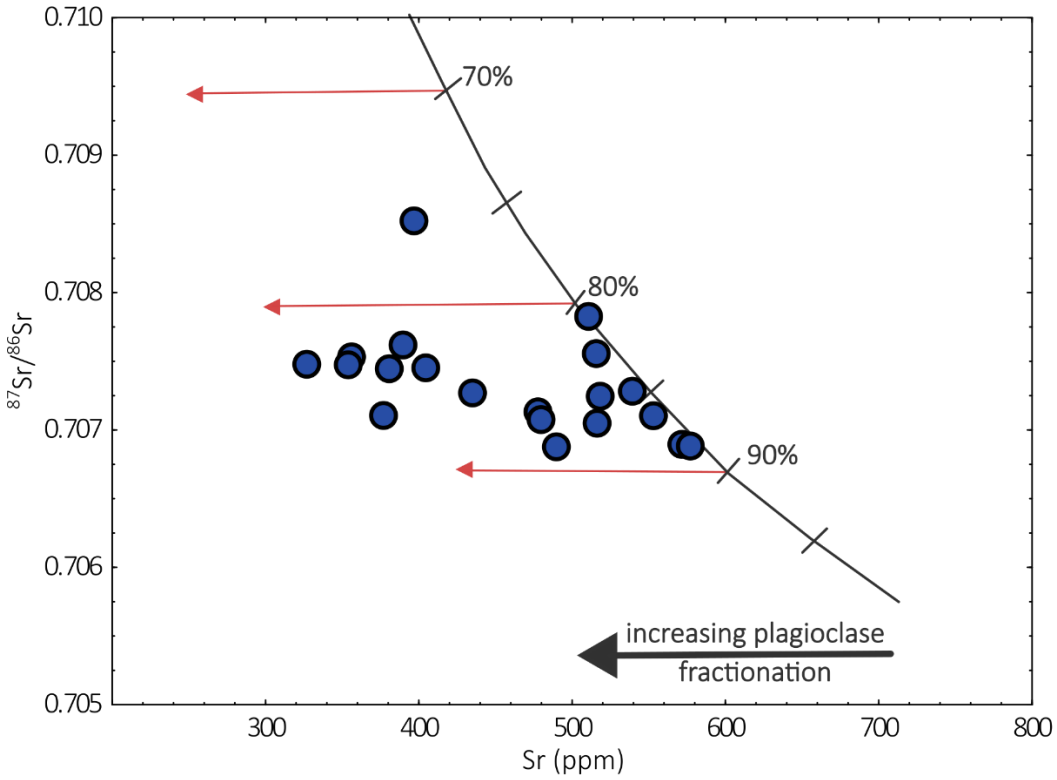

Figure 5.12. $^{87}Sr/^{86}Sr$ vs Sr. The curved line represents the AFC model from Godoy et al. (2017). The numbers along the curve indicate the estimated residual melt fraction (F%). The red arrows represent the proposed trends for closed system fractional crystallisation of magmas initially formed from AFC processes.

Like radiogenic isotopes, oxygen isotopes can be used as indicators of magma contamination by crustal assimilation and APMB contribution (e.g. Godoy et al., 2023; González-Maurel et al., 2020; Wörner et al., 2018). Mantle-derived and crustal lavas have distinct $\delta^{18}O$ values (Wörner et al., 2018). The $\delta^{18}O$ values for the mantle and mantle-derived lavas are characterised by relatively homogeneous and low $\delta^{18}O$, 5.7 ± 0.3 ‰ (Eiler, 2001; Wörner et al., 2018). Whereas crustal rocks are characterised by variable and high $\delta^{18}O$ values (Wörner et al., 2018). Additionally, there is minimal O isotope fractionation at mantle temperatures and $\delta^{18}O$ values of mineral separates are not affected by secondary alteration like whole-rock $\delta^{18}O$ values are (González-Maurel et al., 2020, and references therein).

Using the mineral-melt fractionation factors of $\Delta_{pyroxene\text{-}melt}$ = -0.7 ‰ and $\Delta_{plagioclase\text{-}melt}$ = -0.13 ‰ (González-Maurel et al., 2020; Zhao and Zheng, 2003), the estimated $\delta^{18}O$ values for equilibrium melt were calculated to be $\delta^{18}O_{melt\text{-}pyroxene}$ = 6.9 – 8.4 ‰ (n = 8) and $\delta^{18}O_{melt\text{-}plagioclase}$ = 6.7 – 7.6 (n = 4) (table 5.1). The average $\delta^{18}O$ of the equilibrium melt calculated for pyroxene and plagioclase are 7.5 ‰ and 7.2 ‰, respectively. For the calculation of average $\delta^{18}O_{melt\text{-}plagioclase}$, the $\delta^{18}O_{melt\text{-}plagioclase}$ value of VCA-21-040 was excluded because the $\delta^{18}O_{plagioclase}$ and, consequently, the $\delta^{18}O_{melt\text{-}plagioclase}$ values are outliers (9.2 ‰ and 9.3 ‰, respectively). The calculated values for the $\delta^{18}O$ of the equilibrium melt, given above, are higher than values for mantle-derived rocks from other subduction settings ($\delta^{18}O \leq 6.3$‰) and normal mid-ocean ridge basalts (N-MORB, $\delta^{18}O$ = 5.4 – 5.8 ‰; González-Maurel et al., 2020, and references therein). The high $\delta^{18}O$ and SiO_2 wt% indicate that the Araral lavas formed from an evolved magma that assimilated continental crust with high $\delta^{18}O$ values (González-Maurel et al., 2020). The calculated $\delta^{18}O_{melt}$ values of some samples are lower than the calculated $\delta^{18}O$ value for the sub-arc parent melt (7.0 ± 0.3 ‰; González-Maurel et al., 2020), but the values overlap with the 0.3 ‰ error.

Table 5.1. Oxygen isotope data and estimated $\delta^{18}O$ values for the melt ($\delta^{18}O_{melt\text{-}mineral}$) calculated using mineral-melt fractionation factors of $\Delta_{pyroxene\text{-}melt}$ = -0.7‰ and $\Delta_{plagioclase\text{-}melt}$ = -0.13‰.

sample	rock type	SiO_2 (wt%)	$\delta^{18}O_{pyroxene}$ (‰)	$\delta^{18}O_{melt\text{-}pyroxene}$ (‰)	$\delta^{18}O_{plagioclase}$ (‰)	$\delta^{18}O_{melt\text{-}plagioclase}$ (‰)
VCA-21-004	andesite	60.30	6.5	7.2		
VCA-21-012	dacite	65.88	6.7	7.4	7.2	7.4
VCA-21-015	andesite	61.95	6.4	7.1	6.6	6.7
VCA-21-029	andesite	61.88	6.2	6.9	7.5	7.6
VCA-21-040	dacite	67.15	6.6	7.3	9.2	9.3
			7.0	7.7		
VCA-21-044	andesite	59.89	7.7	8.4		
VCA-21-048	andesite	61.98	7.0	7.7	6.9	7.0

The binary mixing models by González-Maurel et al. (2020) shown in Figure 5.13 use the geochemical values of the Central Andean continental crust and predicted values for the sub-arc parent melt. The sub-arc parent melt is characterised by SiO_2 = 55.5 wt%; $^{87}Sr/^{86}Sr$ = 0.7055; and $\delta^{18}O$ = 7.0 ‰ (González-Maurel et al., 2020). The crustal contaminant C1 is characterised by SiO_2 = 67.0 wt%; $^{87}Sr/^{86}Sr$ = 0.7277; and $\delta^{18}O$ = 11.8 ‰ (Damm et al., 1990). The crustal contaminant C2 is characterised by SiO_2 = 70.0 wt%; $^{87}Sr/^{86}Sr$ = 0.7140; and $\delta^{18}O$ = 19.5 ‰ (Davidson et al., 1990). The binary mixing models indicate the incorporation of 0 – 20 % crustal material into the sub-arc parent melt. The binary mixing models suggest that the lavas of Araral generally underwent less than 10% incorporation of crustal materials, some data points suggest between 10 – 20% incorporation of crustal material, and two data points suggest ~30% and ~50% crustal incorporation. Most of the data points do not plot within the mixing space between the sub-arc magma and the crustal contaminants (fig. 5.13b), which is consistent with minimal interaction with the APMB and minimal crustal contamination of the sub-arc magma at the western margin (González-Maurel et al., 2020; Godoy et al., 2023).

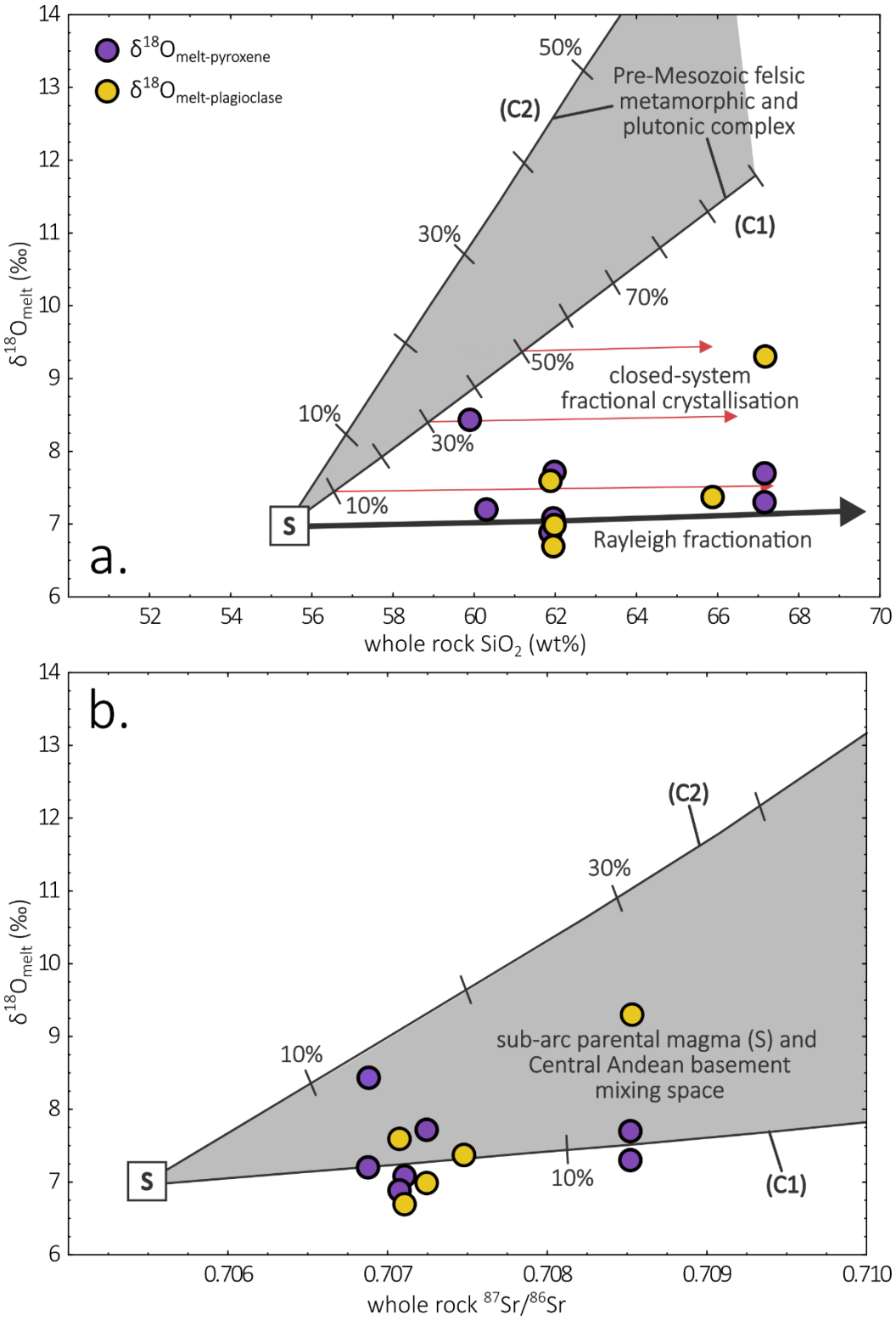

Figure 5.13. Binary mixing models of estimated $\delta^{18}O_{melt}$ from clinopyroxene and plagioclase (González-Maurel et al., 2020). (a) $\delta^{18}O_{melt}$ vs whole rock SiO_2. (b) $\delta^{18}O_{melt}$ vs whole rock $^{87}Sr/^{86}Sr$. The sub-arc Andean parental melt is represented by S (González-Maurel et al., 2020). The curves C1 and C2 represent the upper Central Andean continental crust (Damm et al., 1990; Davidson et al., 1990).

The results for Araral from the AFC model and binary mixing models are consistent with each other (fig. 5.12 and fig. 5.13; Godoy et al., 2017; González-Maurel et al., 2020). The AFC mixing models indicate 10 – 20% incorporation of crustal material and the binary mixing models 0 – 20%. The data point at ~30% (binary mixing model) is from VCA-21-044, the sample with the lowest SiO_2. The data points at ~25% (AFC model) and ~50% (binary mixing model) are both from VCA-21-040, the sample with the highest SiO_2. The AFC and binary mixing models are best reconciled by the magmas undergoing 0 – 20% crustal assimilation and later closed system fractionation (fig. 5.12 and 5.13, Godoy et al., 2014, 2017; González-Maurel et al., 2020). Like LREE/HREE ratios and Eu anomalies, the AFC model also suggests magma differentiation occurred at shallow crustal levels. The proposed model is that mantle-derived magma stagnates in the lower crust and assimilates basement rocks to form a sub-arc parental magma that is characterised by baseline isotopic values of $^{87}Sr/^{86}Sr \approx 0.705$ and $\delta^{18}O \approx 7.0 \pm 0.3‰$. (Davidson et al., 1990; Godoy et al., 2014; González-Maurel et al., 2020). This sub-arc parent melt was formed from the assimilation of ±20 % of continental crust ($\delta^{18}O$ = 6.4 – 11.8 ‰) into mantle-derived melts (González-Maurel et al., 2020). The parent magma then ascends and differentiates at mid and shallow crustal levels (Godoy et al. 2014). The melt that ascends along the western margin of the APMB avoids extensive contamination by the APMB (fig. 5.14; González-Maurel et al., 2019a).

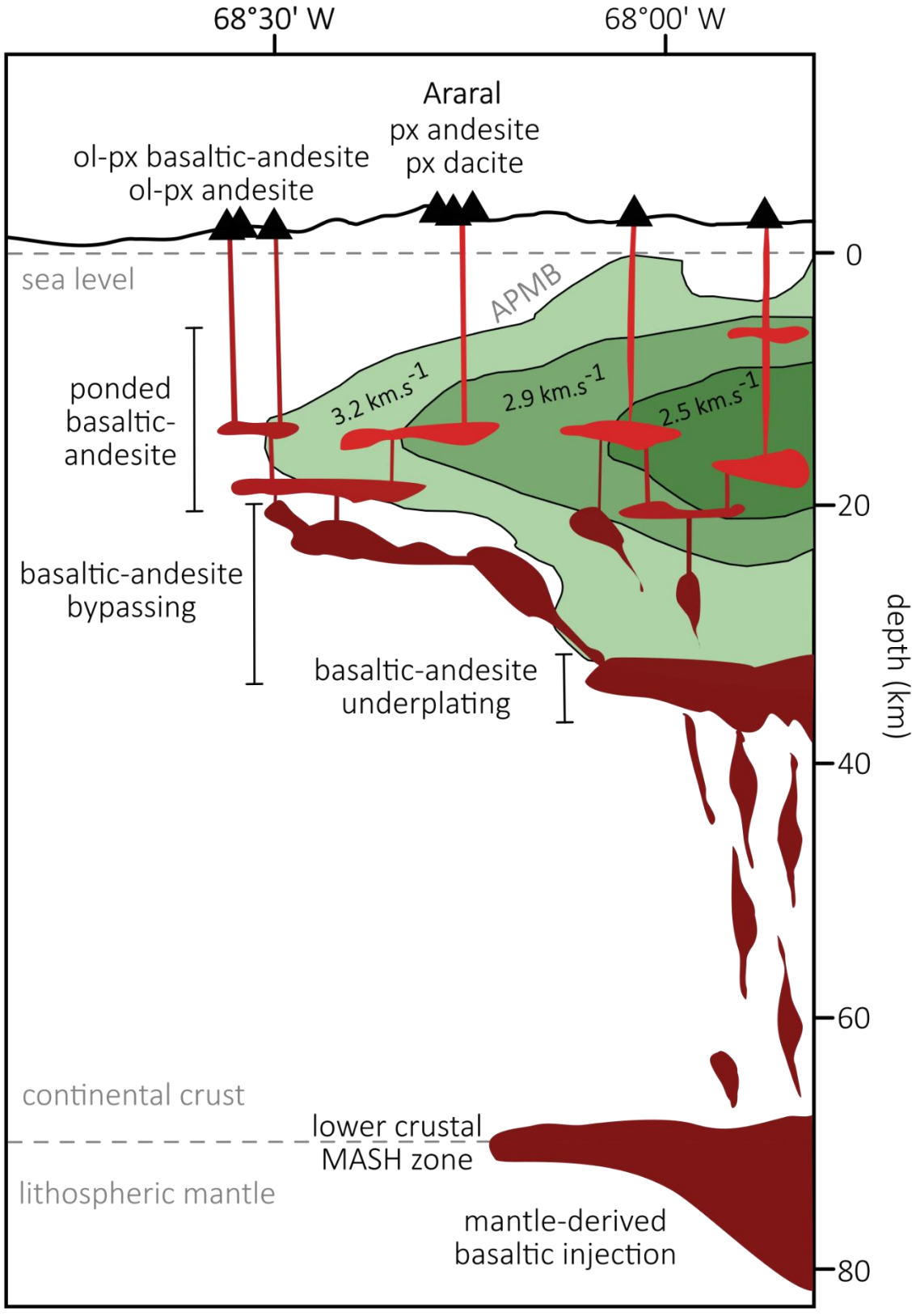

Figure 5.14. Schematic diagram of a cross-section showing the magmatic evolution of mafic APVC lavas (González-Maurel et al., 2019a). The green areas represent an approximate cross-section of the APMB based on the joint ambient noise-receiver function inversion S-velocity model from Ward et al. (2014).

5.3. Evidence of APMB influence:

The models by Godoy et al. (2017) and González-Maurel et al. (2020) suggest varying degrees of crustal assimilation into the sub-arc parent magma (fig. 5.12 and 5.13). The AFC model and geochemistry (e.g., low LREE/HREE ratios and negative Eu anomalies) also suggest magma evolution of the lavas of Araral occurred in a predominantly shallow environment. The similarities in the geochemistry of Araral and other lavas in the APVC indicate that the lavas of Araral were formed from similar magmatic processes. The models (fig. 5.12 and 5.13), petrography, geochemistry, and geochemical similarities with other APVC lavas suggest AFC processes and magma mixing.

The shallow crustal magmatic evolution of the lavas of Araral along with the petrographic, geochemical, and isotopic similarities with lavas of known APMB influence suggest that the APMB had a role in the magmatic evolution of the lavas of Araral. Like other lavas along the western margin, the lavas of Araral had minimal interaction with APMB – lower $^{87}Sr/^{86}Sr$ and higher $^{143}Nd/^{144}Nd$ than Uturuncu (fig. 5.10a; Godoy et al., 2017; González-Maurel et al., 2019a). Despite minimal interaction with the APMB, the geochemical and isotopic signatures of Araral and other lavas along the western margin have a strong APMB influence because anatectic melts mix more effectively into the sub-arc parent melt than solid crust (Godoy et al., 2017). When compared to the Central Andean array, data from Araral and other APVC lavas suggest magma differentiation in the shallow crust and more crustal contamination – i.e. low LREE/HREE ratios, higher $^{87}Sr/^{86}Sr$, and lower $^{143}Nd/^{144}Nd$. These geochemical and isotopic distinctions are likely caused by APMB influence.

The geochemical similarities between Araral, other Pliocene APVC lavas and Quaternary APVC lavas suggest that the APMB has likely been spatially fixed since the Pliocene (González-Maurel et al., 2019a). Ignimbritic activity dating 8.3 Ma alludes to the APMB being present and active before the Pliocene (Salisbury et al., 2011; González-Maurel et al., 2019a) with multiple flare-ups and input of mantle-derived magmas sustained during the waning phases of the magma cycle as well (Burns et al., 2015; de Silva et al., 2015). Comparison of Pliocene and Quaternary volcanoes on the same velocity contours – i.e. Araral with Cerro del Azufre on the 3.2 $km.s^{-1}$ contour and Ascotán with Apacheta and Paniri on the 2.9 $km.s^{-1}$ contour – shows elevated baseline $^{87}Sr/^{86}Sr$ in Pliocene lavas (fig. 5.2; González-Maurel et al., 2019a).

This indicates that while the APMB has been spatially fixed since the Pliocene, zones of higher partial melt may have had a greater extent in the Pliocene (González-Maurel et al., 2019a).

Araral also has a higher baseline $^{87}Sr/^{86}Sr$ ratio than San Pedro – another Quaternary volcano on the present-day 3.2 km.s^{-1} contour (González-Maurel et al., 2019a and references therein, table 5.2). Generally, Araral is characterised by higher $^{87}Sr/^{86}Sr$ than Cerro del Azufre and San Pedro but has significant overlap with Cerro del Azufre (fig. 5.15a). Additionally, the baseline $^{143}Nd/^{144}Nd$ ratio of Araral is lower than those of San Pedro and Cerro del Azufre (González-Maurel et al., 2019a and references therein, table 5.2). There is a significant overlap with $^{143}Nd/^{144}Nd$ ratios with Cerro del Azufre (fig. 5.15b). There is some overlap with $^{143}Nd/^{144}Nd$ ratios of San Pedro, but San Pedro predominantly has higher $^{143}Nd/^{144}Nd$ ratios than the other three volcanoes on the 3.2 km.s^{-1} velocity contour. Ollagüe has higher $^{87}Sr/^{86}Sr$ and lower $^{143}Nd/^{144}Nd$ ratios than all the other lavas on the 3.2 km.s^{-1} contour, and the $^{87}Sr/^{86}Sr$ ratios have some overlap with those of the lavas of Araral and Cerro del Azufre (fig. 5.15). However, the general trend is that Araral shows higher Sr isotope ratios and lower baseline Nd isotope ratios than the other Quaternary lavas on the present-day 3.2 km.s^{-1} velocity contour – Cerro del Azufre and San Pedro. The higher Sr isotope ratios and lower baseline Nd isotope ratios suggest more interaction with the APMB (Godoy et al., 2023). Araral, therefore, generally shows more interaction with the APMB relative to Quaternary volcanoes on the same velocity contour.

The observations made in this study are consistent with the APMB being stationary since the Pliocene and being sustained by repeated magma replenishment (Burns et al., 2015; de Silva et al., 2015; González-Maurel et al., 2019a). The petrographic textures of the Araral and other APVC lavas (i.e. oscillatory zoning, reaction rims) all indicate the mixture of felsic and mafic magmas (Godoy et al., 2022, and references therein). These textures are observed in both Pliocene and Quaternary lavas suggesting that these magma mixing processes and magma replenishment have occurred since the Pliocene (Godoy et al., 2022, and references therein). The greater extent of zones of higher degrees of partial melt in the Pliocene may be a result of a higher degree of magma production during the Pliocene (de Silva et al., 2006; González-Maurel et al., 2019a). The main pulses of the ignimbrite activity occurred during the late Miocene and Pliocene (10, 8, 6 and 4 Ma) and these large fluxes of ignimbrites are suggested to reflect larger amounts of magma production (de Silva et al., 2006). The replenishment of

the APMB with larger amounts of hotter primitive melt during the Pliocene could have resulted in the APMB being hotter and thus a greater spatial extent for the zones of high partial melt during the Pliocene. This resulted in the magma that formed the lavas of Araral having a higher degree of interaction with the APMB than those that formed Quaternary volcanoes on the present-day 3.2. km.s^{-1} velocity contour, as reflected by Sr and Nd isotope ratios.

Table 5.2. Baseline isotopic values of volcanoes on the present-day 3.2 km.s^{-1} velocity contour (this study; González-Maurel et al., 2019a and references therein).

sample	volcano	SiO_2 (wt%)	$^{87}Sr/^{86}Sr$	$^{143}Nd/^{144}Nd$
VCA-21-044	Araral	59.89	0.70688	0.51233
OLA9017	Ollagüe	52.90	0.70632	–
Cda_1_4	Cerro del Azufre	58.10	0.70651	0.51244
SPE-10	San Pedro	55.17	0.70667	0.51237

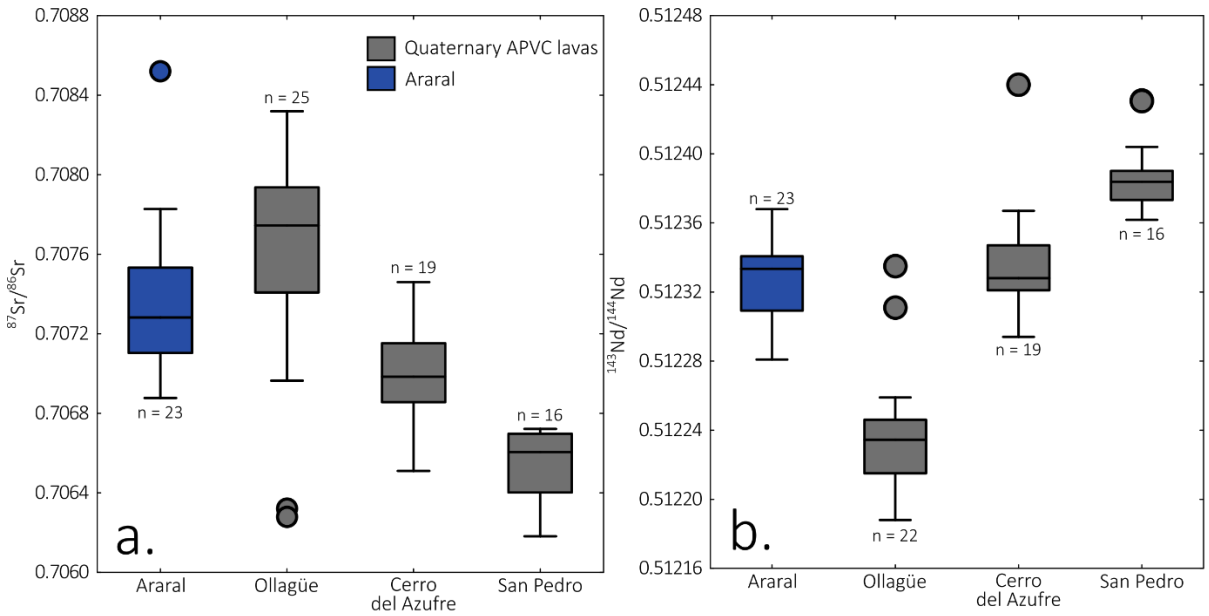

Figure 5.15. (a) Box and whisker plot of $^{87}Sr/^{86}Sr$. (b) Box and whisker plots of $^{143}Nd/^{144}Nd$. The blue dot and boxes represent Araral including data from this study and González-Maurel et al. (2019a). The grey dots and boxes represent the data from Quaternary APVC lavas on the same velocity contour as Araral – 3.2 km.s^{-1}, Ollagüe, Cerro del Azufre, and San Pedro (Feeley and Davidson, 1994; Godoy et al., 2014, 2017; González-Maurel et al., 2019a, and references therein; Lister, 2019).

6. Conclusion:

The lavas of Araral are andesites and dacites with phenocrysts of plagioclase, pyroxene, biotite, hornblende, and olivine (in order of abundance and prevalence). The petrography of the samples suggests three distinct groups based on the most abundant mafic phenocryst phase(s) – olivine-, pyroxene-, and biotite-rich. However, there is little geochemical and isotopic distinction between these groups. The phenocrysts exhibit disequilibrium textures (oscillatory zoning, sieve textures, opacitic rims, and spherulites), which suggest magma mixing, along with thermal and geochemical heterogeneity in the magma. The samples have low LREE/HREE and negative Eu/Eu*, indicating that magma evolution occurred at shallow crustal levels. The radiogenic and O isotope values of the lavas of Araral suggest crustal contamination. The $^{143}Nd/^{144}Nd$ values are lower whereas the $^{87}Sr/^{86}Sr$ and $\delta^{18}O$ values are higher than those of primitive lavas. Additionally, the Araral lavas have higher $^{87}Sr/^{86}Sr$ and lower $^{143}Nd/^{144}Nd$ values than the rest of CVZ, suggesting a higher degree of crustal contamination. The Pb isotope values reflect the values of the local underlying basement. The petrography is consistent with lavas of known APMB influence, as is the geochemical and isotopic data. The petrography, trace element and isotope data, and the similarities with other APVC lavas suggest that the APMB had a role in the magmatic evolution of the lavas of Araral.

The petrography, comparison with existing AFC and binary mixing models suggest that the lavas of Araral were formed from magma mixing and AFC processes – specifically, crustal assimilation followed by closed-system fractional crystallisation at shallow crustal levels. The magmatic evolution of the lavas of Araral is initiated in the lower crust with the injection of mantle-derived magma into the lower crustal MASH zone. The sub-arc parent magma is formed from the assimilation of crustal components into mantle-derived magma. This sub-arc parent magma is a basaltic-andesite and ascends to the upper crust and undergoes further differentiation in an upper crustal MASH-zone – likely the APMB.

The lavas of Araral are generally consistent with the Central Andean Array. The AFC and binary mixing models also indicate that the lavas of Araral had minimal interaction with the APMB. Further, the lavas of Araral and other volcanoes along the western margin of the APMB are characterised by lower $^{87}Sr/^{86}Sr$ and higher $^{143}Nd/^{144}Nd$ than those at the centre – i.e. Uturuncu. This is attributed to lower degrees of interaction with the APMB for the magma

that formed the lavas of Araral and other volcanoes along the margins, where the degree of partial melt is lower. Despite the limited interaction with the APMB the isotope values are still strongly influenced by the APMB because of its partially molten state – crustal melts are more efficiently incorporated than solid crust.

The implication of APMB influence on the lavas of Araral suggests that the APMB has been present and active since the Pliocene. Comparison of the Sr and Nd isotope ratios of Araral and Quaternary lavas on the present-day 3.2 km.s^{-1} velocity contour shows that Araral has higher $^{87}Sr/^{86}Sr$ and lower baseline $^{143}Nd/^{144}Nd$ values than the Quaternary lavas on the same velocity contour – except for Ollagüe. This suggests a higher degree of interaction with the APMB for the magma that formed the lavas of Araral. This is consistent with what has been observed with other Pliocene and Quaternary volcanoes on other velocity contours. These observations indicate that the APMB has been spatiotemporally fixed since the Pliocene but the spatial extent of the zones of higher partial melt has decreased. This likely is a result of a reduced degree of melt production in the APMB since the formation of Araral.

References:

Allmendinger, R.W., Jordan, T.E., Kay, S.M., and Isacks, B. L. 1997. The evolution of the Altiplano-Puna Plateau of the central Andes. *Annual Review of Earth and Planetary Sciences*, 25(1), 139-174.

Angermann, D., Klotz, J., and Reigber, C. 1999. Space-geodetic estimation of the Nazca-South America Euler vector. *Earth and Planetary Science Letters*, 171(3), 329–334.

Annen, C. and Sparks, R.S.J. 2002. Effects of repetitive emplacement of basaltic intrusions on thermal evolution and melt generation in the crust. *Earth and Planetary Science Letters*, 203(3–4), 937–955.

Araya Vargas, J., Meqbel, N.M., Ritter, O., Brasse, H., Weckmann, U. Yáñez, G., and Godoy, B. 2019. Fluid Distribution in the Central Andes subduction zone imaged with magnetotellurics. *Journal of Geophysical Research: Solid Earth*, 124, 4017–4034.

Beck, S.L., Zandt, G., Myers, S.C., Wallace, T.C., Silver, P.G., and Drake, L., 1996. Crustal-thickness variations in the central Andes. *Geology*, 24(5), 407–410.

Bidart, N. 2014. Petrología y geoquímica de lavas recientes, al sureste del campo geotermal del Tatio. Dissertation, B.Sc. Thesis. Universidad de Chile, Santiago, Chile.

Blum-Oeste, M. and Wörner, G. 2016. Central Andean magmatism can be constrained by three ubiquitous end-members. *Terra Nova*, 28 (6), 434–440.

Burns, D.H., de Silva, S.L., Tepley III, F., Schmitt, A.K., and Loewen, M.W. 2015. Recording the transition from flare-up to steady-state arc magmatism at the Purico-Chascon volcanic complex, northern Chile. *Earth and Planetary Science Letters*, 422, 75–86.

Chmielowski, J., Zandt, G., and Haberland, C. 1999. The Central Andean, Altiplano-Puna Magma Body. *Geophysical Research Letters*, 26(6), 783-786.Damm K.-W. Pichowaik, S. Harmon, R.S., and Todt, W. 1990. Pre-Mesozoic Evolution of the Central Andes; The basement revisited. In: Kay, S.M. and Rapela, C.W. (eds), Plutonism from Antarctica to Alaska*, Geological Society of America Special Paper,* 241, 101–126.

Davidson, J.P., McMillan, N., Moorbath, S., Wörner, G., Harmon, R. S., and Lopez-Escobar, L. 1990. 'The Nevados de Payachata volcanic region (18°S/69°W, N. Chile): II. Evidence for widespread crustal involvement in Andean magmatism', *Contributions to Mineralogy and Petrology*, 105, 412–432.

Davidson, J.P., Harmon, R., and Wörner, G. 1991. The source of central Andean magmas: Some considerations. *Geological Society of America*, *Special Paper*, 265, 233–243.

Davidson, J.P., Turner, S., and Plank, T. 2013. Dy/Dy*: variations arising from mantle sources and petrogenetic processes. *Journal of Petrology*, 54(3), 525–537.

de Astis, G., Lucchi, F., Tranne, C.A., and Rossi, P.L. 2009. Evidence for different processes of magma Evolution in El Tatio volcanic region (22°16' to 22°30' S, Central Volcanic Zone, Andes). *Geoacta, Special Publication*, 2, 31–58.

de Silva, S. 1989. Altiplano-Puna volcanic complex of the central Andes. *Geology*, 17, 1102–1106.

de Silva, S., Zandt, G., Trumbull, R., Viramonte, J.G., Salas, G. and Jiménez, N. 2006. Large ignimbrite eruptions and volcano-tectonic depressions in the Central Andes: a thermomechanical perspective. In: Troise, C., De Natale, G. and Kilburn, C.R.J. (eds), *Mechanisms of Activity and Unrest at Large Calderas*, Geological Society, London, Special Publications, 269, 47–63.

de Silva, S.L. and Gosnold, W.D. 2007. Episodic construction of batholiths: insights from the spatiotemporal development of an ignimbrite flare-up. *Journal of Volcanology and Geothermal Research*, 167, 320–325.

de Silva, S.L., Kay, S.M., 2018. Turning up the heat: high-flux magmatism in the central Andes. *Elements*, 14(4), 245–250.

Eiler, J.M. 2001. Oxygen isotope variations of basaltic lavas and upper mantle rocks. *Reviews in mineralogy and geochemistry*, 43(1), 319–364.

Feeley, T.C. and Davidson, J.P., 1994. Petrology of calc-alkaline lavas at Volcán Ollagüe and the origin of compositional diversity at Central Andean stratovolcanoes. *Journal of Petrology*, 35(5), 1295–1340.

Feeley, T.C. and Sharp, Z.D. 1995. $^{18}O/^{16}O$ isotope geochemistry of silicic lava flows erupted from Volcán Ollagüe, Andean Central Volcanic Zone. Earth and Planetary Science Letters, **133(3-4)**, 239–254.

Figueroa, J., and Figueroa, O., 2006. Petrografía y geoquímica de las lavas del volcán Sairecabur, Andes Centrales, Chile. *Actas*, **2**, 459–462.

Figueroa, O., Déruelle, B., and Demaiffe, D. 2009. Genesis of adakite-like lavas of Licancabur volcano (Chile—Bolivia, Central Andes*). Comptes Rendus Geoscience*, **341(4)**, 310–318.

Freymuth, H., Brandmeier, M., and Wörner, G. 2015. The origin and crust/mantle mass balance of Central Andean ignimbrite magmatism constrained by oxygen and strontium isotopes and erupted volumes. *Contributions to Mineralogy and Petrology*, **169(6)**, 58.

Galer, S.J.G., and Abouchami, W. 1998. Practical application of lead triple spiking for correction of instrumental mass discrimination. *Mineralogical Magazine*, **62A**, 491–492

Giese, P., Scheuber, E. Schilling, F., Schmitz, M., and Wigger, P. 1999. Crustal thickening processes in the central Andes and the different natures of the Moho-discontinuity, *Journal of South American Earth Sciences*, **12**, 201-220.

Godoy, B., Wörner, G., Kojima, S., Aguilera, F., Simon, K., and Hartmann, G. 2014. Low-pressure evolution of arc magmas in thickened crust: The San Pedro-Linzor volcanic chain, Central Andes, Northern Chile. *Journal of South American Earth Sciences*, **52**, 24–42.

Godoy, B., Wörner, G., le Roux, P., de Silva, S. Parada, M.Á., Kojima, S., González-Maurel, O., Morata, D., Polanco, E., and Martínez, P. 2017. Sr- and Nd- isotope variations along the Pleistocene San Pedro – Linzor volcanic chain, N. Chile: Tracking the influence of the upper crustal Altiplano-Puna Magma Body. *Journal of Volcanology and Geothermal Research*, **341**, 172–186.

Godoy, B., Lazcano, J., Rodríguez, I., Martínez, P., Parada, M.A., le Roux, P., Wilke, H.-G., and Polanco, E. 2018. Geological evolution of Paniri volcano, Central Andes, northern Chile. *Journal of South American Earth Sciences*, **84**, 184–200.

Godoy, B., Marco, T., González-Maurel, O., Renzulli, A., Hernández-Prat, L., le Roux, P., Morata, D. and Menzies, A. 2019. Linking the mafic volcanism with the magmatic stages during the

last 1 Main the main volcanic arc of the Altiplano-Puna Volcanic Complex (Central Andes). *Journal of South American Earth Sciences*, 95, 1–11.

Godoy, B., Taussi, M., González-Maurel, O., Hüber, D., Lister, J., Sellés, D., le Roux, P., Renzulli, A., Rivera, G., and Morata, D. 2022. Evolution of the Azufre volcano (northern Chile): Implications for the Cerro Pabellón Geothermal Field as inferred from long lasting eruptive activity. *Journal of Volcanology and Geothermal Research*, 423, 1–20.

Godoy, B., González-Maurel, O., Harris, C., e Roux, P., and Lister, J. 2023. Oxygen and radiogenic isotopes require different contamination paths in the Azufre volcano, Central Andes, northern Chile.

González-Maurel, O., le Roux, P., Godoy, B., Troll, V.R., Deegan, F.M., and Menzies, A. 2019a. The great escape: Petrogenesis of low-silica volcanism of Pliocene to Quaternary age associated with the Altiplano-Puna Volcanic Complex of northern Chile (21°10′-22°50′S). *Lithos*, 346–347, 1–15.

González-Maurel, O., Godoy, B., le Roux, P., Rodríguez, I., Marín, C., Menzies, A., Bertin, D.M., Morata, D., and Vargas, M. 2019b. Magmatic differentiation at La Poruña scoria cone, Central Andes, northern Chile: Evidence for assimilation during turbulent ascent processes, and genetic links with mafic eruptions at adjacent San Pedro volcano. *Lithos*, 338–339, 128–140.

González-Maurel, O., Deegan, F.M., le Roux, P. Harris, C., Troll, V.R. and Godoy, B. 2020. Constraining the sub-arc, parental magma composition for the giant Altiplano-Puna Volcanic Complex, northern Chile. *Scientific Reports*, 10(1), 1–10.

Harmon, R.S., Thorpe, R.S., Francis, P.W., 1981. Petrogenesis of Andean andesites from combined O–Sr isotope relationships. *Nature*, 290(5805), 396–399.

Harris, C., and Vogeli, J. 2010. Oxygen isotope composition of garnet in the Peninsula Granite, Cape Granite Suite, South Africa: constraints on melting and emplacement mechanisms. *South African Journal of Geology*, 113(3-4), 387–414.

Hickey-Vargas, R., Moreno, H., Lopez-Escobar, L., Frey, F.A. 1989. Geochemical variations in Andean basaltic and silicic lavas from the Villarrica–Lanin volcanic chain (39.5 degrees S): an evaluation of source heterogeneity, fractional crystallization and crustal assimilation. *Contributions to Mineralogy and Petrology*, 103, 361–386.

Hildreth, W. and Moorbath, S., 1988. Crustal contributions to arc magmatism in the Andes of Central Chile. *Contributions to Mineralogy and Petrology,* 98(4), 455–489.

Irvine, T.N.J. and Baragar, W.R.A.F. 1971. A guide to the chemical classification of the common volcanic rocks. *Canadian Journal of Earth Sciences*, 8(5), 523–548.

Kay, S., Coira, B., and Viramonte, J. 1994. Young mafic back arc volcanic rocks as indicators of continental lithospheric delamination beneath the Argentine Pune plateau. *Journal of Geophysical Research*, 99, 24323–24339.

Komárek, M., Ettler, V., Chrastný, V., and Mihaljevič, M. 2007. Lead isotopes in environmental sciences: A review. *Environment International*, 34, 562–577.

Le Maitre, R.W., Bateman, P., Dudek, A., Keller, J., Lameyre, J., Le Bas, M.J., Sabine, P.A., Schmid, R., Sorensen, H., Strekeisen, A., Woolley, A.R., and Zanettin, B. 1989. *A classification of igneous rocks and glossary of terms: Recommendations of the International Union of Geological Sciences, Subcommission on the Systematics of Igneous Rocks*. Blackwell Scientific Publications, Oxford. pp. 193.

Lister, J. 2019. *Petrogenesis of lavas from Volcano Azufre, Northern Chile: evidence for crustal input.* Masters Thesis. University of Cape Town, South Africa.

Mamani, M., Tassara, A., Wörner, G., 2008. Composition and structural control of crustal domains in the Central Andes. *Geochemistry Geophysics Geosystems*, 9(3), 1–3.

Mamani, M., Wörner, G., Sempere, T., 2010. Geochemical variations in igneous rocks of the Central Andean orocline (13°S to 18°S): tracking crustal thickening and magma generation through time and space. *Geological Society of America Bulletin*, 122 (1–2), 162–182.

Mattioli, M., Renzulli, A., Menna, M., and Holm, P.M. 2006. Rapid ascent and contamination of magmas through the thick crust of the CVZ (Andes, Ollagüe region): Evidence from a nearly aphyric high-K andesite with skeletal olivines. *Journal of Volcanology and Geothermal Research*, 158, 87–105.

Maza, S.N., Collo, G., Morata, D., Taussi, M., Vidal, J., Mattioli, M., and Renzulli, A. 2021. Active and fossil hydrothermal zones of Apacheta volcano: Insights for Cerro Pabellón hidden geothermal system (Northern Chile). *Geothermics*, 96, 1–2.

McKay, G.A., 1989. Partitioning of rare earth elements between major silicate minerals and basaltic melts. *Reviews in Mineralogy and Geochemistry*, **21(1)**, 45–77.

Michelfelder, G.S., Feeley, T.C., Wilder, A.D, and Klemetti, E.W. 2013. Modification of the Continental Crust by Subduction Zone Magmatism and Vice-Versa: Across-Strike Geochemical Variations of Silicic Lavas from Individual Eruptive Centers in the Andean Central Volcanic Zone. *Geosciences*, **3**, 633–667.

Nixon, G.T. and Pearce, T.H. 1987. Laser-interferometry study of oscillatory zoning in plagioclase: The record of magma mixing and phenocryst recycling in calc-alkaline magma chambers, Iztaccihuatl volcano, Mexico. *American Mineralogist*, **72**, 1144–1162.

Pichowaik, S., Buchelt, M., and Damm, K.W. 1990. Magmatic activity and tectonic setting of the early stages of the Andean cycle in northern Chile. In*:* Kay, S.M. and Rapela, C.W. (eds*),* Plutonism from Antarctica to Alaska, *Geological Society of America*, Special Paper, **231**, 127–144.

Pin, C., Gannoun, A., and Dupont, A. 2014. Rapid, simultaneous separation of Sr, Pb, and Nd by extraction chromatography prior to isotope ratios determination by TIMS and MC-ICP-MS. *Journal of Analytical Atomic Spectrometry*, **29**, 1858–1870.

Plechov, P.Y., Tsai, A.E, Shcherbakov, V.D. and Dirksen, O.V. 2008. Opacitization Conditions of Hornblende in Bezymyannyi Volcano Andesites (March 30, 1956 Eruption). *Petrologiya*, **16(1)**, 21–37.

Ranero, C.R., von Huene, R., Wainrebe, W., and Reichert, C. 2006. Tectonic processes along the Chile convergent margin. In: Oncken, O., Chong, G., Franz, G., Giese, P., Götze, H.-J., Ramos, V.A., Strecker, M.R., Wigger, P. (eds.), *The Andes Active Subduction Orogeny, Frontiers in Earth Sciences, vol. 1*., Springer, Heidelberg, Germany, pp. 91–117.

Rickwood, P.C. 1989. Boundary lines within petrologic diagrams which use oxides of major and minor elements. *Lithos*, **22(4)**, 247–263.

Salfity, J.A., 1985. Lineamentos transversales al rumbo andino en el Noroeste Argentino. *IV Congreso Geológico Chileno*, 1985 Aug 19 – 24, Universidad Católica del Norte. Antofagasta, Chile, p. 119–137.

Salisbury, M.J., Jicha, B.R., de Silva, S.L., Singer, B.S., Jiménez, N.C., and Ort, M.H. 2011. $^{40}Ar/^{39}Ar$ chronostratigraphy of Altiplano-Puna volcanic complex ignimbrites reveals the development of a major magmatic province. *Geological Society of America Bulletin*, 123(5–6), 821–840.

Scheuber, E. and Reutter, K.-J., 1992. Magmatic arc tectonics in the Central Andes between 21°and 25°S. *Tectonophysics*, 205 (1–3), 127–140.

Schmitz, M., Heinsohn, W.D., and Schilling, F.R. 1997. Seismic, gravity and petrologic evidence for partial melt beneath the thickened Central Andean crust (21 – 23°S). *Tectonophysics*, 270, 313–326.

Seaman, S.J., Dyar, M.D., and Marinkovic, N. 2009. The effects of heterogeneity in magma water concentration on the development of flow banding and spherulites in rhyolitic lava. *Journal of Volcanology and Geothermal Research*, 183, 157–169

Sellés, D. and Gardeweg, M., 2017. Geología del área Ascotán-Cerro Inacaliri, Región de Antofagasta. Servicio Nacional de Geología y Minería, Carta Geológica de Chile, Serie Geología Básica 190:73p., 1 mapa escala 1:100.000. Santiago, Chile.

Stern C.R. 2004. Active Andean volcanism: its geology and tectonic setting. *Revista Geológica de Chile*, 31(2), 161–206.

Sun, S.-s. and McDonough, W.F. 1989. Chemical and isotopic system of oceanic basalts: implications for mantle composition and processes. *Geological Society, London, Special Publications*, 42, 313–345.

Tanaka, T., Togashi, S., Kamioka, H., and Amakawa, H. 2000. JNdi-1: a neodymium isotopic reference in consistency with LaJolla neodymium. *Chemical Geology*, 168, 279–281.

Taylor, S.R. and McLennan, S.M. 1988. The significance of the rare earths in geochemistry and cosmochemistry. *Handbook on the physics and chemistry of rare earths*, 11, 485–578.

Thorpe, R.S. 1984. The Tectonic Setting of Active Andean Volcanism. In: Harmon, R.S. and Barreiro, B.A. (eds*), Andean magmatism: Chemical and Isotopic Constraints, Shiva Geology Series,* Shiva Publishing Limited, Natwich, United Kingdom, pp. 4–8.

Tibaldi, A., Bistacchi, A., Pasquare, F.A., Vezzoli, L., 2006. Extensional tectonics and volcano lateral collapses: insights from Ollagüe volcano (Chile-Bolivia) and analogue modelling. *Terra Nova*, **18(4)**, 282–289.

Trumbull, R.B., Wittenbrink, R., Hahne, K., Emmermann, R., Büsch, W., Gerstenberger, H., and Siebel, W. 1999. Evidence for Late Miocene to Recent contamination of arc andesites by crustal melts in the Chilean Andes (25–26°S) and its geodynamic implications. *Journal of South American Earth Sciences*, **12**, 135–155.

Trumbull, R., Riller, U., Oncken, O., Scheuber, E., Munier, K., Hongn, F., 2006. The time-space distribution of Cenozoic volcanism in the South-Central Andes: a new data compilation and some tectonic implications. In: Oncken, O., Chong, G., Franz, G., Giese, P., Götze, H.-J., Ramos, V.A., Strecker, M.R., and Wigger, P. (eds), *The Andes Active Subduction Orogeny, Frontiers in Earth Sciences*. 1, Springer, Heidelberg, Germany. pp. 29–43.

Vezzoli, L., Tibaldi, A., Renzulli, A., Menna, M., Flude, S. 2008. Faulting-assisted lateral collapses and influence on shallow magma feeding system at Ollagüe volcano (Central Volcanic Zone, Chile-Bolivia Andes). *Journal of Volcanology and Geothermal Research*, **171**, 137–159.

Waight, T., Baker, J., and Peate, D., 2002. Sr isotope ratio measurements by double-focusing MC-ICPMS: techniques, observations and pitfalls. *International Journal of Mass Spectrometry*, **221**, 229-244.

Ward, K. M., Zandt, G., Beck, S. L., Christensen, D. H., and McFarlin, H. 2014. Seismic imaging of the magmatic underpinnings beneath the Altiplano-Puna volcanic complex from the joint inversion of surface wave dispersion and receiver functions. *Earth and Planetary Science Letters*, **404**, 43–53.

Watts, R.B., de Silva, S.L., de Rios, G.J., and Croudace, I. 1999. Effusive eruption of viscous silicic magma triggered and driven by recharge: a case study of the Cerro Chascon-Runtu Jarita Dome Complex in Southwest Bolivia. *Bulletin of Volcanology*, **61(4)**, 241–264.

Wörner, G., Mamani, M., and Blum-Oeste, M. 2018. Magmatism in the Central Andes. *Elements*, **14(4)**, 237–244.

Zandt, G., Leidig, M., Chmielowski, J., Baumont, D., and Yuan, X. 2003. Seismic detection and characterization of the Altiplano-Puna magma body, Central Andes. *Pure and Applied Geophysics*, 160(3), 789–807.

Zhao, Z.-F. and Zheng, Y.-F. 2003. Calculation of oxygen isotope fractionation in magmatic rocks. *Chemical Geology*, 193, 59–80.

Supplementary materials:

Table S1. Petrographic descriptions of samples from Araral.

sample	classification	texture(s)	minerals	modal abundance (%)	grain size (mm)	mineral description
olivine-rich group						
VCA-21-015	andesite					
		hypocrystalline, porphyritic, glomeroporphyritic, glassy groundmass with microlites				
			plagioclase	27	<2	anhedral - subhedral, oscillatory zoning, albite twinning
			olivine	20	<1	anhedral
			clinopyroxene	5	<2	anhedral
			orthopyroxene	1	<1	anhedral
			hornblende	1	<1	subhedral - euhedral
			biotite	1	<1	subhedral
			opaque mineral(s)	5	<0.4	anhedral - subhedral
			groundmass	40		
VCA-21-048	andesite					
		hypocrystalline, porphyritic, glomeroporphyritic, glassy groundmass with microlites				
			plagioclase	30	<3	subhedral, oscillatory zoning, Carlsbad twinning, albite twinning
			clinopyroxene	10	<2	anhedral - subhedral, simple twinning
			olivine	10	<2	anhedral - subhedral
			opaque mineral(s)	10	<1	anhedral
			groundmass	40		

sample	classification	texture(s)	minerals	modal abundance (%)	grain size (mm)	mineral description
pyroxene-rich group						
VCA-21-002	andesite					
		hypocrystalline, porphyritic, glomeroporphyritic, glassy groundmass with microlites, groundmass is predominantly light with some parts containing darker groundmass in irregular patch-like shapes	plagioclase	25	<3	subhedral - euhedral, Carlsbad twinning, albite twinning, periclase twinning oscillatory zoning
			orthopyroxene	15	<2	anhedral - subhedral
			clinopyroxene	15	<1	anhedral - subhedral, simple twinning
			opaque mineral(s)	5	<1	anhedral - subhedral
			groundmass	40		
VCA-21-003	andesite					
		hypocrystalline, porphyritic, glomeroporphyritic, glassy groundmass with microlites	plagioclase	30	<2	anhedral - subhedral, oscillatory zoning, albite twinning
			orthopyroxene	15	<1	anhedral - subhedral, simple twinning
			clinopyroxene	15	<1	anhedral - subhedral
			opaque mineral(s)	5	<0.25	anhedral
			groundmass	35		
VCA-21-004	andesite					
		hypocrystalline, porphyritic, glomeroporphyritic, glassy groundmass with microlites	plagioclase	25	<3	anhedral - subhedral, oscillatory zoning, Carlsbad twinning, albite twinning
			orthopyroxene	15	<1	anhedral - subhedral

sample	classification	texture(s)	minerals	modal abundance (%)	grain size (mm)	mineral description
			clinopyroxene	15	<2	anhedral - subhedral, simple twinning
			opaque mineral(s)	5	<0.25	anhedral
			groundmass	40		
VCA-21-009	andesite					
		hypocrystalline, porphyritic, glomeroporphyritic, glassy groundmass, groundmass is predominantly light with thick irregular discontinuous vein-like darker groundmass, crystals and microlites in darker groundmass are relatively aligned	plagioclase	20	<2	anhedral - subhedral, oscillatory zoning, albite twinning
			orthopyroxene	15	<2	anhedral - subhedral
			clinopyroxene	10	<1	anhedral - subhedral
			opaque mineral(s)	5	<0.5	anhedral
			groundmass	50		
VCA-21-012	dacite					
		hypocrystalline, porphyritic, glomeroporphyritic, glassy groundmass with microlites, groundmass is predominantly light, the darker groundmass is reddish in XPL and is either small, thin and vein-like or patch-like, crystals and microlites in the lighter groundmass are relatively aligned	plagioclase	20	<2	subhedral - euhedral, Carlsbad twinning, albite twinning, oscillatory zoning
			orthopyroxene	10	<0.5	anhedral - subhedral
			clinopyroxene	10	<1	anhedral - subhedral, simple twinning
			biotite	5	<2	subhedral - euhedral
			opaque mineral(s)	5	<1	anhedral
			groundmass	50		
VCA-21-016	dacite					
		hypocrystalline, porphyritic, glomeroporphyritic, glassy groundmass, contains both light and dark groundmass, appears to be layered/banded, the crystals and microlites seem aligned with the bands, lighter groundmass in reddish in XPL				

sample	classification	texture(s)	minerals	modal abundance (%)	grain size (mm)	mineral description
			plagioclase	15	<2	subhedral - euhedral, Carlsbad twinning, albite twinning, oscillatory zoning
			clinopyroxene	10	<1	anhedral - subhedral, simple twinning
			orthopyroxene	10	<0.5	anhedral - subhedral
			biotite	2	<1	subhedral - euhedral
			opaque mineral(s)	5	<1	anhedral
			groundmass	58		
VCA-21-019	dacite					
		hypocrystalline, porphyritic, glomeroporphyritic, glassy groundmass with microlites, groundmass is predominantly light in some parts and predominantly darker in others, darker groundmass is patch-like and reddish in XPL, the two are nearly indistinguishable in XPL, microlites seem to be aligned in darker groundmass, margins of some crystals in darker groundmass are red	plagioclase	25	<2	anhedral - subhedral, oscillatory zoning, Carlsbad twinning, albite twinning
			clinopyroxene	10	<1	anhedral, simple twinning
			hornblende	3	<1	subhedral
			biotite	1	<1	subhedral-euhedral
			orthopyroxene	1	<0.5	anhedral
			opaque mineral(s)	5	<0.5	
			groundmass	55		
VCA-21-026	dacite					
		hypocrystalline, porphyritic, glomeroporphyritic, glassy groundmass with microlites	plagioclase	25	<2	anhedral - subhedral, Carlsbad twinning, albite twinning
			clinopyroxene	10	<1	subhedral
			opaque mineral(s)	5	<1	anhedral
			groundmass	60		

sample	classification	texture(s)	minerals	modal abundance (%)	grain size (mm)	mineral description
VCA-21-038	dacite					
		hypocrystalline, porphyritic, glomeroporphyritic, glassy groundmass with microlites				
			plagioclase	30	<2	subhedral - euhedral, Carlsbad twinning, albite twinning, oscillatory zoning
			orthopyroxene	20	<1	anhedral - subhedral
			clinopyroxene	15	<0.5	anhedral - subhedral, simple twinning
			olivine	<1	<0.5	subhedral
			opaque mineral(s)	10	<0.5	anhedral - subhedral
			groundmass	25		
VCA-21-043	andesite	hypocrystalline, porphyritic, glomeroporphyritic, glassy groundmass with microlites				
			plagioclase	20	<2	anhedral - subhedral, oscillatory zoning, Carlsbad twinning, albite twinning
			clinopyroxene	10	<2	anhedral, simple twinning
			hornblende	7	<2	subhedral
			orthopyroxene	5	<0.5	anhedral
			biotite	3	<1	euhedral
			opaque mineral(s)	5	<0.5	anhedral - subhedral
			groundmass	50		
VCA-21-044	andesite	hypocrystalline, porphyritic, glomeroporphyritic, glassy groundmass with microlites, groundmass is predominantly light, darker groundmass is patch-like and reddish in XPL, the two are nearly in distinguishable in XPL, margins of some crystals in darker groundmass are red, microlites are relatively aligned				
			plagioclase	30	<2	subhedral - euhedral, Carlsbad twinning, albite twinning, oscillatory zoning

sample	classification	texture(s)	minerals	modal abundance (%)	grain size (mm)	mineral description
			orthopyroxene	10	<2	anhedral - subhedral, simple twinning
			clinopyroxene	10	<2	anhedral - subhedral, simple twinning
			biotite	8	<2	subhedral - euhedral
			hornblende	2	<1	euhedral
			opaque mineral(s)	5	<0.5	anhedral - subhedral
			groundmass	35		
VCA-21-045	dacite					
		hypocrystalline, porphyritic, glomeroporphyritic, glassy groundmass with microlites				
			plagioclase	30		subhedral - euhedral, oscillatory zoning, Carlsbad twinning, albite twinning
			orthopyroxene	15	<0.5	subhedral - euhedral
			clinopyroxene	10		Subhedral+
			opaque mineral(s)	5	<0.5	anhedral - subhedral
			groundmass	40		
RMM-22-001	andesite					
		hypocrystalline, porphyritic, glomeroporphyritic, glassy groundmass with microlites, spherulites and devitrification				
			plagioclase	30	<3	subhedral - euhedral, Carlsbad twinning, albite twinning, periclase twinning oscillatory zoning
			orthopyroxene	20	<1	subhedral - euhedral
			clinopyroxene	10	<1	anhedral - subhedral, simple twinning

sample	classification	texture(s)	minerals	modal abundance (%)	grain size (mm)	mineral description
			opaque mineral(s)	5	<0.5	anhedral - subhedral
			groundmass	40		
RMM-22-002	andesite					
		hypocrystalline, porphyritic, glomeroporphyritic, glassy groundmass with microlites				
			plagioclase	30	<2	subhedral - euhedral, Carlsbad twinning, albite twinning, periclase twinning oscillatory zoning
			orthopyroxene	20	<1	anhedral - subhedral, simple twinning
			clinopyroxene	10	<0.5	anhedral - subhedral, simple twinning
			hornblende	2	<1	subhedral
			biotite	3	<0.25	subhedral - euhedral
			opaque mineral(s)	10	<1	anhedral - subhedral
			groundmass	25		
biotite-rich group						
VCA-21-011	dacite					
		hypocrystalline, porphyritic, glomeroporphyritic, glassy groundmass				
			plagioclase	25	<2	anhedral - subhedral, oscillatory zoning, Carlsbad twinning, albite twinning
			biotite	10	<2	euhedral
			clinopyroxene	5	<2	anhedral - subhedral
			opaque mineral(s)	10	<0.5	anhedral
			groundmass	50		

sample	classification	texture(s)	minerals	modal abundance (%)	grain size (mm)	mineral description
VCA-21-028	andesite					
		hypocrystalline, porphyritic, glomeroporphyritic, glassy groundmass with microlites				
			plagioclase	15	<2	anhedral - subhedral, oscillatory zoning, Carlsbad twinning, albite twinning, periclase twinning
			orthopyroxene	10	<1	anhedral
			biotite	10	<2	subhedral - euhedral
			hornblende	5	<1	anhedral - subhedral
			opaque mineral(s)	5	<0.5	anhedral - subhedral
			groundmass	55		
VCA-21-029	andesite					
		hypocrystalline, porphyritic, glomeroporphyritic, glassy groundmass with microlites				
			plagioclase	25	<2	anhedral - subhedral, oscillatory zoning, Carlsbad twinning, albite twinning
			hornblende	20	<1	subhedral - euhedral
			orthopyroxene	5	<1	subhedral, simple twinning
			biotite	5	<2	subhedral
			opaque mineral(s)	4	<0.5	anhedral - subhedral
			clinopyroxene	1	<0.25	anhedral
			groundmass	40		

sample	classification	texture(s)	minerals	modal abundance (%)	grain size (mm)	mineral description
VCA-21-040	dacite					
		hypocrystalline, porphyritic, glomeroporphyritic, glassy groundmass with microlites				
			plagioclase	25	<2	subhedral, oscillatory zoning, Carlsbad twinning, albite twinning
			biotite	15	<1	euhedral
			clinopyroxene	15	<2	subhedral
			opaque mineral(s)	5	<1	anhedral
			groundmass	40		